

**İSTANBUL TECHNICAL UNIVERSITY ★ GRADUATE SCHOOL OF SCIENCE**  
**ENGINEERING AND TECHNOLOGY**

**ROCKMASS REACTION TO BLASTING IN MINES STUDIED BY LOCAL  
INDUCED SEISMICITY**

**M.Sc. THESIS**

**İrem ERGUNCU GÜÇLÜ**

**Department of Geophysical Engineering  
Geophysical Engineering Programme**

**Thesis Advisor: Prof. Dr. Abdullah KARAMAN**

**Thesis Co-Advisor: Prof. Dr. Savka DINEVA**

**JUNE 2016**



**İSTANBUL TECHNICAL UNIVERSITY ★ GRADUATE SCHOOL OF  
SCIENCE ENGINEERING AND TECHNOLOGY**

**ROCKMASS REACTION TO BLASTING IN MINES STUDIED BY LOCAL  
INDUCED SEISMICITY**

**M.Sc. THESIS**

**İrem ERGUNCU GÜÇLÜ**

**(505111404)**

**Department of Geophysical Engineering  
Geophysical Engineering Programme**

**Thesis Advisor: Prof. Dr. Abdullah KARAMAN**

**Thesis Co-Advisor: Prof. Dr. Savka DINEVA**

**JUNE 2016**



**İSTANBUL TEKNİK ÜNİVERSİTESİ ★ FEN BİLİMLERİ ENSTİTÜSÜ**

**PATLATMA SONUCUNDA OLUŞAN YEREL TETİKLENMİŞ SİSMİSİTENİN  
KAYA KÜTLESİ DAVRANIŞI ÜZERİNDEKİ ETKİSİNİN ARAŞTIRILMASI**

**YÜKSEK LİSANS TEZ,**

**İrem ERGUNCU GÜÇLÜ**

**(505111404)**

**Jeofizik Mühendisliği Anabilim Dalı**

**Jeofizik Mühendisliği Yüksek Lisans Programı**

**Tez Danışmanı: Prof. Dr. Abdullah KARAMAN**

**Eş Danışman: Prof. Dr. Savka DINEVA**

**JUNE 2016**



İrem ERGUNCU GÜÇLÜ, a M.Sc. student of İTÜ Graduate School of Science Engineering and Technology student ID 505111404 successfully defended the thesis/dissertation entitled “Rockmass Reaction to Blasting in Mines Studied by Local Induced Seismicity”, which she prepared after fulfilling the requirements specified in the associated legislations, before the jury whose signatures are below.

**Thesis Advisor :**      **Prof. Dr. Abdullah KARAMAN**      .....

İstanbul Technical University

**Co-advisor :**      **Prof.Dr. Savka DINEVA**      .....

Luleå University of Technology

**Jury Members :**      **Yrd. Doç. Dr. Tuna Eken**      .....

İstanbul Technical University

**Prof. Dr. Hanifi Çopur**      .....

                                 İstanbul Technical University

**Doç.Dr. Ekrem Zor**      .....

                                 TÜBİTAK

**Date of Submission : 02 May 2016**

**Date of Defense : 06 June 2016**





*To my spouse and family,*



## **FOREWORD**

I would like to thank my supervisors Prof. Dr. Abdullah Karaman at İstanbul Technical University and Prof. Dr. Savka Dinvevna at Luleå University of Technology (LTU) for their kindly help and wisdom. I thank to İstanbul Technical University for helping me improve my knowledge. I want also thank to LTU to for giving e me an opportunity for working on the thesis.

The study is supported financially by Vinnova (The Swedish Governmental Agency for Innovation Systems), Lundin Mining and Boliden AB. I am grateful for the technical help from Jouni Hansen-Haug from Lundin Mining, Andries van Zyl (IMS), Dimitar Mihaylov (LTU), and Anders Nystrom, Per-Ivar Marklund, Peter Fjellstroöm, and Shahram Mozaffari from Boliden AB Andries van Zyl (Institute of Mine Seismology, IMS), Dimitar Mihaylov (Lulea University of Technology), for the installation and maintenance of the local and the permanent seismic network, as well as providing of additional data related to mining operations and consultations. Ernest Lotter (IMS) was extremely helpful with his consultations regarding the IMS Trace software. Australian Centre of Geomechanics (ACG) provided the MxRap software for 3D visualization of the results.

June 2016

İrem ERGUNCU GÜÇLÜ  
(Geophysical Engineering)



# TABLE OF CONTENTS

	<u>Page</u>
<b>FOREWORD</b> .....	<b>ix</b>
<b>TABLE OF CONTENTS</b> .....	<b>xi</b>
<b>SYMBOLS</b> .....	<b>xiii</b>
<b>LIST OF TABLE</b> .....	<b>xv</b>
<b>LIST OF FIGURES</b> .....	<b>xvii</b>
<b>SUMMARY</b> .....	<b>xxiii</b>
<b>ÖZET</b> .....	<b>xxv</b>
<b>1. INTRODUCTION</b> .....	<b>1</b>
<b>2. INDUCED SEISMICITY</b> .....	<b>5</b>
2.1 Induced Seismicity .....	5
2.2 Induced Seismicity in Mines .....	5
<b>3. SEISMIC EVENT SOURCE PARAMETERS</b> .....	<b>9</b>
3.1 Seismic Waves .....	9
3.2 Kinematic Source Parameters .....	11
3.3 Dynamic Source Parameters .....	15
3.3.1 Magnitude .....	16
3.3.1.1 Local magnitude.....	16
3.3.1.2 Modified local magnitude .....	17
3.3.1.3 Moment magnitude .....	17
3.3.2 Seismic wave spectrum and corner frequency .....	18
3.3.3 Seismic moment and potency .....	19
3.3.4 Energy .....	20
3.3.5 Apparent stress .....	22
3.3.6 Stress drop.....	22
3.3.7 Source radius.....	23
<b>4. IMS TRACE SOFTWARE</b> .....	<b>25</b>
4.1 General Information .....	25
4.2 Data Processing .....	25
4.3 Perform Location .....	33
4.4 Perform Source.....	37
<b>5. ZINKGRUVAN MINE</b> .....	<b>41</b>
5.1 Geology .....	41
5.2 Mine Operation .....	43
5.3 Seismic Events Data Processing .....	45
5.3.1. Seismic systems and data .....	45
5.3.1 Number of seismic events with time.....	46
5.3.2 Data processing .....	49
5.3.3 Hypocenter locations.....	49
5.3.4 Magnitude, seismic moment, and energy distributions.....	52
5.3.5 Apparent stress and stress drop .....	59
5.3.6 Source radii .....	65
5.3.7 Summary and conclusions about the activity in Zinkgruvan .....	66
<b>6. GARPENBERG MINE</b> .....	<b>69</b>
6.1 Geology .....	69
6.2 Mine Operation .....	71

6.3 Seismic Events Data Processing .....	72
6.3.1 Seismic systems and data .....	72
6.3.1 Number of seismic events with time .....	74
6.3.2 Data processing .....	77
6.3.3 Hypocenter locations.....	78
6.3.3.1 Bad coverage .....	82
6.3.3.2 Good sensor coverage .....	88
6.3.4 Magnitude, seismic moment, and energy distributions.....	91
6.3.5 Apparent stress and stress drop .....	98
6.3.6 Source radii .....	105
6.3.7 Summary and conclusions about the activity in Garpenberg.....	105
<b>7. SEISMIC SOURCE PARAMETER AFTER BLASTING OF TWO MINES</b>	
<b>111</b>	
<b>8. CONCLUSIONS.....</b>	<b>115</b>
8.1 Zinkgruvan Mine.....	115
8.2 Garpenberg Mine.....	117
<b>REFERENCES .....</b>	<b>119</b>
<b>CURRICULUM VITAE .....</b>	<b>125</b>

## SYMBOLS

$\rho$	: Density
$\xi$	: Seismic efficiency
$r_0$	: Source Dimension
$\bar{\sigma}$	: Average Stress
$A_{P,S}$	: Average Radiation Pattern
$\mu$	: Rigidity
$A$	: Amplitude of Seismic Wave
$a$	: Area
$C$	: Regional Scale Factor
$D(f)$	: Displacement Spectrum
$E$	: Energy
$f$	: Frequency
$f_c$	: Corner Frequency
$Fi(m)$	: Earth Model
$f_0$	: Natural Frequency
$G$	: Geometric Spreading
$M_0$	: Seismic Moment
$M_L$	: Local Magnitude
$M_w$	: Moment Magnitude
$P$	: Potency
$Q$	: Correction of Ampitude
$r$	: Radius of Seismic Wave
$r_i$	: Residual Difference
$S(f)$	: Spectrum

<b>T</b>	: Dominant Period
<b>t</b>	: Origin Time
<b>t<sub>a</sub></b>	: Arrival Time
<b>t<sub>i</sub></b>	: Travel Time
<b>t<sub>p<sub>i</sub></sub></b>	: Predicted Travel Time
<b>v</b>	: Velocity
<b>α</b>	: P Wave Velocity
<b>β</b>	: S Wave Velocity
<b>λ</b>	: Lamé Constant
<b>σ<sub>a</sub></b>	: Apparent Stress
<b>Ω<sub>0</sub></b>	: Plateau



## LIST OF TABLE

	<u>Page</u>
<b>Table 4.1</b> : Explanation of abbreviations on the Seismogram screen. ....	29
<b>Table 5.1</b> : Percentage of types of recorded seismic events on July 1 and July 2, 2015.....	58
<b>Table 5.2</b> : The highest moment magnitude event information. ....	58
<b>Table 6.1</b> : Blasts near the local seismic system in Garpenberg Mine between October 8 and 13, 2015. ....	74
<b>Table 6.2</b> : October 10 production blast location calculations.....	78
<b>Table 6.3</b> : Seismic events locations differences.....	80
<b>Table 6.4</b> : Source parameters of October 8, 2015 at 04:42.....	85
<b>Table 6.5</b> : Source parameters of October 10, 2015 at 16:04.....	88
<b>Table 6.6</b> : Source parameters of October 10, 2015 at 16:10.....	90
<b>Table 6.7</b> : Processed seismic events moment magnitude with respect to seismic networks. ....	92
<b>Table 6.8</b> : The highest and the lowest values of some source parameters.....	95



## LIST OF FIGURES

	<u>Page</u>
<b>Figure 1.1</b> : Possible reasons of the rock mass damage (Raina et al, 2000). ....	2
<b>Figure 3.1</b> : Seismic wave's propagation (Kulhanek, 1997). ....	9
<b>Figure 3.2</b> : Seismogram of the earthquake in northern Greece on May 23, 1978, magnitude M=5.7, focal depth is 9 km (Kulhanek, 1997). ....	10
<b>Figure 3.3</b> : Epicenter and hypocenter location (Stein and Wysession, 2003). ....	11
<b>Figure 3.4</b> : Earthquake focus (hypocenter), epicenter and seismic station location and ray path between the focus and the station (Stein and Wysession, 2003). ....	12
<b>Figure 3.5</b> : (a) L2-norms contours from a grid search location of an earthquake off western Norway. The grid size is 2 km. The circle in the middle indicates the point with the lowest value (1.4 s). (b) The location of the earthquake and the stations used. (Havskov and Ottemöller, 2010). ....	14
<b>Figure 3.6</b> : Local magnitude estimation. ....	17
<b>Figure 3.7</b> : Theoretical displacement and acceleration spectrum by Brune Model (Haskov and Ottemöller, 2010). ....	18
<b>Figure 3.8</b> : Example of different type of displacement spectra, P- and S- waves and corresponding corner frequencies (Modified from Gibowicz and Kijko, 1994, modified). ....	19
<b>Figure 4.1</b> : IMS Trace windows with waveforms from six sensors. ....	26
<b>Figure 4.2</b> : Seismogram view. (a) Normal view and (b) Rotated view. ....	28
<b>Figure 4.3</b> : Example of noise data (all sensors). ....	30
<b>Figure 4.4</b> : Example of view with unseparated seismogram. ....	31
<b>Figure 4.5</b> : Example of view with separated seismogram. ....	31
<b>Figure 4.6</b> : Example of enlarge a seismogram (zoom in). ....	32
<b>Figure 4.7</b> : The hypocenter location after the first phase picking. ....	34
<b>Figure 4.8</b> : The result after second location performed before S-wave arrival correction on sensor 508. ....	34
<b>Figure 4.9</b> : The result after third location performed after S-wave arrival correction on sensor 508. ....	35

<b>Figure 4.10</b> : The result after fourth performed location after correction of P (or S) arrival on sensor 506 was eliminated (disabled).....	36
<b>Figure 4.11</b> : The result after fifth performed location after correction of P (or S) arrival on sensor 510 correction.....	36
<b>Figure 4.12</b> : Brune model spectrum (a) displacement (b) acceleration spectrums (Young et al, 1989). .....	38
<b>Figure 4.13</b> : The source parameters of the event (on October 10 at 16:04) source parameter solution with slope $\omega - 2$ . .....	38
<b>Figure 4.14</b> : The source parameters of the event (on October 10 at 16:04) source parameter solution with slope $\omega - 3$ . .....	39
<b>Figure 5.1</b> : Geology of southern Sweden (Bengtsson, 2000). .....	42
<b>Figure 5.2</b> : Generalized geology map of Zinkgruvan mine site (Owen and Meyer, 2013). .....	43
<b>Figure 5.3</b> : Mine operation sites (Owen and Meyer, 2013). .....	44
<b>Figure 5.4</b> : Mining methods at Zinkgruvan mine (Pakalnis and Hughes, 2011). ....	45
<b>Figure 5.5</b> : Local network installation at site 871 and 874. The black circles show the sensor, the red dots are observation wells and the yellow dots are extensometer. ....	46
<b>Figure 5.6</b> : Number of recorded seismic events. Blasts are marked as red circles. Red crosses show the highest moment magnitude events (the magnitude scale is shown on the right side of the graph). .....	48
<b>Figure 5.7</b> : All manually obtained events locations (vertical plane). Size of the circle and the color correspond to the magnitude. The sensor locations are shown as blue cylinders (uniaxial sensors) or red triangles (triaxial sensors). .....	50
<b>Figure 5.8</b> : Seismic event locations on July 1, 2015.....	51
<b>Figure 5.9</b> : Seismic event locations on July 2, 2015.....	51
<b>Figure 5.10</b> : Moment Magnitude distribution on July 1, 2015. ....	52
<b>Figure 5.11</b> : Moment Magnitude distribution on July 2, 2015. ....	53
<b>Figure 5.12</b> : Logarithm of energy versus moment magnitude for both days – July 1 (blue) and July 2 (red), 2015.....	54

<b>Figure 5.13</b> : Seismic energy of seismic events on (a) July 1 and (b) July 2. The color and the size of the circles show the energy and local magnitude, respectively. ....	55
<b>Figure 5.14</b> : Cumulative energy radiation for P and S wave on July 1 and July 2, 2015 (Blue dots are for the events before the blast and orange dots are for the events after the blast).....	57
<b>Figure 5.15</b> : $E_s/E_p$ of seismic events on (a) July 1 and (b) July 2. The color and the size of the circles show the $E_s/E_p$ ratio and local magnitude, respectively. ....	59
<b>Figure 5.16</b> : Logarithm of apparent stress versus logarithm of seismic moment on July 1 (blue dots) and July 2 (red dots).....	60
<b>Figure 5.17</b> : Logarithm of apparent stress and logarithm of seismic energy on July 1 (blue dots) and July 2 (red dots). ....	61
<b>Figure 5.18</b> : Apparent stress of seismic events on (a) July 1 and (b) July 2. The color and the size of the circles show apparent stress and local magnitude, respectively. ....	62
<b>Figure 5.19</b> : Stress drop versus logarithm of seismic moment on July 1 (blue dots) and July 2 (red dots).....	63
<b>Figure 5.20</b> : Logarithm of stress drop versus logarithm of seismic energy on July 1 (blue dots) and July 2 (red dots). ....	64
<b>Figure 5.21</b> : Logarithm of apparent stress versus stress drop on July 1 (blue dots) and July 2 (red dots).....	64
<b>Figure 5.22</b> : Stress drop of seismic events for (a) July 1 and (b) July 2. The color and the size of the circles show the stress drop and local magnitude, respectively. ....	65
<b>Figure 5.23</b> : Source radius versus moment magnitude on July 1 (blue dots) and July 2 (red dots). ....	66
<b>Figure 6.1</b> : Geology map of Garpenberg (Allen et al, 2008).....	71
<b>Figure 6.2</b> : Garpenberg mine ore bodies distribution (Allen et al, 2008).....	72
<b>Figure 6.3</b> : Location of the geophones in the local seismic system in Garpenberg mine with the number of the sensor sites. Blue circles are uniaxial (surface) geophones and red circles are three-axial (surface or borehole)	

geophones. The vertical profiles with the sensor positions are shown too. ....	73
<b>Figure 6.4 :</b> Number of seismic events recorded by the local seismic system between October 8 and 13, 2015 (per half an hour). Blasts are marked as red circles. Red crosses show the highest moment magnitude events (the magnitude scale is shown on the right side of the graph). ....	76
<b>Figure 6.5 :</b> Seismic event locations in the (a) Merge Database, (b) Permanent Network and (c) Local Network with event time as color and the circle size representing the seismic event moment magnitude. ....	79
<b>Figure 6.6 :</b> The ray path fort the seismic event at 04:42 on October 8, 2015 and the theoretical ray paths from the sensors (red lines) (case of bad sensors coverage). ....	83
<b>Figure 6.7 :</b> Travel times for the event at 04:42 on October 10, 2015. ....	84
<b>Figure 6.8 :</b> Seismic event locations calculated with data from (a) Merged Dataset, (b) Local Network and (c) Permanent Network. The red lines are the theoretical ray paths from the sensors (case of bad sensor coverage). .	87
<b>Figure 6.9 :</b> Ray path of the seismic event at 16:10 on 10-October 2015 (red lines represent the theoretical ray paths to the sensors (example of good sensors coverage). ....	89
<b>Figure 6.10 :</b> Travel times for the event at 16:10 on 10-October 2015. ....	89
<b>Figure 6.11 :</b> Logarithm of energy versus seismic moment. The green, red and blue dots represent the local network, the permanent network and merged dataset, respectively. ....	91
<b>Figure 6.12 :</b> Seismic moment changing with respect to the events code (number). The green, red and blue dots represent the local network, the permanent network and merged dataset, respectively. ....	94
<b>Figure 6.13 :</b> Seismic energy of seismic events of (a) merged database, (b) permanent network and (c) local network. The green triangles show the local network sensors and the size of the circles represent the moment magnitude. ....	96
<b>Figure 6.14 :</b> Seismic energy of seismic events of (a) merged database, (b) permanent network and (c) local network. The green triangle shows the	

local network sensors and the size of the circles represent moment magnitude.....	97
<b>Figure 6.15</b> : The logarithm of apparent stress versus logarithm of seismic moment. The green, red and blue dots represent the local network, the permanent network and merged dataset, respectively. ....	98
<b>Figure 6.16</b> : The logarithm of apparent stress and energy. The green, red and blue dots represent the local network, the permanent network and merged dataset, respectively. ....	99
<b>Figure 6.17</b> : Apparent stress of seismic events of (a) merged database, (b) permanent network and (c) local network. The green triangles show the local network sensors and the size of the circles represent moment magnitude.....	100
<b>Figure 6.18</b> : Stress drop versus logarithm of seismic moment. The green, red and blue dots represent the local network, the permanent network and merged dataset, respectively. ....	101
<b>Figure 6.19</b> : Stress drop and logarithm of the seismic energy. The orange, blue and purple dots represent the local network, the permanent network and merged dataset, respectively. ....	102
<b>Figure 6.20</b> : The logarithm of stress drop and the logarithm of apparent stress. The green, red and blue dots represent the local network, the permanent network and merged dataset, respectively. ....	102
<b>Figure 6.21</b> : Stress drop of seismic events of (a) merged database, (b) permanent network and (c) local network. The green triangle shows the local network sensors and the size of the circle represents moment magnitude.....	104
<b>Figure 6.22</b> : Source radius versus moment magnitude. The green, red and blue dots represent the local network, the permanent network and merged dataset, respectively. ....	105
<b>Figure 6.23</b> : Dynamic seismic parameters change due to the coverage. ....	106
<b>Figure 6.24</b> : Corner frequency of P wave. ....	107
<b>Figure 6.25</b> : Corner frequency of S wave. ....	107
<b>Figure 6.26</b> : Fault plane and body waves radiation patterns. ....	108
<b>Figure 6.27</b> : Good coverage seismic events body waves energy.....	109

**Figure 6.28** : Bad coverage seismic events body waves energy. .... 109

**Figure 7.1** : Logarithm of the energy versus moment magnitude of July 1 (blue),  
July 2 (red) and October 10 (green) seismic events..... 112

**Figure 7.2** : Logarithm of the apparent stress versus logarithm of the moment on  
July 1, July 2 and October 10 seismic events. .... 113

**Figure 7.3** : Logarithm of the stress drop versus logarithm of the radiated energy on  
July 1, July 2 and October of 10 seismic events. .... 113



# **ROCKMASS REACTION TO BLASTING IN MINES STUDIED BY LOCAL INDUCED SEISMICITY**

## **SUMMARY**

Elaborate manual processing of mining-induced seismic events following production blasting in two of the oldest underground Swedish mines (Zinkgruvan and Garpenberg) was carried out in order to obtain the most accurate possible solutions for kinematic and dynamic parameters and to obtain information about the reaction of the rock mass to blasting. The main problems for each mine were not the same so slightly different procedures were followed. Data used in the thesis was recorded by small scale temporary local seismic systems, consisting of 16 to 18 sensors, installed in both mines in 2015 to study the local site effects and ground motion from possible damaging seismic events. Additional data from the permanent mine-wide seismic system in Garpenberg was also used.

A rockburst event occurred on July 2, 2015 (Mw 1.2) at 15:01 during a blast at Zinkgruvan Mine that caused damage. The source parameters of the seismic events following the blast on July 2 were studied and compared with the parameters of the events following another blast on July 1 (in total 4517 waveforms from 271 events were analyzed).

The moment magnitude of all events ranged between -3.3 and 1.2. The events on July 1 and July 2 formed two separate large clusters (with length up to 60 to 80 m) with orientations of long axes perpendicular to each other. The largest moment magnitude events in each cluster were located at the edges of the corresponding clusters: Mw 0.6 event on July 1 was on the top of the first cluster, however, the Mw 1.2 event on July 2 was on the bottom of the other cluster.

Dynamic source parameters of seismic events on July 1 and 2 showed consistently different values and relationships. In general the events on July 1 had smaller magnitudes, seismic moment, seismic energy, apparent stress and stress drop compared with the events on July 2. The source parameters relationships with each other were also examined and found different.

The second case study was related to seismicity caused by production blasting in Garpenberg Mine. The parameters of the events within the period October 8 to 13, 2015 were studied. Three different datasets, for the same 30 events recorded by the permanent seismic system, temporary local seismic system, and merged data from both systems, were used to test the sensitivity of the parameters to the number of sensors and their geometry, and to test if merging of the data could be of practical interest for the routine seismicity studies. The moment magnitude of the events varied between -1.4 and 0.9. In total 962 waveforms were analyzed.

The results of the tests for the 30 studied events showed that the source locations of seismic event in the individual datasets (local and permanent) were not exactly the same and the differences between the locations could be up to 300 m depending on the azimuthal sensor coverage. In case of good sensor coverage, the hypocentral locations were more accurate and the difference between the locations obtained by each seismic system dataset was smaller than in case of bad sensor coverage. Some dynamic source parameters, on the other hand, were less affected by sensor coverage. However, it was

found that a few dynamic parameters as energy, energy ratio ( $E_s/E_p$ ), apparent stress and stress drop were very sensitive to the geometry of the seismic system and change of up to 300% were observed in case of using different sensors datasets from sensors with bad coverage. The local network seismic energy was found to be always higher than the seismic energy obtained by the data from the permanent system independently on the sensor coverage. The consistent difference was attributed to underestimated correction for the attenuation, which affects more the results obtained from the permanent system with sensors generally at larger distances. A recommendation was made that the merged database should be used to obtain more accurate results, especially for hypocenter location, as the sensors of both systems together provide the best possible coverage but merging the data for calculation of dynamic parameters should be used with caution.

In conclusion, the results in this thesis can be divided into two parts: first, results related to the reaction of the rock mass to blasting for Zinkgruvan and Garpenberg Mine, and second, methodological results related to the sensitivity of the kinematic and dynamic parameters to the number and geometry of the sensor locations, and practical application for Garpenberg Mine. Valuable information was obtained also about the orientation of the cluster of seismicity after the damaging event on July 2, 2015 at Zinkgruvan mine.

This information can be useful to study the relationship between the damage and the source parameters and ultimately to improve the understanding the damage potential from seismic events in this the mines. All results could be used for further investigation on re-entry protocols for these two mines and seismic hazard assessment.

# PATLATMA SONUCUNDA OLUŞAN YEREL TETİKLENMİŞ SİSMİSİTENİN KAYA KÜTLESİ DAVRANIŞI ÜZERİNDEKİ ETKİSİNİN ARAŞTIRILMASI

## ÖZET

Çok küçük manyetütlü depremlerin incelenmesini konu alan tetiklenmiş sismisite, yer bilimleri açısından oldukça önemlidir. Tetiklenmiş sismisite sismoloji araştırmalarının bir alt kolu olup, akustik emisyon ve doğal kaynaklı depremlerin arasında yer almaktadır. İndüklenmiş sismisite çalışmaları; doğal gaz ve petrol üretim kuyularında, jeotermal kaynaklarının üretim ve geri besleme kuyularında, baraj ve göl çevrelerinde, atık su depolarının çevresinde ve yer altı işletmelerinde etkin olarak kullanılmaktadır. Tetiklenmiş sismisite çalışmaları ile sismik aktivitelerin lokasyonlarının belirlenmesi, sismik aktivitelerinin oluşum mekanizmalarının anlaşılması ve kaya patlamalarının veya çökmelerinin sebepleri araştırılmaktadır.

Bu tez çalışmasında, yer altı maden işletmelerinde meydana gelen küçük manyetütlü tetiklenmiş depremler incelenmiş ve çevre kayacın bu sismik aktivitelere verdiği tepkiler değerlendirilmiştir. Birçok maden sahası kendine özgü, karakteristik olarak nitelenebilecek şekilde sismik yönden aktiftir. Yapılan çalışmalar, maden sahalarının jeolojik özellikleri ve maden üretim yöntemi aynı olsa bile sismik aktivite seviyelerinin birbirlerinden çok farklı olabileceğini göstermektedir. Ancak bu farklı sismik aktivite seviyelerinin nedenleri henüz açıklanamamış değildir.

Tetiklenmiş sismik aktiviteler genel olarak çok düşük manyetütlü yapay depremler olarak tanımlanmaktadır ve yer içinde meydana gelen dış etkiler sonucunda (madenler için üretim patlatmaları veya üretim yönteminin doğasından kaynaklanan) bölgedeki stress dağılımı değişmektedir. Ancak tetiklenmiş sismik aktivitenin meydana gelmesindeki önemli etkenlerden biri de kayaç içindeki stress dağılımı olmakla birlikte, yapılan çalışmalar kayaçtaki porozite değişimi ve ani enerji yayılımlarının da bölgede tetiklenmiş sismik aktivitelere neden olduğunu göstermektedir.

Yer altı maden işletmeleri tetiklenmiş sismik aktivitenin oluşmasında önemli rol oynamaktadır. Cevher ve çevre kayacın yapısı, maden üretim yöntemi, maden dizyanı ve derinlik tetiklenmiş sismik aktivite seviyesini etkileyen parametreler olarak sayılmaktadır. Günümüze kadar yapılan çalışmalar, tetiklenmiş sismitenin derinlikle birlikte arttığını ancak yüzeye yakın yer altı işletmelerinde de göreceli olarak yüksek manyetütlü aktiviteler olabildiğini göstermiştir (kaya patlamaları ya da taban çökmesi). Bu nedenle üretim seviyesi derinleştikçe, kaya patlamaları gibi ölümcül ve hasarlı kazaların görülmesi sıklaşmaktadır. Sismik aktivitelerin lokasyonları ve ativitelerin göreceli olarak artış gösterdiği zamanların doğru olarak belirlenmesi önemlidir. Özellikle üretim patlatmalarının hemen sonrasında tetiklenmiş sismisitede normalin çok üstünde artışlar gözlemlenmektedir. Unutulmaması gereken diğer önemli bir konu ise sismik aktivitedeki benzer artışlar kaya patlamaları gibi kazaların sonucunda da görülebilmektedir. Öte yandan tetiklenmiş sismisitenin sonuçları göz önünde bulundurularak madene yeniden giriş kuralları düzenlemekte, üretim yöntemleri güncellenebilmekte ve maden tahkimat yöntemi değiştirilebilmektedir.

Tez çalışması kapsamında İsveç'in güneyinde yer alan Zinkgruvan ve Garpenberg metal madenlerinden elde edilen veriler değerlendirilmiştir. Zinkgruvan ve

Garpenberg yeraltı işletmeleri, İsveç'te günümüzde halen işletilmeye devam eden en eski madenlerdendir ve birbirlerine olan uzaklıkları yaklaşık olarak 200 km'dir. Her iki işletmede de çinko, gümüş ve kurşun cevherleri bulunmakta, yüzeyden ortalama 1000 m derinde üretim devam etmektedir. Zinkgruvan maden sahası metasediman ve metavolkanik kayalarla karakterize edilmektedir. Günümüzde aktifliği tartışmalı olan iki fay yapısı ortaya konmuştur ve bu fay sistemlerinin hareketleri sonucunda metal cevheri günümüzdeki halini almıştır. Maden sahasındaki üretimler bütün cevher parçalarında devam etmektedir. Garpenberg maden sahası ise daha karmaşık bir jeolojik yapının üstüne kurulmuştur. Maden sahasında içinde bulunduğu kıvrım yapısı ve farklı metamorfizma olaylarının sonucunda cevher bölünmüş ya da yakın ancak farklı lokasyonlarda yeniden oluşmuştur. Ancak, Garpenberg'deki cevher Zinkgruvan cevherine kıyasla daha az zarar görmüştür.

Zinkgruvan Madeninde 2 Temmuz 2015 günü, yerel saat ile 15:00 sularında, 1100 metre derinde kaya patlaması gerçekleşmiştir. Meydana gelen bu kazada tünel kapanmış ve üretime bir süre ara verilmiştir, çalışmada bu olayın sebepleri ve civar kayaların tepkisi araştırılmıştır. Ayrıca Garpenberg Madeni'nde 8-13 Ekim 2015 tarihleri arasında kaydedilen tetiklenmiş sismik aktiviteler incelenmiş, ancak madende bu süre zarfında herhangi bir kritik kaza olmamıştır. Garpenberg Maden'inde iki farklı sismik ağ bulunmaktadır. Bölgesel ağ yüzeyden 720 metre derinde ve toplamda 16 kayıtçıdan oluşmaktadır. Bu kayıtçılar aynı yatay düzlemde konumlandırılmıştır. Diğer yandan Kalıcı ağ maden içinde farklı seviyelerde konumlandırılmış, toplam 19 kayıtçıdan bulunmakta ve bu kayıtçılar genel olarak Yerel ağın daha altında bulunmaktadır.

Zinkgruvan madeninde 1-2 Temmuz 2015 tarihleri arasında 3000 den fazla sismik aktivite kaydedilmiştir. Ancak veri işlem aşamasında 271 veri incelenmiştir. Veri işlemi yapılacak olan sismik aktivite belirlenmesinde iki farklı kriter göz önünde bulundurulmuştur. Bunlardan ilki, sismik aktivitenin manyetütü küçüldükçe daha az kayıtçı tarafından kaydedileceği için, 15 veya daha fazla kayıtçı tarafından kaydedilmiş olan sismik aktiviteler değerlendirmeye alınmıştır. İkinci kriter ise üretim patlatmasından (12:00) 3 saat öncesinden gün sonuna kadar olan kayıtlar dikkate alınmıştır. Madenin genel sismik aktivite karakteristiğine bakıldığında, patlatma sonrası kaydedilen sismik aktivite oldukça fazla olmaktadır.

1-2 Temmuz 2015 tarihlerinde kaydedilen ve veri işlemleri gerçekleştirilen tetiklenmiş sismik aktivitelerin yaklaşık %63'ü shear kaynaklıdır. Toplamda 4 büyük ( $M_w > 0$ ) tetiklenmiş sismik olay kaydedilmiştir. Bunlardan sadece bir tanesi 1 Temmuz 2015'de kaydedilmiştir. İki günlük kayıtların içerisindeki en büyük moment magnitudü sismik aktivite ise 2 Temmuz 2015 gününde yapılan patlatma kaydı içinde görülmüş ve moment manyetütü 1.2 olarak bulunmuştur. Aynı gün kaydedilen diğer iki tetiklenmiş sismik olayların moment manyetütleri ise 0.4 ve 0.2 olarak hesaplanmıştır.

1 Temmuz 2015 tarihinde kaydedilen tetiklenmiş depremlerin yaklaşık olarak 135 tanesi veri işlem aşamasından geçmiştir ve odak noktalarının genel olarak bir hat üzerinde toplandığı gözlemlenmiştir. 1 Temmuz 2015 tarihinde, üretim patlatmasından yaklaşık 15 dakika sonra, moment manyetütü 0.6 olan tetiklenmiş sismik aktive kaydedilmiştir ve bu tetiklenmiş aktivitenin dinamik parametreleri, gün içinde kaydedilen diğer tetiklenmiş depremlerden daha yüksektir. Bu sismik olayın sonucunda açığa çıkan toplam enerji neredeyse günün geri kalanında kaydedilen sismik olaylarda elde edilen toplam enerji yayılımından fazladır. Dinamik kaynak

parametreleri genel anlamda göreceli olarak düşük seviyede kalmıştır. Üretim patlatmasından sonraki ilk yarım saatte toplamda 200'den fazla kayıt alınmış olmakla birlikte, patlatmadan yaklaşık 1.5-2 saat sonrasında, sismik aktivite seviyesi patlatma öncesine geri dönmüştür.

2 Temmuz 2015 tarihindeki kayıtlar, kaya patlaması sebebi ile ancak saat 17:00 sularına kadar alınabilmiş ve yaklaşık olarak 131 tetiklenmiş depremin veri işlemi yapılmıştır. Tetiklenmiş sismik aktivitelerin odak noktalarına bakıldığında genel eğilimin, 1 Temmuz 2015 tarihinde oluşan sismik olaylara dik olacak şekilde ters doğrultuda yoğunlaştığı görülmektedir. Ancak 2 Temmuz 2015 günü kaydedilen en büyük moment magnitudü depremlerin ise mevcut yönelimin sol-altında olduğu görülmüştür. Dinamik kaynak parametrelerinin kesinlikle 1 Temmuz 2015'de kaydedilen sismik aktivitelerin parametreleri ile uyumlu olmadığı gözlemlenmiştir. Ancak 2 Temmuz günü kaydedilen sismik olayların dinamik kaynak parametreleri neredeyse her zaman 1 Temmuz sismik aktivilerinin sonuçlarından daha büyük çıkmaktadır. En ilgi çekici kısım ise, sismik aktivitelerin sonucunda ortama yayılan enerjilerin kümülatif değerlerine bakıldığında, dört farklı zamanda enerji sıçramaları görülmüştür. Her ne kadar dinamik kaynak parametreleri daha yüksek olsa da, kaydedilen bütün bu sismik aktivitelerin kaya patlamasına neden olup olmadığı açıklanamamaktadır. Çünkü kaya patlamasına neden olan kırık yapılarının ortamda zaten oluşmuş olma olasılığı mevcuttur. Patlatmalar sonucunda kırık yapıları derinleşmiş ve sismik olaylar bu kırık zonları üzerinde gerçekleşmiş olabilir. Ya da sismik aktivitelerin etkisi ile kırık yapıları oluşmuş ve bu yapıların giderek zayıflaması sonucunda mevcut hasar oluşmuş olabilir.

Garbenberg Maden sahasında 2012 yılından beri tetiklenmiş sismik aktiviteler gözlenmektedir. Üretim sahası içinde iki farklı sismik şebeke kurulmuştur. Yerel sistem 50×40 metre karelik bir alana yerleştirildiğinden, göreceli olarak daha küçük manyetütü sismik aktivitelere daha duyarlıdır. 10 Ekim 2015 tarihinde yapılan üretim patlatmasının Yerel sisteme yakın olmasından dolayı, Yerel sistemin kaydettiği sismik aktivite sayısında kayda değer bir artış görülmüştür. Diğer yandan Kalıcı sistem bütün maden içine dağıldığından, bölgesel patlamaların sonucunda ortaya çıkan tetiklenmiş sismik aktivite sayısındaki artıştan etkilenmemektedir. 10 Ekim 2015 günü yapılan patlatma kayıtları her iki sismik şebeke tarafından da kaydedilmiş ancak Kalıcı ağın kayıtlarından hesaplanan lokasyon tayini gerçek patlatma lokasyonuna daha yakın bulunmuştur. İki farklı ağın sonuçlarının farklı olmasından dolayı, çalışma iki sismik ağın kayıtlarının kinematik sonuçlarının karşılaştırmasına dayanmaktadır.

Şebekelerin karşılaştırılabilmesi için her iki sistem tarafından kaydedebilecek kadar büyük manyetütü sismik aktivite olması gerekmektedir. Bu nedenle iki sistem de kontrol edilmiş ve gürültülü kayıtlar tamamen göz ardı edilmiştir. Karşılaştırma sonucunda moment manyetütü 0'dan büyük 30 kayıt tespit edilmiştir. Bunlardan bir tanesi 10 Ekim 2015 patlatma kaydı olmasından ve 3 tane kayıt odak noktasının kalan tetiklenmiş depremlerin odağından çok farklı olmasından dolayı sonraki karşılaştırmalara eklenmemiştir. Yerel ve kalıcı ağ haricinde, aynı sismik aktiviteden elde edilen kayıtların birleştirilmesi sonucunda Birleştirilmiş Veriseti oluşturulmuş ve karşılaştırmaya dahil edilmiştir.

Karşılaştırmanın daha anlamlı olabilmesi için sismik aktiviteleri sensor kapsamına göre ikinci bir sınıflamaya tabi tutulmuştur. Buna göre, sismik aktiviteler kayıtlarının ortasında kaldığında her üç verisetinin kinematik sonuçları benzer

çıkılmaktadır. Aksi durumda ise Kalıcı Şebeke ile Birleştirilmiş Veri seti odak sonuçları birbirine daha yakındır.

Dinamik kaynak parametrelerinde ise yukarıda bahsedilen sınıflama sonuçları arasında benzerlik bulunamamıştır. Yerel Şebeke sonuçları, sismik aktivite kaynağını shear olarak vermekte ve kalıcı ağdan ve Birleştirilmiş Veriseti'nden alınan sonuçların ancak düşük bir kısmı shear olay olarak çözümlenmiştir.

Yapılan çalışmaların sonucunda yeraltı işletmelerinde, sismik aktivite ile patlatma arasında güçlü bir ilişki vardır. Patlatmalar eğer kayıtçılara yakın ise sismisitedeki artış daha belirgin olmaktadır. Dinamik kaynak parametleri ise yapılan veri işlem aşamaları ile ilişkili olmakla birlikte parametrelerin sismik dalganın ilerlediği yoldan da etkilendiği düşünülmektedir.

## **1. INTRODUCTION**

Induced seismicity is a branch of seismology and the size and the frequency of the induced seismic event is between acoustic emission and natural earthquakes and commonly are related to artificial water reservoirs (dams and lakes), water waste disposals, oil and gas reservoir extraction and hydraulic fracturing, geothermal energy production and underground mining. This study focuses on induced seismic activity due to underground mining in two mines – Zinkgruvan and Garpenberg (Sweden) after blasting in order to obtain a new empirical information about rock mass response.

Zinkgruvan and Garpenberg mines are located in the southern part of Sweden. Each mine has different geological conditions and mining methods which affect the seismic activity. Moreover, the ore body is extracted after production blast. The main aim of this study is to clarify the relation between production blast and seismic activity. It is already known that after the production blast, number of seismic activity increases because the stress of rock mass re-distributed. The seismic activity is also affected by other reasons, such as local geology, mining method, and pre-existing cracks. However, the local geology and pre-existing cracks are not easy to solve. There is not enough time to collect especially the local geology data, because the tunnels must be supported as soon as possible. Pre-existing cracks in the mine site cannot be observed easily. Induced seismic events is monitored to reveal the fracture/failure processes. The result of the induced seismic events, especially underground mine, can be used in order to avoid deadly or violent accidents into the tunnels. Figure 1.1 explains possible reasons of the rock mass damage in the mine site.

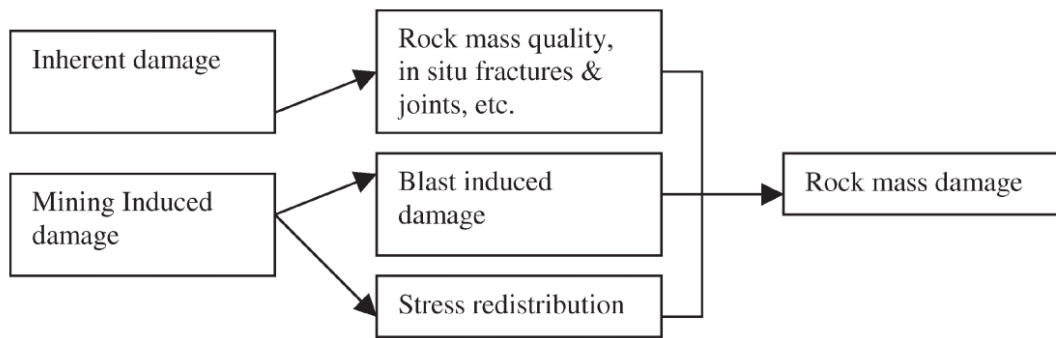


**Figure 1.1 :** Possible reasons of the rock mass damage (Raina et al, 2000).

Not only kinematic but also dynamic parameters of the induced seismic events were calculated. The kinematic parameter includes the location determination of the seismic event. The dynamic source parameters are magnitude, seismic energy, seismic moment, apparent stress, stress drop and source radius. These parameters help to understand rock mass response. The pre-blast conditions must be defined to understand the effect of the production blast.

Zinkgruvan mine is one of the oldest mines in Sweden. It is owned by Lundin Mining, and is located about 240 km south-west of Stockholm. Current mining activity take place in three ore bodies. They are Nygruvan, Burkland and Cecilia. The current mining method is underhand and overhand mining sublevel stopping. Mining operations at present are ongoing down to 1200 meters from the ground surface. Zinkgruvan mine is seismically active, and it has been monitored since November 1996.

Additionally to the permanent seismic monitoring system, a local network consisting of 18 sensors was installed in May-August 2015 at ~1100 m depth, in area around 40×50m<sup>2</sup>. They were installed not only to the surface of gallery but also special boreholes (9 meter inside to the gallery wall). A rockburst occurred at Zinkgruvan mine on July 2, 2015, caused by a production blast. Large number of seismic events were recorded by the local system after the rockburst but, the local system was disconnected during this violent event, and the spare recording kept data only for three hours after the blast. This study focuses on the understanding of the dynamic rock response after the blast on July 2, and compares with the nearby blast on July 1.

More than 3000 seismic events were recorded between July 1 and July 2, 2015 by the local seismic network. Data processing was done manually via IMS Trace software. It



is not possible to process all data because of several reasons, such as lower amplitude, less accuracy of the result due to less sensor number, and noise data etc. In order to avoid these problems, the data which would be processed, had to be specified before data processing stage. First filter was designed to optimize the sensor number. If seismic event recorded by more than 15 sensors, it was marked as to be processed events because sensor numbers link with accuracy of result and magnitude of the events. Second filter was set up to understand the rock mass response before and after the production blast. This filter was applied to the data after the first filter. The processed seismic event were recorded between three hours before the production blast and after the production blast until last record of the day. After these filters, 271 seismic events remained and these events were processed to obtain all kinematic and dynamic parameters of the seismic sources. Data from the permanent seismic system was installed as the sensors are sparse and far away the study area.

Garpenberg mine is the oldest mining site at Central Sweden where locates 200 km north-west of Stockholm. It is owned and operated by Boliden Mineral AB. The geology of Garpenberg area is more complicated, the ore body is generated in the fold and two metamorphism episodes were documented around Garpenberg Mine site. Mining operations are ongoing in a few ore bodies at the same time. The complex ore contains zinc, silver, lead, gold and copper. The mining method is overhand cut-and-fill. The production levels are between ~500 and ~1250 m depth.

The mine seismicity has been monitored by a permanent system since 2012, consisting of 27 sensors by 2015 but 2 of the sensors disconnected. A local seismic system, consisting of 16 sensors was installed in August 2015 at depth of ~720 m in a small area of  $50 \times 104 \text{ m}^2$ . The design of the local network is almost same with Zinkgruvan Mine. Some sensors are at the surface of gallery, rest of them inside the rock mass. Two large production blasts in proximity to the local system were made on October 8 and 10, 2015. Large number of seismic events following these blasts (especially after October 10, 2015) were recorded by both, the permanent and local seismic systems. In this study data from both systems were merged to improve uniqueness of the kinematic and dynamic parameters of the source of the seismic events in order to obtain information about the rock mass response to blasting. The results for the merged data were compared with the individual results from the dataset of each network.

The comparison of the results for both case studies shows some similarities and differences in the rock mass response to blasting. The number of the seismic events dramatically increases, especially first half an hour. However, returning the pre-blast level depends on the mine characteristic. The level of dynamic source parameters were also different for each mine. Although, several higher moment magnitude seismic events were recorded after the production blast at Garpenberg Mine, a curial damage was not reported and very few seismic events were recorded each day by the local network. According to this result, Zinkgruvan mine may be more sensitive to stress distribution. The results could be used for further investigation on re-entry protocols for these mines and seismic hazard assessment. However, further detailed studies are still necessary to explain rockmass responses.

## **2. INDUCED SEISMICITY**

### **2.1 Induced Seismicity**

Induced seismicity occurs as a result of stress redistribution, pore pressure change, volume change and applied forces or load due to human activity. Induced seismicity has become a very important subject in relation to hydrocarbon extraction, hydraulic fracturing, carbon dioxide injection, waste water management, reservoir impoundment, tunnel projects, nuclear underground waste disposal, and not the last underground mining (Talebi, 1998; Gurha, 2000; McGarr et al, 2002; Occhiena et al 2014; Nicholson and Wesson, 1992). To be able to make more sophisticated studies first the following three tasks have to be clarified by induced seismicity monitoring (Chorney et al, 2012). They are calculating the seismic event location, determining the failure mechanism and finding possible reason(s) of the failure.

### **2.2 Induced Seismicity in Mines**

According to Gibowicz (1990), Cook (1976) defined the induced seismicity as ‘Seismicity induced by mining is usually defined as the appearance of seismic events causes by rock failures as a result of changes in the stress field in the rockmass near mining excavations’. Cao et al (2009) definition was ‘Mining-induced seismic events, which are induced by the sudden release of elastic strain energy in rock mass, are associated not only with superficial structure movement triggered by new stress concentration with mining operations, but also large geological discontinuity, affected by the extent and means of mining’. It is obvious that mining induced seismicity is both related to increase in the shear stresses or decrease in the normal stresses on the fault plane (Gibowicz and Lasocki, 2001).

Induced seismicity is quite new branch of seismology. The first study about induced seismicity was done at Ruhr coal basin (Germany) at 1908 (McGarr et al, 2002). The Upper Silesia coal mine was the first one monitored from induced seismicity

perspective starting at 1920 (McGarr et al, 2002). In 1933, China mining industry was faced with the first rockburst activity at 200 meter depth (Gibowicz and Lasocki, 2001). The first rockburst at Ural bauxite mines (Russia) was announced at the beginning of 1970s. The event was at 350 meters depth and estimated magnitude was between 3.0 and 3.5 (Gibowicz and Lasocki, 2001). Several rockburst series were reported at Grängesberg's iron ore bodies (Central Sweden) between August 1974 and July 1976 (Båth, 1979). Local magnitude 5.2 event occurred at Klerksdrop Gold Mine (South Africa) on April 7, 1997 which was one of the largest seismic events induced by mining (McGarr et al, 2002). Tragic rockburst, local magnitude 3.5, occurred in Sudbury hard rock mine (Canada) in 1984 (Young et al, 1989). Rockburst activity recorded at Solvay trona mine Wyoming (USA) in 1995. The local magnitude was 5.2 (Ge, 2005).

Seismic monitoring helps to understand the dynamics of seismic activities in mines. Seismic monitoring networks are installed in mines not only for study of rockburst hazard but also for detection of methane signature (Murphy et al, 2011). Re-entry protocol to the mines was defined by the results of seismic monitoring in the Canadian mines (Vallejos and McKinnon, 2011). Seismic monitoring plays crucial role for planning of the mining operations and the rock support design (Wang and Ge, 2008; Ge, 2005).

Mine sites, especially in underground mines, are strongly affected by mining methods, and local and regional geological features such as discontinuities, stress changing. Moreover, seismic activities increase with the depth because of the increasing overburden pressure (Hasegawa et al. 1989; Young et al, 1989; Gibowicz and Kijko, 1994; Bollinger, 1989).

Rockburst hazard is not a problem for early days of any mines but it becomes huge problem with increase in depth as the rock system becomes more sensitive to redistribution of stresses (Alcott et al, 1998). There have been many studies on how seismic activity increases with the depth of mining level (e.g. Cao et al, 2009; Šílený and Milev, 2008).

The extraction ratio is another factor that affects induced seismicity. High extraction ratio could cause seismic events and rockbursts in the whole mine because of rapid redistribution of seismic energy (Brandy and Brown, 2004). Recent studies have

pointed out the importance of the geological structures but it also reported that two mine areas with the same geological structure and similar mining methods may result in different level of seismic activity (Gibowicz and Lasocki, 2001).

There are some differences and similarities between natural earthquakes and induced seismic events. Nests, swarms and sequences also follow higher magnitude seismic events in mines. However, the aftershock series are not like the ones after shallow natural earthquakes (Gibowicz, 1990). Unlike natural earthquake, induced seismic events ceases only a few hours after the events (Vallejos and McKinnon, 2011), and are not uniformly disturbed in space and time (Gibowicz and Lasocki, 2001).

Seismic networks record not only seismic activity but also blasts inside mining area. Blast events differ from the seismic events in such way that blasts are characterized by specific waveform, high energy and frequency and quick decay and seismic activity increases after blasts (Liu et al, 2013). In each case (after the production blast), the number of seismic events increase dramatically and the duration of the seismic activity and its subsequent decrease changes with respect to mining operations, geological conditions and damaged area due to the blast or previous cracks. However, if the blast charging is not enough or the distance between the blast and sensor locations is too long, many low magnitude events may not be recorded.



### 3. SEISMIC EVENT SOURCE PARAMETERS

#### 3.1 Seismic Waves

There are two main types of seismic waves – body and surface waves. The body waves can be separated into P (primarily, longitudinal) wave and S (secondary, shear) wave. Poisson first mentioned the body waves (Kulhanek, 1997). Surface waves are the second type and include Love (LQ) and Rayleigh (LR) waves. The diagram showing the type of particle motion of each one of the mentioned types is presented in Figure 3.1.

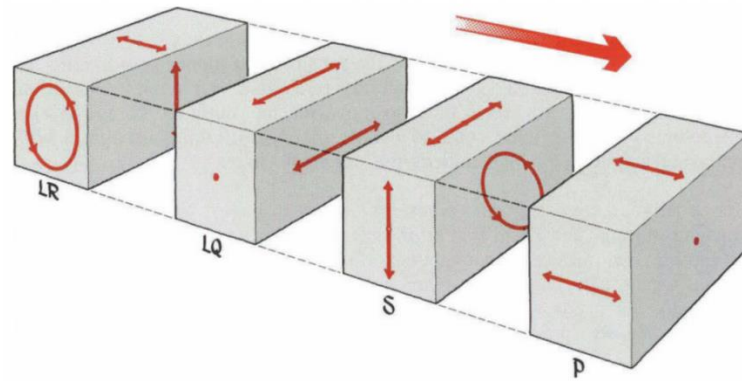


**Figure 3.1 :** Seismic wave's propagation (Kulhanek, 1997).

P wave travels through the body of the medium with particle motion along the path and it is the fastest wave. S wave particle motion is always perpendicular to the wave propagation and its velocity is approximately  $1/\sqrt{3}$  times slower than the velocity of P wave. Body wave's velocities could be defined by elastic moduli and density of medium. The velocities of body P- and S- wave are calculated by following equations:

$$\alpha = \sqrt{\frac{\lambda + 2\mu}{\rho}} \quad (3.1)$$

$$\beta = \sqrt{\frac{\mu}{\rho}} \quad (3.2)$$

where  $\alpha$  and  $\beta$  are P- and S- wave velocities, respectively,  $\lambda$  and  $\mu$  are Lamé constants, and  $\rho$  is the density of medium.

If seismic event occurs very close to the sensors, identification of P and S wave arrivals become harder (Bollinger, 1989) because of the small time interval between the arrivals. As seen in Figure 3.2 the time interval between P- and S- wave arrivals is distinguishable because the station is far enough from the source.

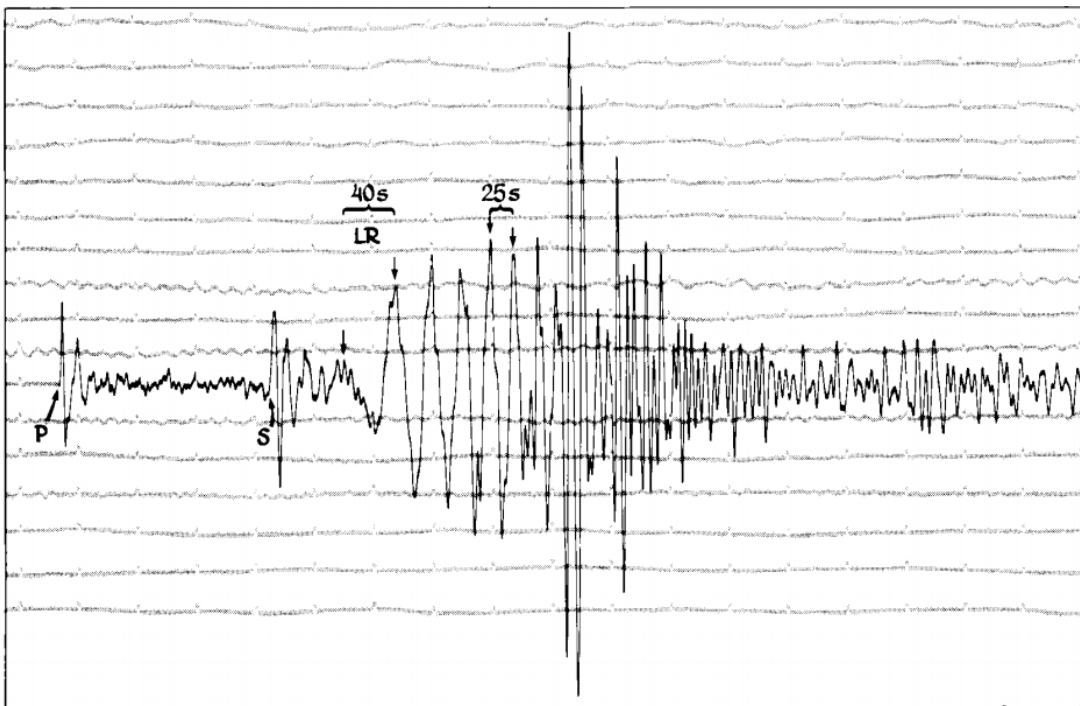


**Figure 3.2 :** Seismogram of the earthquake in northern Greece on May 23, 1978, magnitude  $M=5.7$ , focal depth is 9 km (Kulhanek, 1997).

Surface waves are the dominant waves on the seismogram. Their frequencies and amplitude are different from body waves. Surface waves generally occur at the layer interaction. The surface waves velocities can be calculated also from the medium physical properties. The particle motion of these waves is more complicated than body waves. It is uncommon to observe signs of surface waves in the records at mine scale seismological studies.



### 3.2 Kinematic Source Parameters

Kinematic source parameters are the hypocenter location and the origin time. In this part, the methodology for determination of these parameters based on defined arrival times of P and S waves will be explained.

The hypocenter (called also focus) refers to a point where the rupture on the fault during the earthquake starts. However, especially for big earthquakes, the center of earthquake describes where the energy begin to be released (Shearer, 2009). Hypocenter is defined by three coordinates (x,y,z) but the epicenter which is the projection of the hypocenter on the earth surface, is defined with two coordinates (x,y). A sketch with an epicenter and a hypocenter are shown in Figure 3.3.

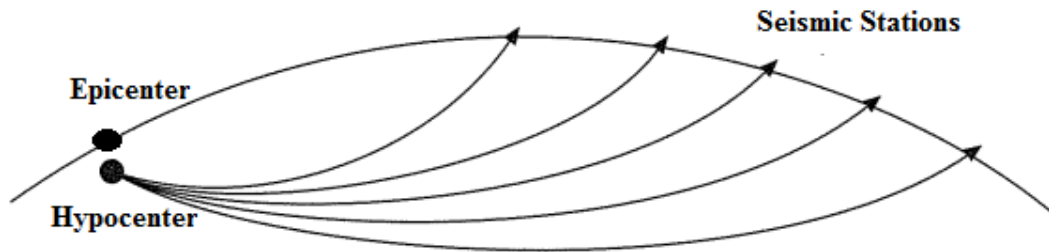


**Figure 3.3 :** Epicenter and hypocenter location (Stein and Wysession, 2003).

Travel time based precise earthquake location estimation has been a big challenge almost from the early days of seismology (Shearer, 2009). The time of the event (when the rupture starts) is called origin time ( $t$ ). To define the hypocenter location and the origin time it is necessary to use the theoretical travel times ( $t_i$ ) from the source (hypocenter, focus) to the  $i$ th seismic station (receiver). The theoretical arrival time of the seismic waves ( $t_d$ ) is defined as a sum of the origin time and the travel time as

$$t_d = t_i + t \quad (3.3)$$

Figure 3.4 shows a hypocenter (focus), an epicenter and a station and the ray path of either P or S waves for which the travel time is calculated in homogeneous medium.

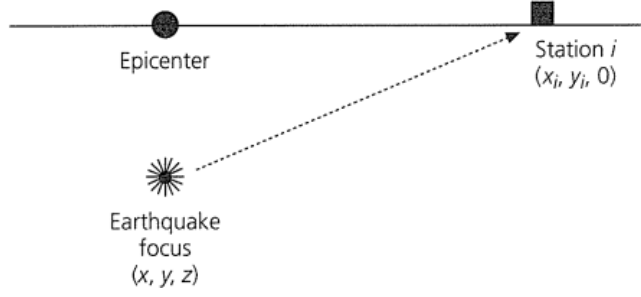


**Figure 3.4 :** Earthquake focus (hypocenter), epicenter and seismic station location and ray path between the focus and the station (Stein and Wysession, 2003).

Equation 3.3 can be re-written also with coordinates of the focus and receiver given in a vector form as

$$t_{di} = T(x, x_i) + t \quad (3.4)$$

where  $T(x, x_i)$  is the travel time between the hypocenter  $x$  and the receiver  $x_i$  and  $t_{di}$  is the theoretical arrival time for  $i$ th station.

Therefore hypocentral location and the origin time describe an earthquake (in terms of kinematic source parameters). In order to calculate these parameters, at least three station records are necessary, if the velocity model is known. An earth velocity model needs to be defined for travel time calculations. Model earth parameters are functions of model input (hypocenter location and origin time).

$$\mathbf{m} = (t, x, y, z) \quad (3.5)$$

Next step is to estimate predicted arrival times for each station. For  $i$ th station, predicted arrival time can be expressed as follows;

$$t_i^p = F_i(\mathbf{m}) \quad (3.6)$$

where  $F$  is a function of arrival times according to model parameters and  $t_i^p$  is predicted arrival time. The inverse problem can be described as finding model parameters from the observed arrival time. To solve the inverse problem minimum four stations are needed. Then the difference between predicted and observed arrival time differences will be calculated and this value is known as residual.

Once the travel times from an assumed earth model is calculated, the time residuals that are differences between observed minus calculated travel time are expected minimum. That is,

$$r_i = t_i - F_i(\mathbf{m}) \quad (3.7)$$

Since the  $F$  is not a linear function of the model parameters, an iterative solution is required to update the model parameters until minimum residual or some other criteria is obtained. To start with the iterative solution, an initial value for each model parameters has to be assumed (initial model) to obtain the theoretical travel time using.

$$t_i = T(x, x_i) + t = \frac{\sqrt{(x - x_i)^2 + (y - y_i)^2 + (z - z_i)^2}}{v} + t \quad (3.8)$$

where station coordinates are  $(x_i, y_i, z_i)$ , any point location is  $(x, y, z)$ ,  $t$  is the earthquake origin time,  $T(x, x_i)$  is travel time between station and hypocenter and  $v$  is velocity of medium.

Different methods can be used for calculation of the hypocenters and origin time. The most popular methods for homogeneous and 1D velocity models use different minimization techniques (e.g. Simplex method - Nelder and Mead, 1965). There is also a grid search method in which -equation 3.7 must be handled for all possible epicenter or hypocenter locations in a grid. It is obvious that error has lower value close to the source. The point or area with minimum error defines the possible location. It is expected that the error increases rapidly where grid points are getting far from the source (Shearer, 2009).

Different quantities like  $L_2$  norm have been used to measure the performance of the model given as (Ge, 2012). Error calculation by L2-norm is

$$\epsilon = \sum_{i=1}^n (t_i - t_i^p)^2 \quad (3.9)$$

where  $\epsilon$  shows the total error of all stations.  $\epsilon/n$  is called variance (Stein and Wyssession, 2003). Figure 3.5 shows how the error increases with respect to source location. The increasing number of stations and accuracy of picking the arrival times

increase the accuracy of the seismic location. Poorly assumed velocity model causes an increasing misfit between the observed and calculated travel times.

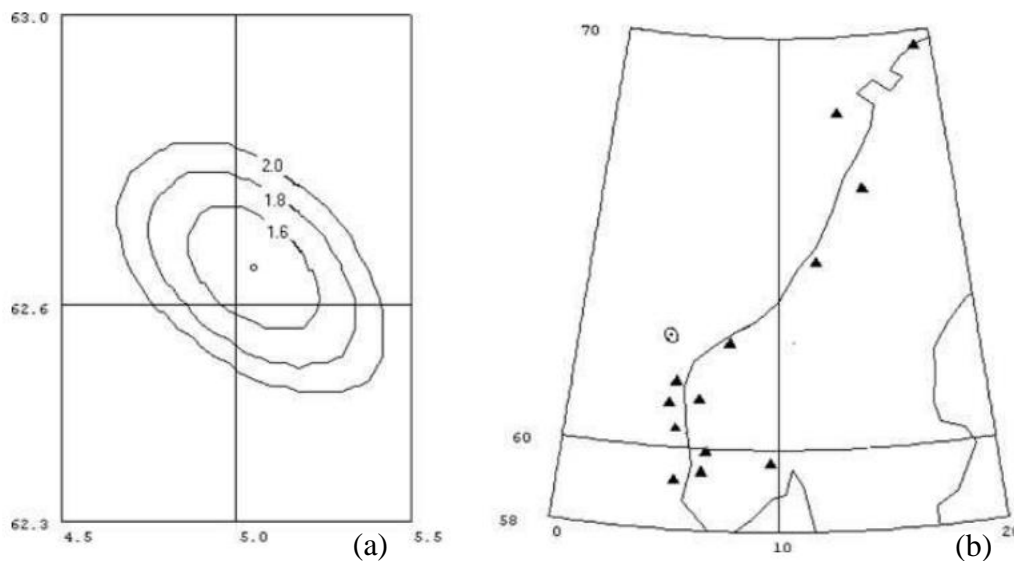


**Figure 3.5 :** (a) L2-norms contours from a grid search location of an earthquake off western Norway. The grid size is 2 km. The circle in the middle indicates the point with the lowest value (1.4 s). (b) The location of the earthquake and the stations used. (Havskov and Ottemöller, 2010).

Microseismic event source location determination is a little more complicated because mine areas have relatively small and the velocity estimation is difficult because of complex structure (Ge and Kaiser, 1991). The expectation of the location error would be less than few meters in the best case (Kijko and Sciocatti, 1995).

A different approach is accepted in some mines for calculation of the hypocenter locations. Due to the production, the rock mass becomes more complex and the local stresses are re-distributed. This causes seismic velocities to change with time within a limited volume. Therefore, a routine source location procedure may not be suitable. In order to reduce the travel time residual, for example the IMS Trace software, which is a data processing software especially induced seismic event, uses the Nelder-Mead algorithm but the velocities along the path for each pair of source and sensor are calculated by a special procedure for every case, depending on the location of the ray paths and the time of the event. Information from recorded so called “calibration blasts” is used for the purpose. By using calibration blasts (with known source location), the P-wave (or S-wave) velocity for each sensor is calculated via the following equation:

$$v_p^i(x_a) = \frac{\sum_{j=1}^n 1/d_j^2 v_p^{ij}}{\sum_{j=1}^n 1/d_j^2} \quad (3.10)$$

where  $v_p^{ij}$  is the inverted P-wave apparent velocity of site  $i$  for calibration blast  $j$ ,  $d_j$  is the distance between calibration blast  $j$  and point  $x_a$  is tested as a hypocenter. The same formula is valid also for S-wave velocity. This processing approach helps to reduce the location error for induced seismic events.

### 3.3 Dynamic Source Parameters

A seismogram does not only contain information about the source locations, and timing but also describe the mechanism and other source parameters of the events (Cao et al, 2009). Such as, seismic moment, energy and energy ratio, stress drop, corner frequency etc. are called dynamic source parameters. Seismic source parameters as seismic moment, radius and stress drop are estimated by Brune (1970, 1971) and/or Madariaga (1976) models. Both of these models assume that the stress is uniformly distributed over the source area. Brune model assumes circular dislocation and Madariaga's model is based on circular crack with finite rupture velocity (Gupta and Chadha, 1995). A modification of the Brune model is also used – Brune et al (1979), Hartzell & Archuleta (1979) by taking into consideration the relationship of S-wave far-field corner frequencies to the source dimensions and the stress drop and source dimensions.

Seismic event time, location, seismic moment and radiated energy are independent parameters, although source radius, average slip, stress drop and apparent stress directly linked with the waveform and corner frequency of the spectra (Gibowicz and Lasocki, 2001). The parameter calculation is a routine procedure for seismic events with longer period waveform however this simple task becomes a challenge for events with short period waveform, and weak seismic events, such as, induced seismic events (Šílený and Milev, 2008). Obviously, these dynamic parameters cannot be determined without knowledge of attenuation (Havskov and Ottemöller, 2010). To start the process of determination of the dynamic source parameters of any seismic event, attenuation correction must be applied on the data.

The number of sensors is important for determining source parameters precisely. Minimum 5 to 10 three component stations are needed to obtain reliable solution on the source parameters (Mendecki and Niewiadomski, 1997). Daily data analysis at mines mainly focuses on seismic event locations, clustering of the events, their frequency content, and energy index (Alcott et al, 1998).

### 3.3.1 Magnitude

Seismic event magnitude is linked to the amplitude of recorded seismogram. The general relation between magnitude and amplitude for natural earthquakes is

$$M = \log(A/T) + Q(h, \Delta) + C \quad (3.11)$$

where  $A$  is maximum amplitude,  $T$  is dominant period,  $Q$  is correction for amplitude decrease with distance  $\Delta$  is attenuation,  $h$  is the source depth, and  $C$  is a regional scale factor (Shearer, 2009).

Magnitude scale is a logarithmic scale. One unit increment in magnitude represents 10 times higher or lower amplitude (Shearer, 2009).

#### 3.3.1.1 Local magnitude

Local magnitude was defined for the first time by Charles Richter for California earthquakes in 1935. The method uses the highest amplitude on the record by Wood-Anderson seismograph. The attenuation must be corrected before calculating the arrival time differences between S and P wave. Figure 3.6 shows how a local magnitude is calculated from a seismogram (Shearer, 2009). Local magnitude  $M_L$  equation is

$$M_L = \log(A) + \log(A_0(D)) \quad (3.12)$$

where  $\log(A_0(D))$  is the correction for attenuation for epicenter/hypocenter distance  $D$  and  $A$  is the measured amplitude.

A modified version of Equation 3.12 is

$$M_L = \log(A) + a \log(\Delta) + b \quad (3.13)$$

which accounts for the geometrical spreading,  $a$ , and the attenuation  $b$  (Havskov and Ottemöller, 2010). The parameters  $a$ ,  $b$  and  $\log(A_0(D))$  change from region to region and have to be re-estimated. Local magnitude is used in several aspects. It could be related to the structural damages in mines or mining activities.

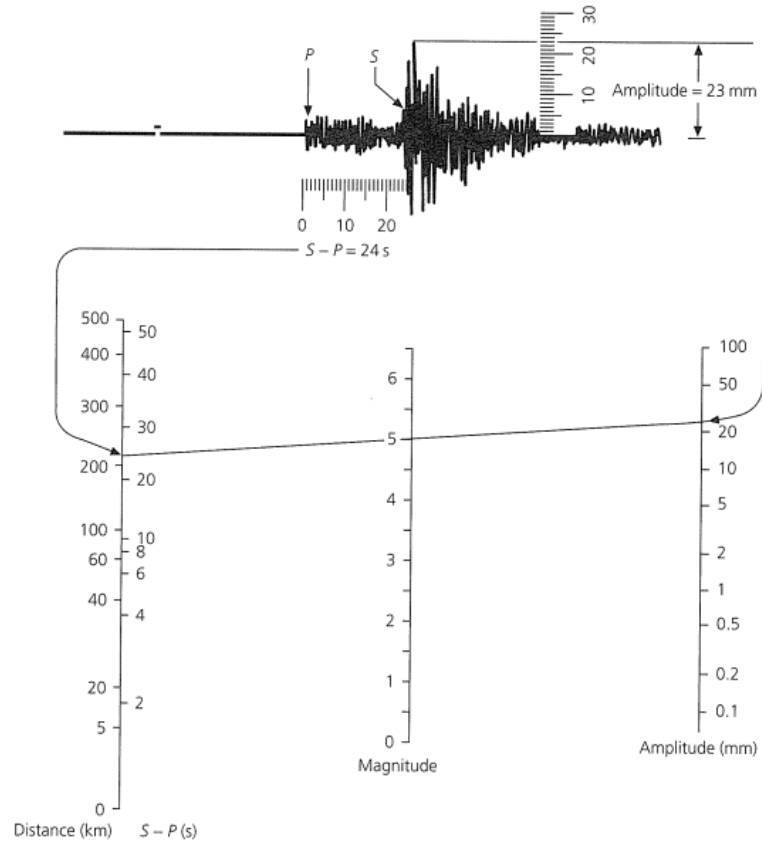


**Figure 3.6 :** Local magnitude estimation.

### 3.3.1.2 Modified local magnitude

In IMS Trace software a modified version of the local magnitude is used. It is defined by the formula

$$M_L = a \log E + b \log M_0 + c \quad (3.14)$$

where  $a$ ,  $b$ , and  $c$  are constants specific for the mine  $E$  is the energy, and  $M_0$  is the seismic moment.

### 3.3.1.3 Moment magnitude

Use of the local magnitude may not be reliable since it exhibits several disadvantages. The problem arises at quantifying the amplitude that is related to the frequency.

The moment magnitude defined by Hanks and Kanamori (1979) is

$$M_w = \log(M_0)/1.5 - 6.07 \quad (3.15)$$

where  $M_0$  is the seismic moment [N.m].

Much more data processing is needed to estimate seismic moment and moment magnitude than the local magnitude (Stein and Wyession, 2003). Moment magnitude values are generally different from local magnitude values.

### 3.3.2 Seismic wave spectrum and corner frequency

Corner frequency could be estimated by Brune model. Brune model describes the plateau  $\Omega_0$  and corner frequency  $f_0$  (Gibowicz and Kijko, 1994). Plateau is the low frequency level of the spectra and the corner frequency the frequency estimated approximately at half of the amplitude of the flat level (Havskov and Ottemöller, 2010). Figure 3.7 shows displacement and acceleration spectra. The flat part of the displacement spectrum links with seismic moment and high frequency slope usually is accepted as -2 (Havskov and Ottemöller, 2010).

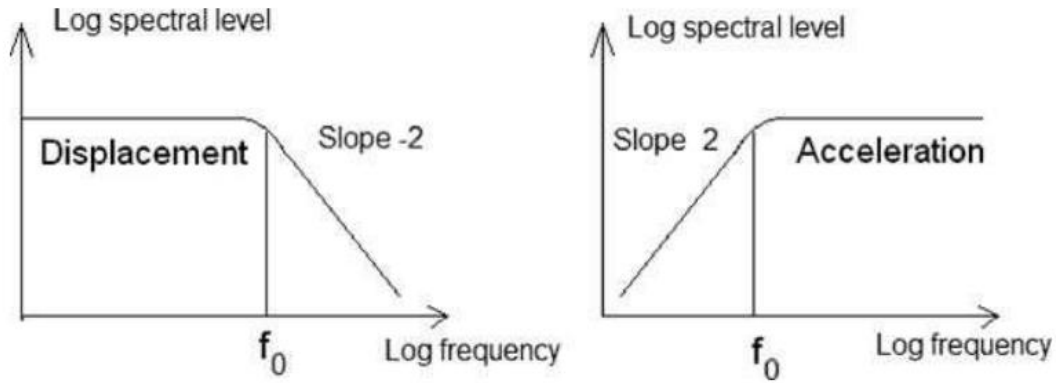


**Figure 3.7 :** Theoretical displacement and acceleration spectrum by Brune Model (Haskov and Ottemöller, 2010).

The equation for displacement spectrum is

$$S(f) = \frac{M_0}{\left(1 + \left(f/f_0\right)^2\right) 4\rho\pi v^3} \quad (3.16)$$

where  $M_0$  is the seismic moment (Nm),  $\rho$  is the density ( $\text{kg/m}^3$ ),  $f_0$  is the corner frequency (Hz) and  $v$  is the velocity (m/s) of P- or S- wave, depending on the spectrum.



Equation 3.16 does not include the radiation pattern effect and attenuation. Gibowicz and Lasocki (2001) mentioned that P wave corner frequency is higher than S wave corner frequency. Figure 3.8 shows a real data displacement spectrum as an example.

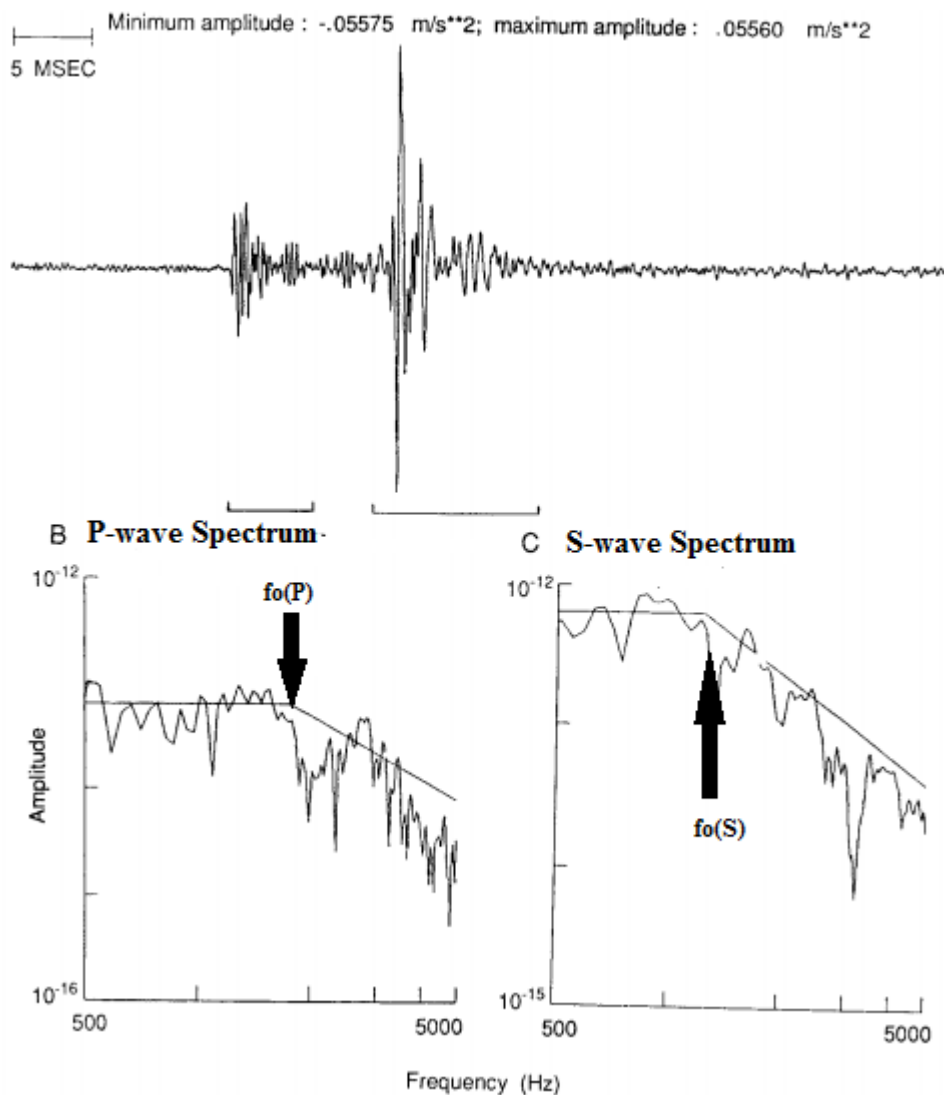


**Figure 3.8 :** Example of different type of displacement spectra, P- and S- waves and corresponding corner frequencies (Modified from Gibowicz and Kijko, 1994, modified).

### 3.3.3 Seismic moment and potency

A scalar seismic moment is defined as seismic moment is a measure of the size of an earthquake based on the area of fault rupture, the average amount of slip, and the force that was required to overcome the friction sticking the rocks together that were offset by faulting. As described, the seismic moment is;

$$M_0 = \mu \times a \times D \quad (3.17)$$

where  $\mu$  is rigidity,  $a$  is the area of the fault and  $D$  is slip on the fault. Seismic moment could be also estimated from the low frequency level of the far-field displacement spectrum with the geometric spreading taken into account as

$$M_0 = \frac{\Omega_0 4\pi\rho v^3}{R_{\theta\phi} \times 2.0 \times G(\Delta, h)} \quad (3.18)$$

where  $G(\Delta, h)$  is the geometric spreading,  $\Omega_0$  is the low frequency level of the displacement spectrum,  $\rho$  is density,  $R_{\theta\phi}$  is the radiation pattern of P- or S-wave and  $v$  is the P- or S- wave velocity of medium at the source. Geometric spreading  $G(\Delta, h)$  depends on  $\Delta$ , epicentral distance and  $h$ , hypocentral depth. For simplicity  $G(\Delta, h)$  function can be replaced with  $1/r$ . Then equation 3.18 becomes

$$M_0 = \frac{\Omega_0 4\pi\rho v^3 r}{R_{\theta\phi} \times 2.0} \quad (3.19)$$

Average radiation patter is found between 0.55 and 0.85 in the literature moreover it is 0.55 and 0.63 for P and S waves, respectively in the earth's crust (Aki and Richards, 2002).

Potency describing the source strength is the relation between scalar seismic moment and potency is;

$$P = \frac{M_0}{\mu} \quad (3.20)$$

Where  $M_0$  is the seismic moment and  $\mu$  is the rigidity.

### 3.3.4 Energy

Seismic energy refers to the energy released during fracturing and frictional sliding when elastic strain transforms into inelastic strain (Mendecki, 1994).

$$E = -2\gamma_{eff} FA + \frac{1}{2} \int_{FA} \Delta\sigma_{ij} u_i n_j dFA + \int^{t_{cs}} dz \int_{FA(t)} \dot{\sigma}_{ij} u_i n_j dFA \quad (3.21)$$

where effective source energy is  $\gamma_{eff}$ , the difference between the final and the initial stress is  $\Delta\sigma_{ij}$ , the fracture area with the displacement  $u_i$  is  $FA$ , unit vector normal to the fracture plane is  $n_j$ , source duration is  $t_{cs}$  and  $\dot{\sigma}_{ij}$  is traction rate. Although there are seismic energy losses because of friction during sliding, the released energy is always proportional to the stress drop, displacement and fault geometry. The total energy of seismic event is always a sum of the energy of all waves (Alcott et al, 1998). Energy estimation is harder than seismic moment calculation, because it relates to high-frequency the slope of the displacement spectra (Stein and Wyession, 2003).

Seismic energy can be calculated via different formulas IMS Trace software uses a different equation for seismic energy calculation (from Kanamori and Anderson (1975)) of the induced seismic events.

$$E_{P,S} = 4\pi\rho v_{P,S} A_{P,S} R^2 \int_0^{t_s} U_{corr}^2(t) dt \quad (3.22)$$

Where  $\rho$  is the rock density ( $\text{kg/m}^3$ ),  $v_{P,S}$  is the P- and S-wave velocity in the rock (m/s),  $R$  is the distance from the source to sensor (m),  $U$  is the energy of the velocity of ground motion, and  $A_{P,S}$  is the average radiation pattern.

The energy ratio  $E_s/E_p$  is used as a proxy of the mechanism of the source. If  $E_s/E_p$  is lower than 10, the source has non-shear mechanism (Gupta and Chadha, 1995). If  $E_s/E_p > 10$  the source has shear mechanism. The threshold between shear and non-shear events is not well defined. It varies around 8 to 10. Cao et al (2009) described the characteristics of two types of events at Sanhejian Mine data, China with respect to waveform solution in the following way:

- Non-Shear Event: low dominant frequency, long wave duration, not strong S component;
- Shear Event: strong and dominant S wave, short wave duration, large amplitude.

### 3.3.5 Apparent stress

The apparent stress ( $\sigma_a$ ) describes how much energy is radiated per unit volume during inelastic coseismic deformation and it is a function of seismic energy and the seismic moment (Wyss, 1970; Mendecki, 1997).

$$\sigma_a = \zeta \bar{\sigma} = \mu \frac{E}{M_0} \quad (3.23)$$

where  $\zeta$  is the seismic efficiency and  $\bar{\sigma}$  is the average stress,  $E$  is the seismic energy, and  $M_0$  is the seismic moment.

The apparent stress associates with the geological features of the medium. If seismic event occurs in very soft geological material that means stress changes take long time and this event has higher seismic moment but lower energy, hence the apparent stress of event will be low (Mendecki, 1997). Apparent stress is also used to describe stress changes before larger seismic events (Liu et al, 2013).

### 3.3.6 Stress drop

As a general term stress drop indicates the stress differences along the fault before and after a seismic event (Gibowicz, 1998) or average stress releases across the fault (Gupta and Chadha, 1995).

$$\Delta\sigma = \frac{7}{16} \frac{M_0}{r_0^3} \quad (3.24)$$

where  $M_0$  is the seismic moment and  $r_0$  is the source radius. Stress drop depends on the corner frequency and source radius (Gibowicz, 1998). Gibowicz (1975) indicated that the stress drop increases with seismic moment.

Stress drop, which can be calculated by observation of rupture on the surface of the Earth, is an important parameter for scaling relationships. However, the case of small events fault dimensions have to be calculated by far field observations of the seismic waves using the estimation source radius (Stein and Wyssession, 2003)

### 3.3.7 Source radius

Source radius is a function of corner frequency, and therefore, it is a model dependent parameter (Young et al, 1989). Source radius could be calculated either from P-wave or S-wave spectrum (Molnar and Wyss, 1972). Source radius equation according to Brune (1970) is given by;

$$r_0 = \frac{2.3k\beta}{2\pi f_c} \quad (3.25)$$

where  $r_0$  is the source radius, and  $\beta$  is S-wave velocity and  $f_c$  is corner frequency of P- or S-wave (Molnar and Wyss, 1972). The k parameter is 0.5 and 0.37 (for Brune Model) and 0.33 and 0.22 (for Madariaga Model) for P and S wave, respectively. The radius calculated with the last model have values between the values calculated with Brune and Madariaga models. The source radius usually is estimated with large uncertainty.



## **4. IMS TRACE SOFTWARE**

### **4.1 General Information**

IMS Trace is software which is designed for processing of seismic records (waveform) from induced seismic events. Trace is developed by the Institute of Mine Seismology (IMS) (<http://www.imseismology.org/>) an independent private company which focuses on developing new methodologies, technologies, monitoring and modelling services for seismic responses of mining areas.

IMS Trace is available for Windows and Linux operation systems. One of the most important features of Trace is its processing capability of the seismic waveforms and calculation of the seismic event parameters, automatically or manually. Data processing is quite straightforward with Trace; the most critical part is picking of arrival times of body waves. After this step the event location and source parameters are calculated by Trace automatically but some adjustment of the arrival times, for specific sensors, velocity and attenuation models are needed for. All source parameters, in Trace mentioned in Chapter 3, are calculated.

Trace has filtering options for the preprocessing step. Notch filter for 50/60 Hz that is used when needed. Other corrections such as attenuation of the waveform, and anti-aliasing were applied before data preparation stage. In Trace are already corrected for the instrument response and are in m/s (velocity).

IMS Trace follows the rules of seismology such that, P wave velocity must be higher than S wave and P wave arrival must be defined before S wave. Moreover, Trace does not save any processing steps until event saved manually. If seismic event is recorded by more sensors, the result will be more accurate. To get minimum result one P and S wave must be picked.

### **4.2 Data Processing**

IMS Trace is a user-friendly program. Each components of the program can be added or removed to the window easily. Moreover, event records can be visualized in several

ways, and phase arrival (P or S) can be picked or changed to reduce the residual error.

Figure 4.1 shows a regular Trace-window.

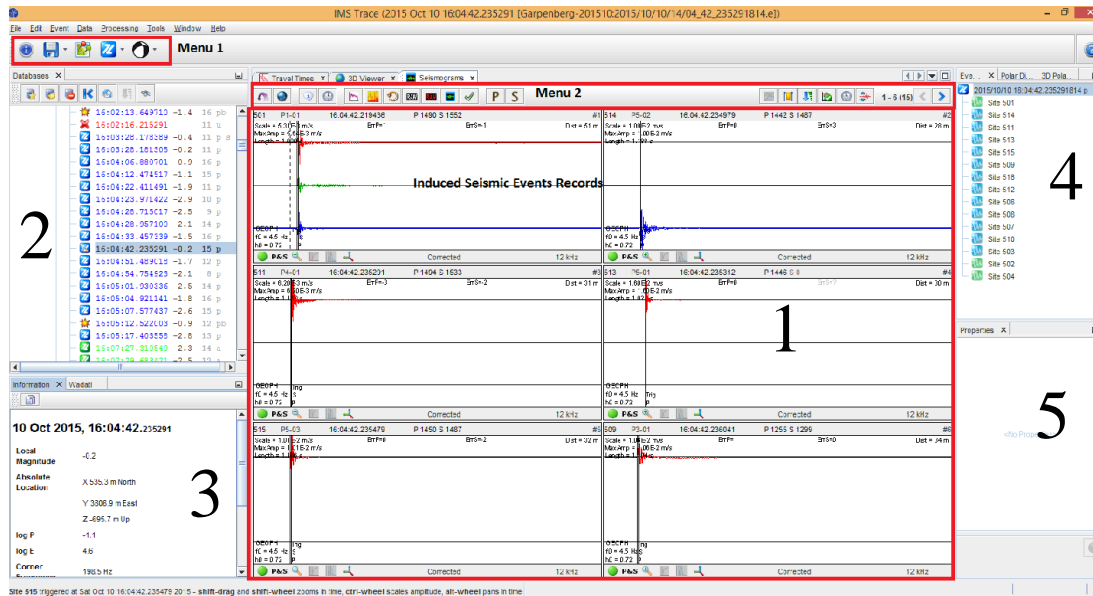


**Figure 4.1 :** IMS Trace windows with waveforms from six sensors.

There is five sub-window seen on Figure 4.1. Each of them is needed during data processing of induced seismic events. The event waveforms are visible on Window-1. The data is selected in database on Window-2. The general information and/or other necessary tools such as FFT, and Wadati diagram locate on Window-3. Window-4 shows all sensor in selected event. Window-5 is optional, any tools in the Tool menu can be opened there or if any sensor selected on Window-4, options will display in Window-5.

Waveform visualization (Window-1) and processing has two options: individual seismograms for one or six sensors and all seismograms in order of sensor ID, epicentral or hypocentral distance (called Travel-Time option).

A useful tool is the polar diagram that shows the polarization of seismic waves within chosen time interval, e.g. P- or S-wave, noise (Window-5). It can be used to define the back azimuth (the azimuthal angle between the sensor and the source).

The Event Processing tool has three options: Perform Location, Perform Source and Mechanism. The first option is for calculation of hypocenter location, the second one for calculation of all dynamic source parameters, and the third one – for calculation of



the seismic moment tensor or source mechanism. Only the first two options are used in this study.

After visualization and processing, an event can be saved in the original database as Accepted (for induced seismic events), Marked as Blast (if blast features are observed), Rejected (for noise accidentally recorded as event) and Rejected as Blast.

Event locations and source parameters are calculated based on P and S wave arrivals. Not only induced seismic events but also recorded blast events by the seismic system could be processed by Trace.

For picking the arrival times seismograms from triaxial sensors can be viewed in the original form as three traces (X,Y,Z) or (E-W,N-S,DOWN/UP) for each component (Figure 4.2 a). They could be also automatically rotated into a local coordinate system with (Radial, Transverse, Z) (P-SV-SH) components (Figure 4.2 b). The orientation of the local coordinate system is defined by the polarization of P-wave. All parameters in this window are marked by a capital letter in red. The elements are defined in Table 4.1.

The trace window can be modified to zoom into specific section of the record to pick the arrival times, the polarities of P- and S-wave, etc. All different views help to process data correctly.

The areas outside the red square on Figure 4.1 could be designed by the analyst's needs. Database (Window 2) and Information (Window 3), which are located in the left column on Figure 4.1 are important; database displays the events in chronological order of day and time. General information, source parameters are displayed in the Information Window. These options could be visualized in different ways and the windows can be displayed or removed. In this way, it is easy to handle the events in a different way and keep processing under the control.

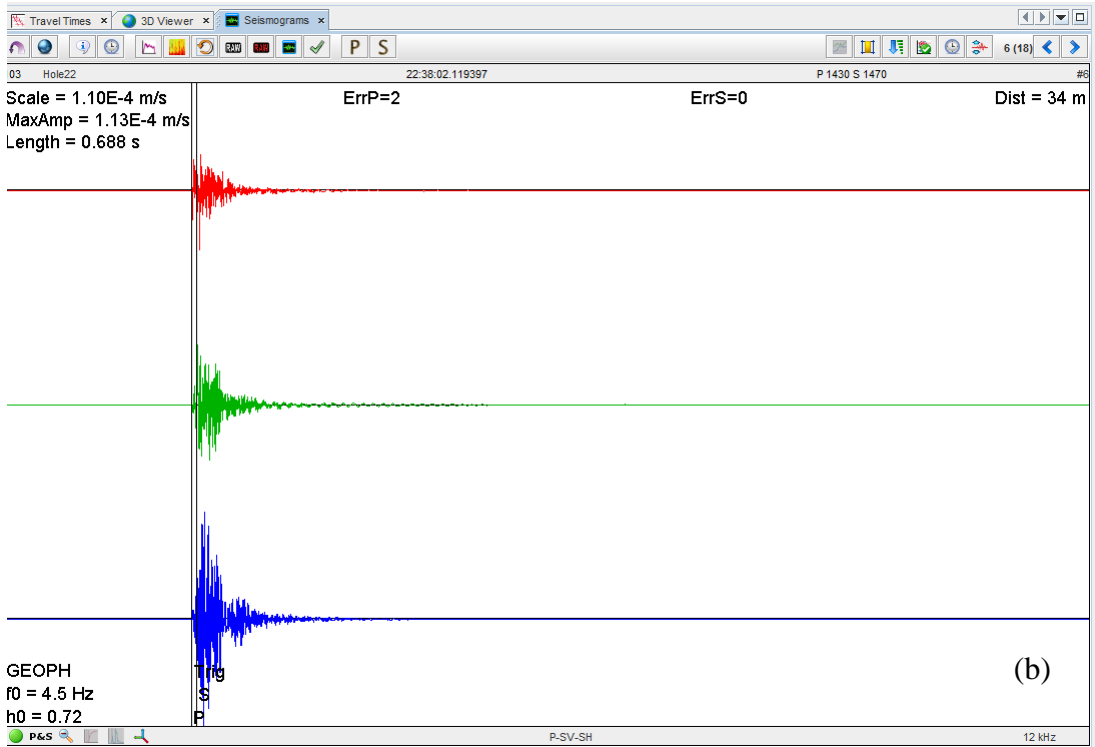
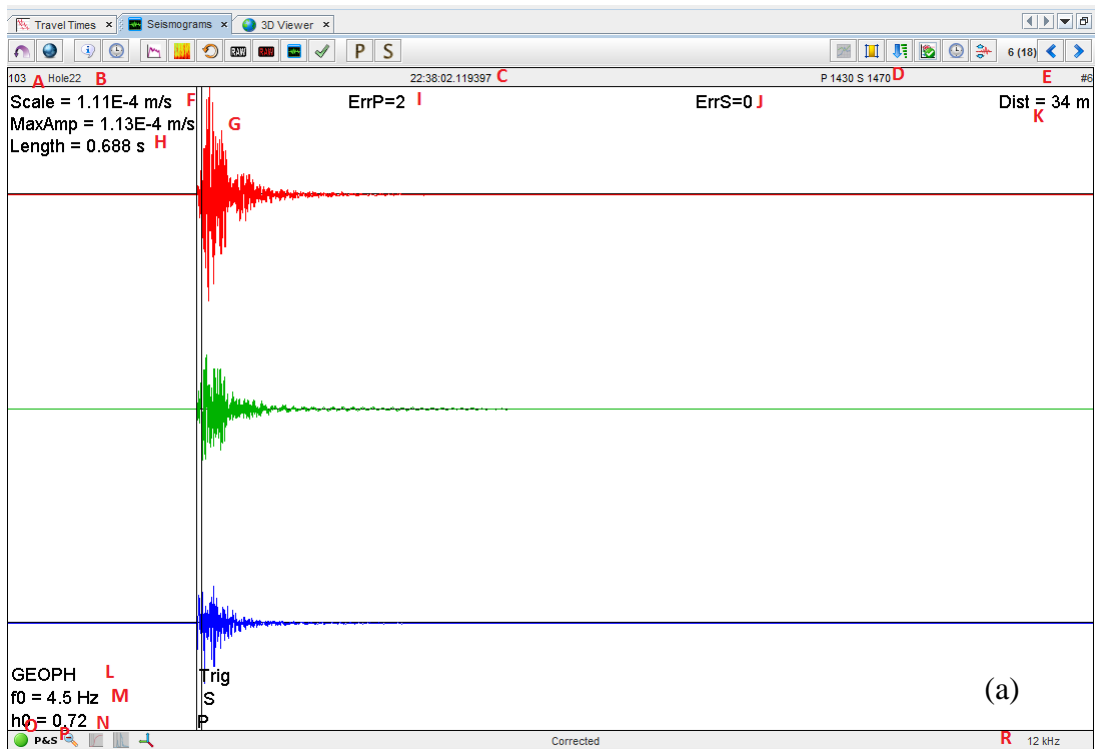


**Figure 4.2 :** Seismogram view. (a) Normal view and (b) Rotated view.

**Table 4.1** : Explanation of abbreviations on the seismogram screen on Figure 4.2(a).

<b>ID</b>	<b>Explanation</b>
A	Site Identification Number
B	Site Name
C	Trigger Time
D	P and S Wave Sample Number
E	Site arrival order
F	Scaling Factor
G	Waveform Amplitude Scale
H	Length of Seismogram
I	P wave error (meter)
J	S wave error (meter)
K	Distance from site to seismic source location (m)
L	Sensor type
M	Sensor frequency
N	Sensor damping
O	Accepted or rejected seismogram
P	Error types
R	Sampling rate at which the seismogram was recorded

A seismic event is selected for processing from a Database. The event name contains the time of the triggering and it is in a format hh:mm:ss.ms. If the event has been processed already the magnitude would be seen next to the event name.

Before starting processing an event, event records should be checked. Some of events might be masked by noise as seen in Figure 4.3. Two different ways could be followed under these circumstances. If only one sensor record is pure noise, the sensor can be disabled. If there are not so many useful records the whole event can be rejected. However, if some body waves could be visible on at least three or four sensors, phase picking might be considered.

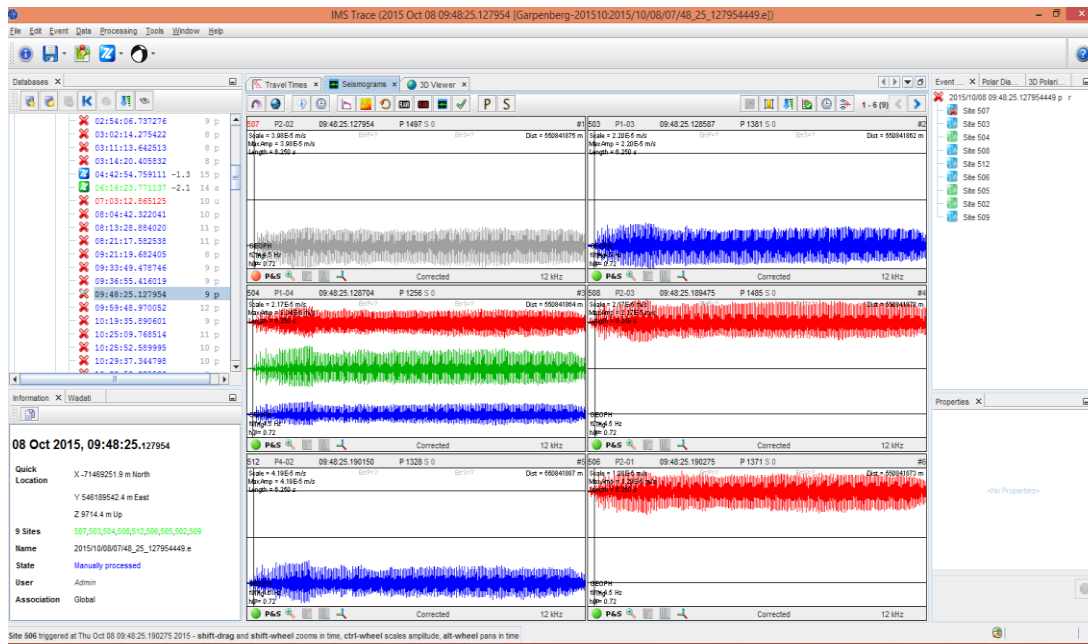


**Figure 4.3 :** Example of noise data (all sensors).

This view with six sensor records is not good enough during the processing but it gives an idea about quality of the records and roughly about P and S wave arrivals. Figure 4.4 shows single seismogram display with all three components together. To start processing the components have to be separated (Figure 4.5). On this view each component has different color. These colors represent N-S, E-W and Down-Up component as red, green, and blue color, respectively.

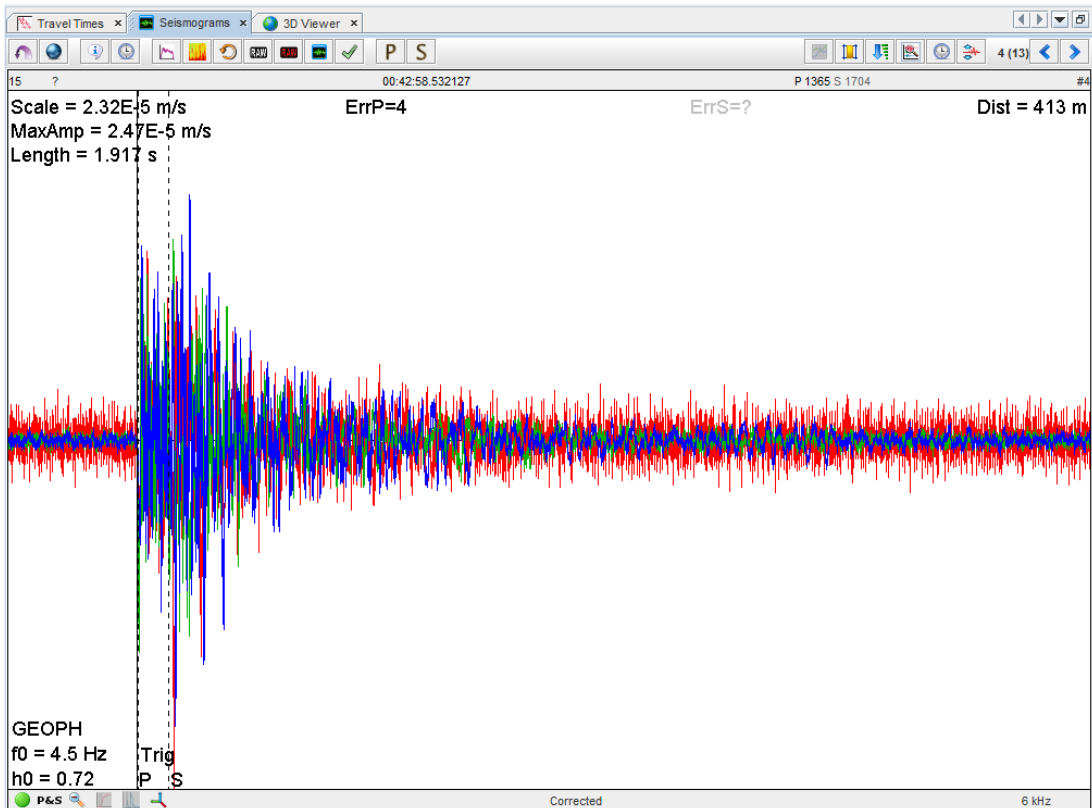


**Figure 4.4** : Example of view with unseparated seismogram.

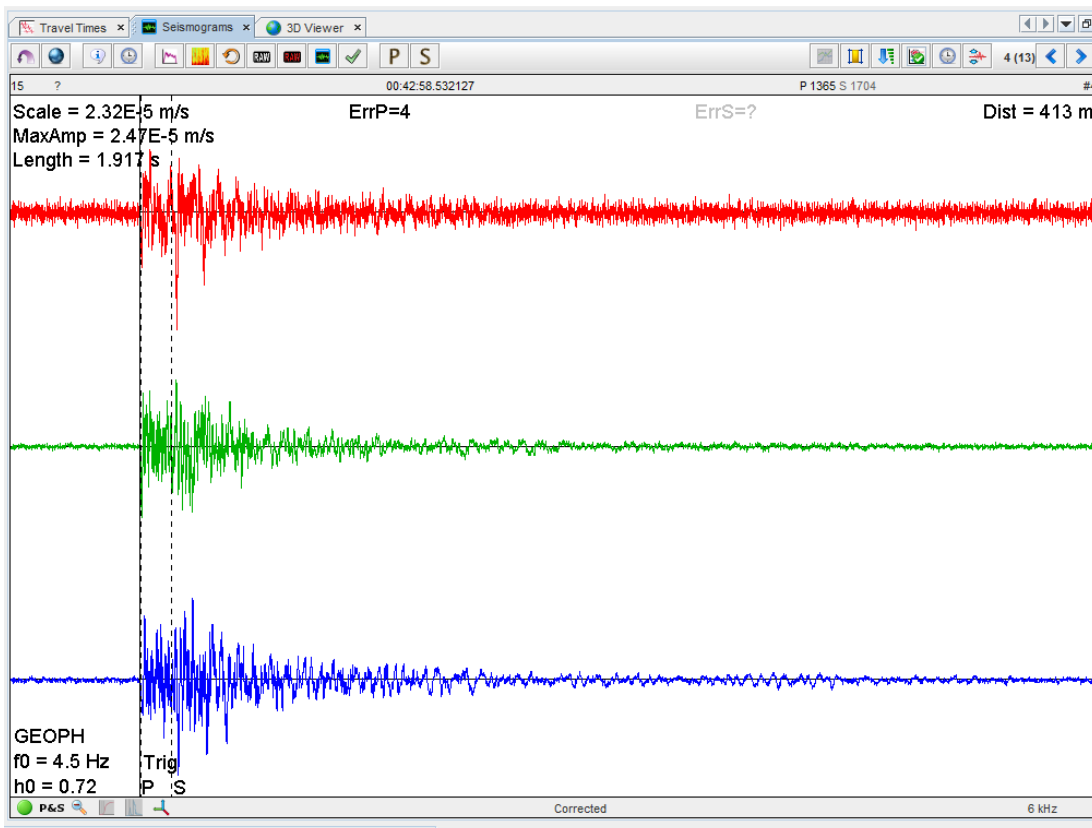


**Figure 4.5** : Example of view with separated seismogram.

Even these steps are not enough for picking first arrival with high accuracy because the record of the seismic waves is too squeezed. Seismogram can be enlarged, zooming into a selected portion (Figure 4.6). Zoom in provides comfort for the user to identify first break.

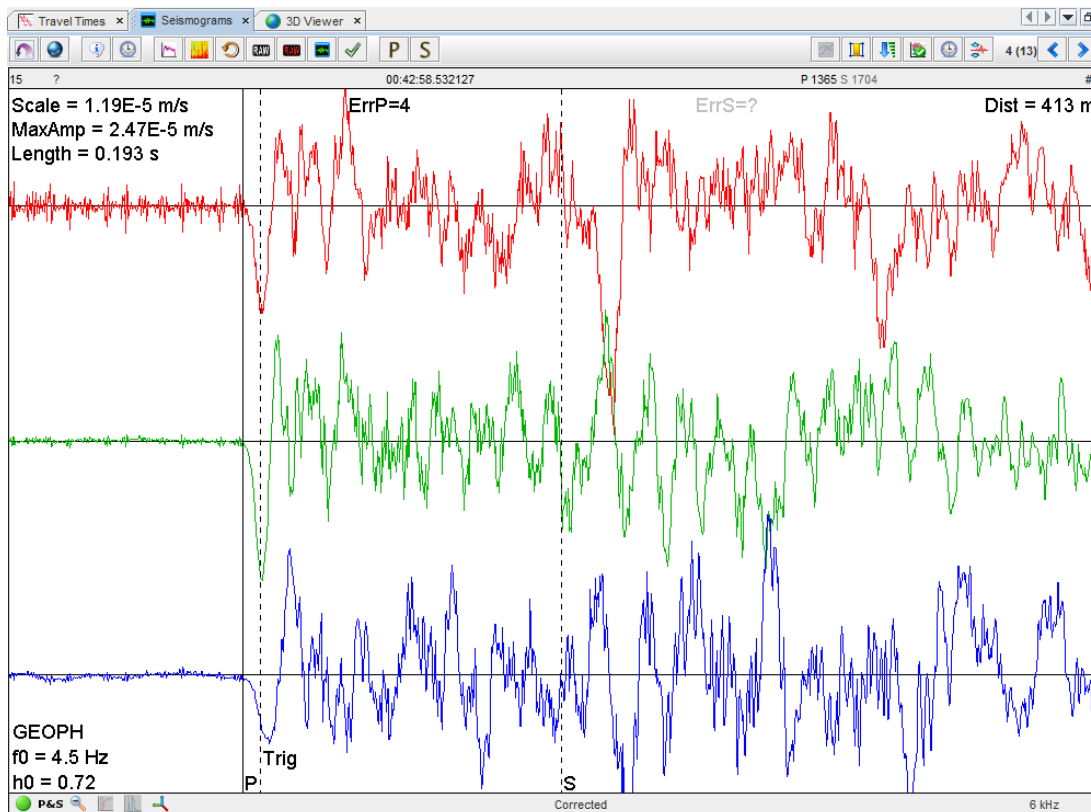


**Figure 4.6:** Example of enlarge a seismogram (zoom in).

If we have only one-component seismogram, picking, especially S arrival, depends on our knowledge and experience. However, three component data could be rotated to P-SV-SH orientation (local coordinate system) to pick the S-wave arrival with more confidence. In this case, the first component, which represents the radial component, should be used to pick P-wave. On this component P wave should be clearly visible. The second and third components represent the transverse components where SV and SH waves, respectively should be visible. If the record is rotated, the bottom-middle text “Corrected” becomes “Rotated” (Figure 4.2 a and b).

Due to the anisotropy, SV and SH waves real velocities might be different and SV wave could travel faster than SH wave and the arrival times on these two components to be different. This very first arrival of P- and S-wave (phase picks) is very important because the location calculation is based on it.

### 4.3 Perform Location

After picking of all possible P and S wave arrivals on all records of the event, the hypocenter location is calculated by pressing the 'Perform Location' icon in the Menu and a table with the result and the error of the location as well as the residual for each individual phase appears on the screen (Figure 4.7). This table can be used to verify and adjust the arrival times wherever possible and to reduce the error (residual) of the hypocenter calculation.

The errors on P- and S- wave is given without units. These errors just point out the misfit between programmer phase picking and calculated P- and S- wave arrivals. Negative errors mean that programmer phase picking is earlier than calculated one, and positive number indicates that calculated arrival time by P- and/or S- wave arrival picking are late than calculated arrival time. On the other hand, total error is given in percentage and called AHD (average hypocentral distance). The value of AHD also gives an idea about accuracy of phase picking. The aim is to be kept it less than 5%.

If sensors and source location are close, reducing P- and S- wave arrival time errors even with one sample might have a very large effect on the location. The relative effect of the arrival time error on the hypocenter decreases when S-P arrival time or distance increases.

An example for the event at 16:04 on October 15, recorded by the local seismic system in Garpenberg mine is used to describe the effect of arrival time picking on hypocenter location calculations. Next five figures are designed to explain the way of reducing the hypocenter residual. They explain in details the procedure followed later in Chapters 5 and 6. Some S arrivals were not picked because they were not clearly visible. Figure 4.7 shows the arrival times picked for sensor 511 and the first calculation of the hypocenter

Correction of phase picking (arrival time picking), should be done step by step. Each time only one arrival must be corrected because the residuals for the other arrivals will be recalculated depending on it and the residual and the sign can change. It is important to check all arrivals with larger residuals and first to correct them one by one.

After the first hypocenter calculation Site 508 had distance residuals -4 and -11 respectively for P- and S-wave (negative sign means that the arrival was picked earlier

than the calculated arrival time) and the total residual was 3.8 m (or 9.3% ADH) (Figure 4.8). After the S-wave arrival was corrected as seen on Figure 4.8, the S-wave residual decreased to -3 and the total was residual reduced to 8.5% ADH (Figure 4.9).

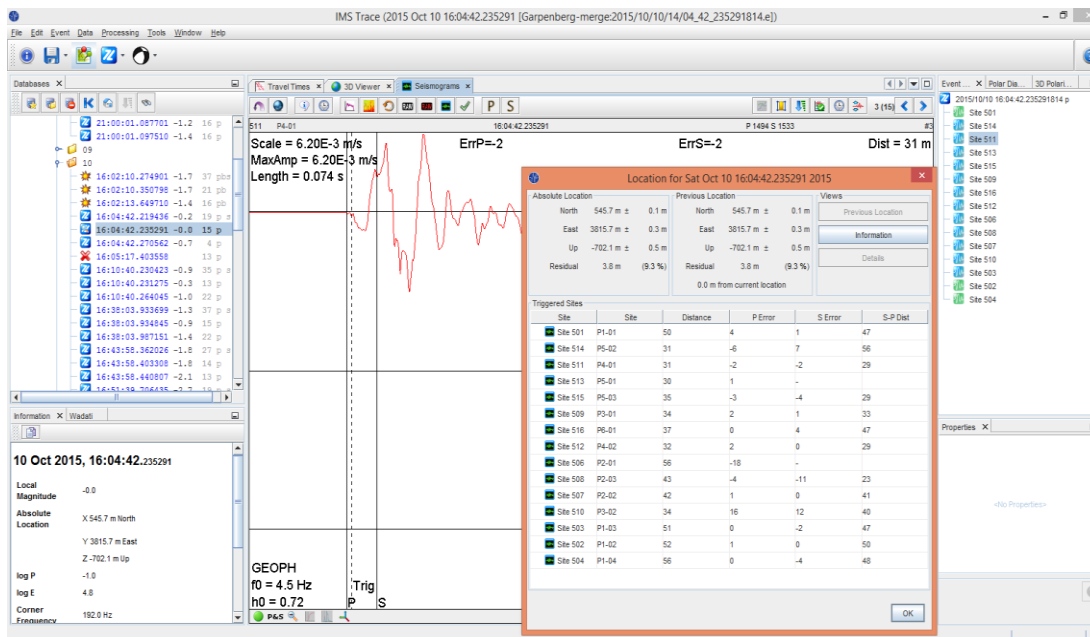


Figure 4.7 : The hypocenter location after the first phase picking.

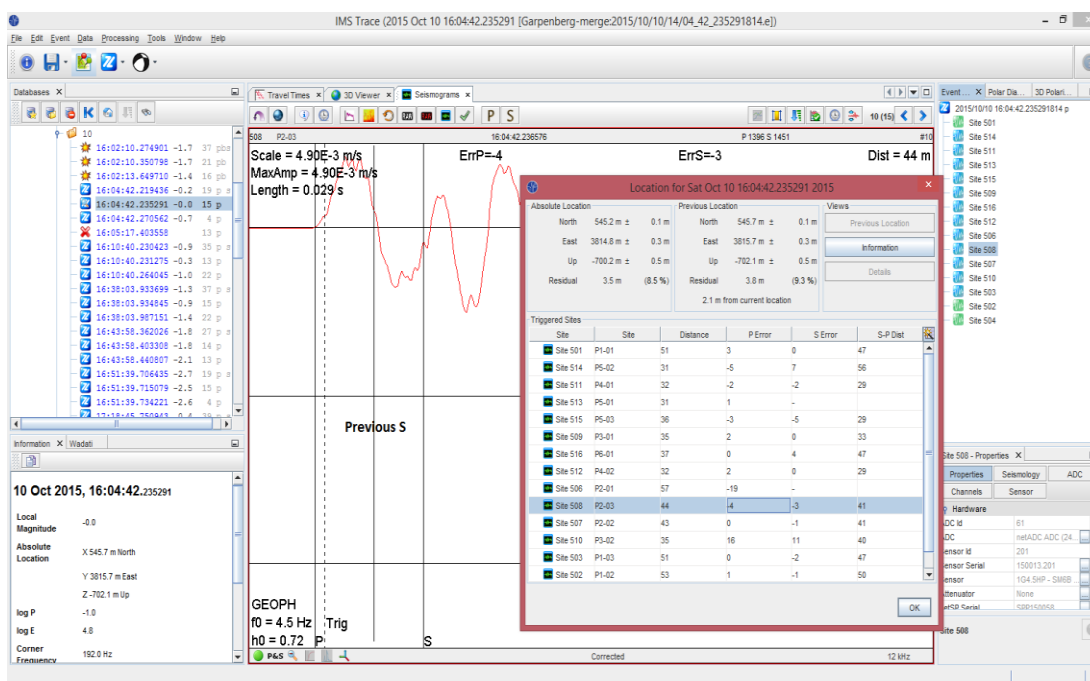
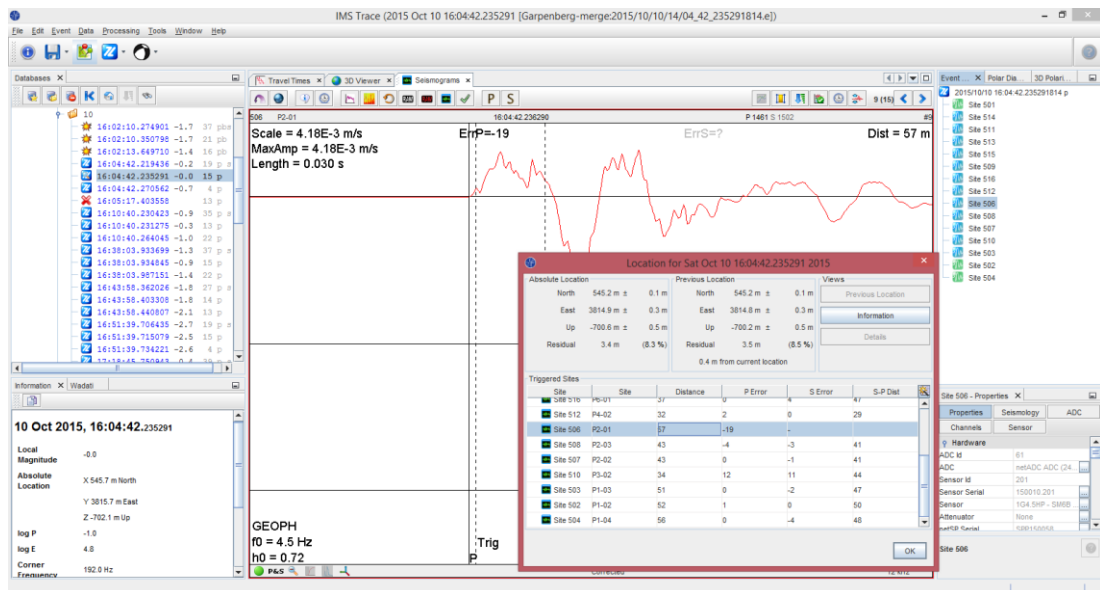


Figure 4.8 : The result after second location performed before S-wave arrival correction on sensor 508.

On Figure 4.9 the record from sensor 506 is shown. The P-wave residual for this sensor is -19, which means that the P wave arrival is too early than the calculated arrival



time. However, P arrival is not wrong. The analyst should not change the arrivals only to reduce the hypocenter error but should only ensure that his/her picking is correct, and keep the arrival as it is.



**Figure 4.9 :** The result after third location performed after S-wave arrival correction on sensor 508.

In case of large residuals for a particular sensor, the record can be excluded from calculations. It is possible that in some cases the traces for specific sensor have been wrongly associated with the event. Figure 4.10 shows the result after Sensor 506 was disabled (removed) in the calculation. This high error elimination had a significant effect on location residual. Total location residual changed from 3.4 m to 2.9 m (ADH changed from 8.3 to 7.2%).

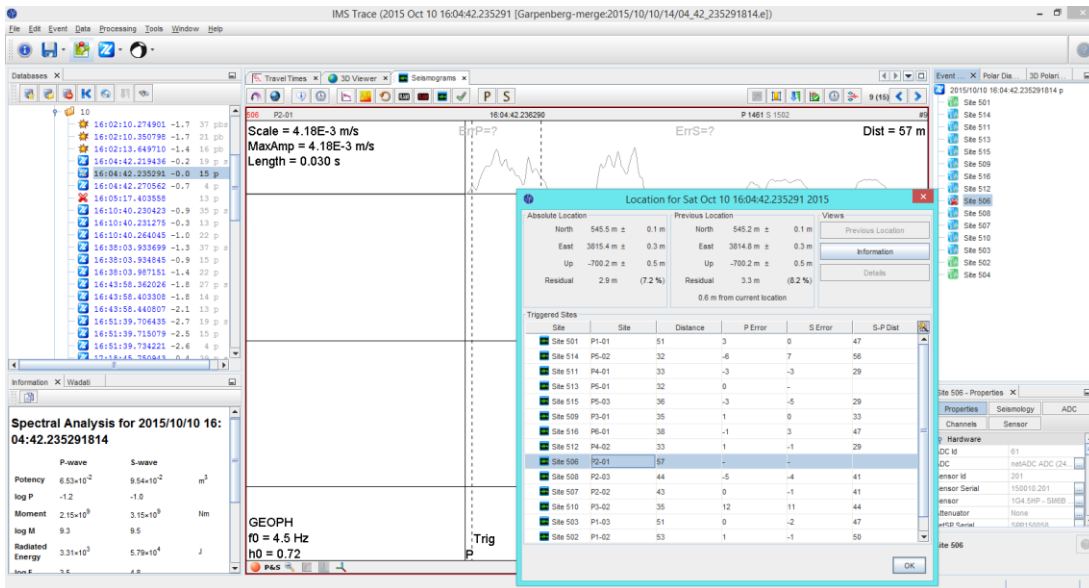


**Figure 4.10 :** The result after fourth performed location after correction of P (or S) arrival on sensor 506 was eliminated (disabled).

Next correction was applied on Sensor 510. According to the results the P- and S-residuals were 12 and 11, respectively (see Figure 4.10). The residuals suggest that the arrival times were later than the calculated ones. As seen in Figure 4.11 the P-arrival was clear but a small correction of 1 sample was made (picked a little earlier). The S-wave arrival was not very certain. Despite of the large residuals, this sensor was kept in the calculation.

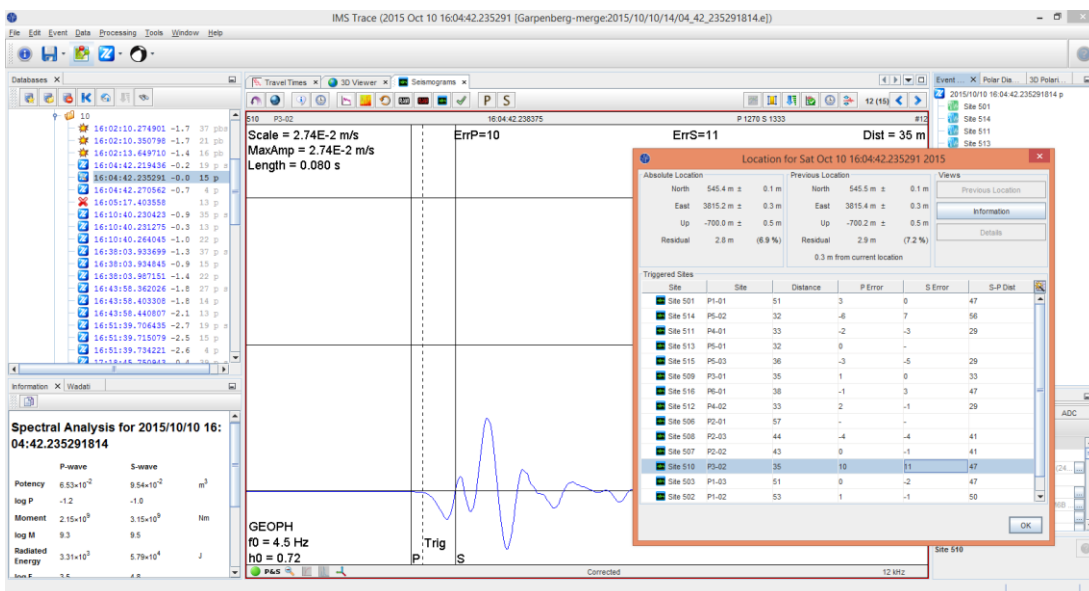


**Figure 4.11 :** The result after fifth performed location after correction of P (or S) arrival on sensor 510 correction.

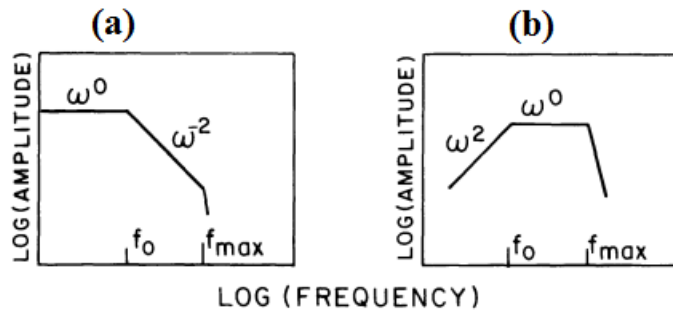
The process of picking the arrival times for all sensors in the local seismic system and calculation of the hypocenter location for 16:04 on 10 October 2015 was described. The total residual error was found to be 2.8 m (or 6.9% AHD). No further improvement in the location was possible.

In addition to phase picking sensor geometry, velocity model, location algorithm (Kijko and Sciocatti, 1995; Ge, 2005; Wang and Ge, 2008) are also other important factors that affect the quality and accuracy of the source location. Although, the arrival times are clearly visible and picked correctly, the hypocenter solution may have large residual. In other cases even the velocity model is correct and sensors geometry is good, the sensors may show systematic residuals for P- and/or S- wave. This might be a result of local site effects. When the result for the hypocenter location is as best accurate as possible, the source parameters can be calculated by Perform Source.

#### **4.4 Perform Source**

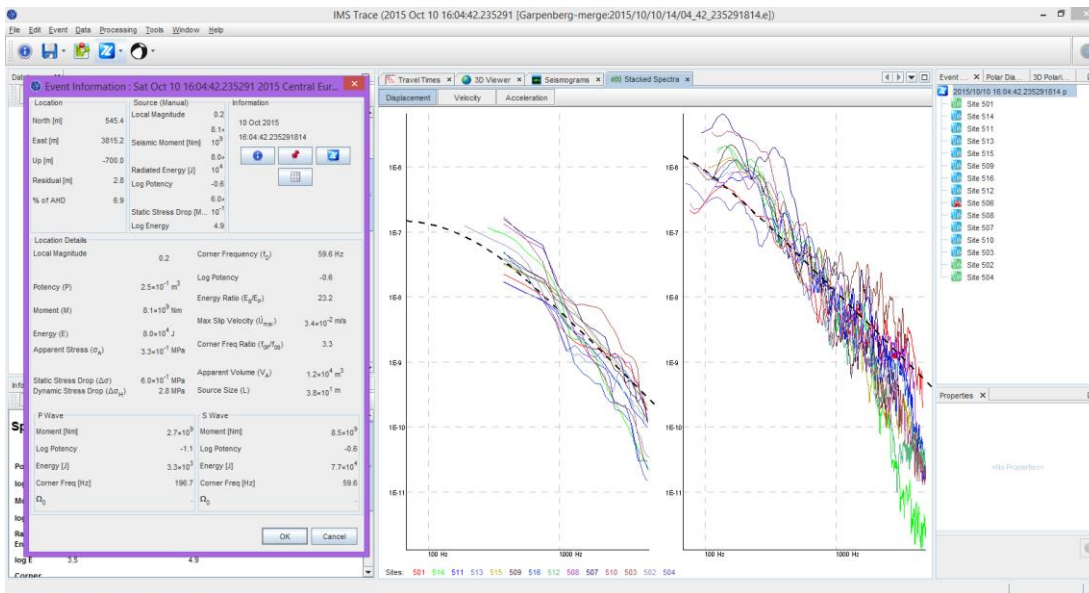
Dynamic source parameters calculation is the last step of data processing adopted for the mining induced-seismic events in this study. Parameters are calculated easily by IMS Trace. All dynamic source parameters were described in Chapter 3. IMS Trace uses Brune model (1970, 1971) for approximation of the spectra. The radius is calculated using the formulas in Brune et al. (1979). After performing the source parameters calculation a graph showing the stacked spectra, separately for P- and S-wave appears on the screen. At this stage the stacked spectra have to be checked for deviations of the individual spectra from the average spectrum and if the high-frequency slope corresponds to the default  $\omega^{-2}$  slope or it needs to be adjusted.

Figure 4.12 shows a Brune model spectrum for displacement and acceleration. Standard spectral slope is defined as  $\omega^{-2}$ . Recent studies have indicated that the high-frequency slope of displacement spectra could be between  $\omega^{-2}$  and  $\omega^{-3}$  (Young et al., 1989). IMS Trace software allows using only the end values for the power -2 or -3.



**Figure 4.12** : Brune model spectrum (a) displacement (b) acceleration spectrums (Young et al, 1989).

Source location calculation is quite easy with IMS Trace. When event location accuracy satisfies the analyst, Perform Location would be applied. An example of source parameters window with the stacked spectra for the event at 16:04 on October 10, 2015 is shown in Figure 4.13. As a default value the slope was defined initially as  $\omega^{-2}$  in IMS Trace. However, this model does not fit the spectra very well (Figure 4.13). The slope was changed to  $\omega^{-3}$  and the source parameters re-calculated. Figure 4.14 shows how source parameters have changed when the slope was defined as -3, a much better fit of the stacked spectra.



**Figure 4.13** : The source parameters of the event (on October 10 at 16:04) source parameter solution with slope  $\omega^{-2}$ .

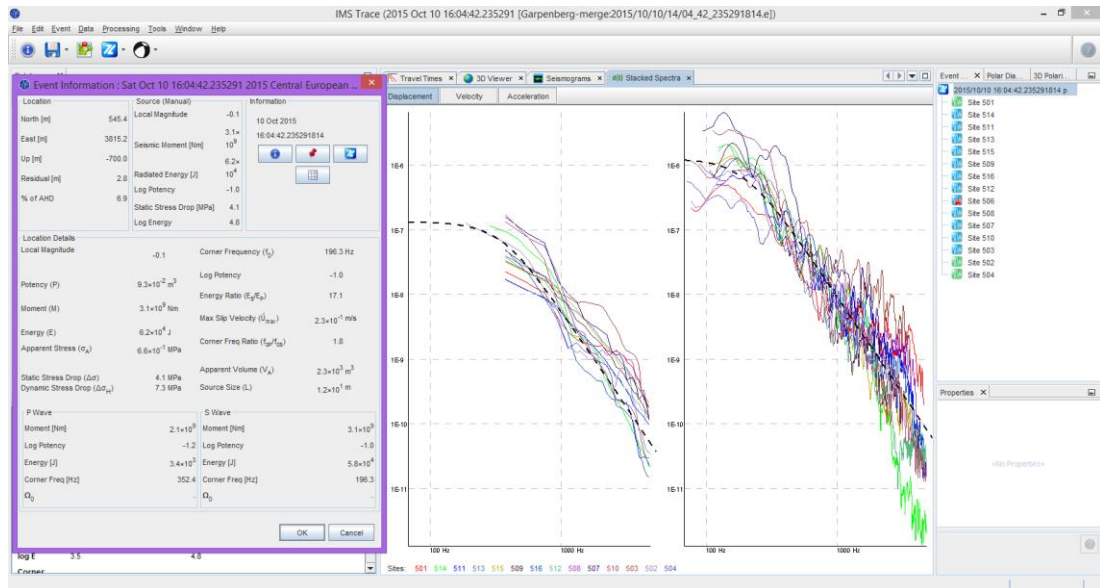


**Figure 4.14 :** The source parameters of the event (on October 10 at 16:04) source parameter solution with slope  $\omega^{-3}$ .

Figures 4.13 and 4.14 show how the high-frequency slope changes the solution of the source parameters changed as a result of it. Sometimes the change is very substantial. The optimal solution is determined by the model fit for the two cases of -2 and -3 slope. Source parameters are dependent on the model as mentioned in Chapter 3. For the event on October 10 at 16:04, slope  $\omega^{-3}$  is accepted because the model misfit was lower. The last step is the saving the result for the event. Trace does not have automatic save option. If data processing solution is within the acceptable limit, the event has to be saved as Accepted event. Otherwise, all processing will be erased. The procedures for processing of the events described in this chapter were followed for Zinkgruvan and Garpenberg mine event, described in Chapter 5 and 6.



## **5. ZINKGRUVAN MINE**

The first dataset of induced seismic events were taken from Zinkgruvan Mine (Sweden). The local geology data is not easy to collect because tunnels should be supported as soon as possible. Due to the missing the local geology data, the general geological structures were briefly explained to understand formation of the ore body and the host rock. The general information about the mine site are also given such as ore body, and production method. This study focused on relation between the production blast and rockmass responses.

### **5.1 Geology**

Zinkgruvan mine is located on Svecofennian Domain of Baltic Shield which is formed by supracrustal Precambrian rocks (Bengtsson, 2000), which felsic metavolcanic unit are dominant (Owen and Meyer, 2013). The basement was formed during either Archean or Proterozoic time (Bengtsson, 2000). Lots of small proximal basins have been formed because of continental rift environment (Owen and Meyer, 2013). This area was deformed during the Svecofennian orogenesis, because that primarily deformation could not be detectable (Bengtsson, 2000; Bjärnberg, 2009).

Zinkgruvan ore bodies were formed after three different phase of metamorphism. They are contact metamorphism, low pressure regional metamorphism and post-metamorphism (Bjärnberg, 2009). Lots of volcanic intrusion occurred in the area during the rifting stage.

Zinkgruvan mine has Zn-Pb-Ag ore deposits and it is not single ore body. Ore bodies have been cut into several pieces, that have been disturbed by faults and tectonic activities moreover the basement is also highly affected due to tectonic activity (Bengtsson, 2000).

Bengtsson (2000) described the lithological sequences in three groups and these units are shown in Figure 5.1. These units are a red, fine grained, massive to foliated quartzofeldspathic rock; the ore bearing, grey, fine grained, massive to foliated,

occasionally skarn banded quartzofeldspathic rock, and veined gneisses. Zinkgruvan mine site were set up the Svecofennian metasupracrustal rocks.

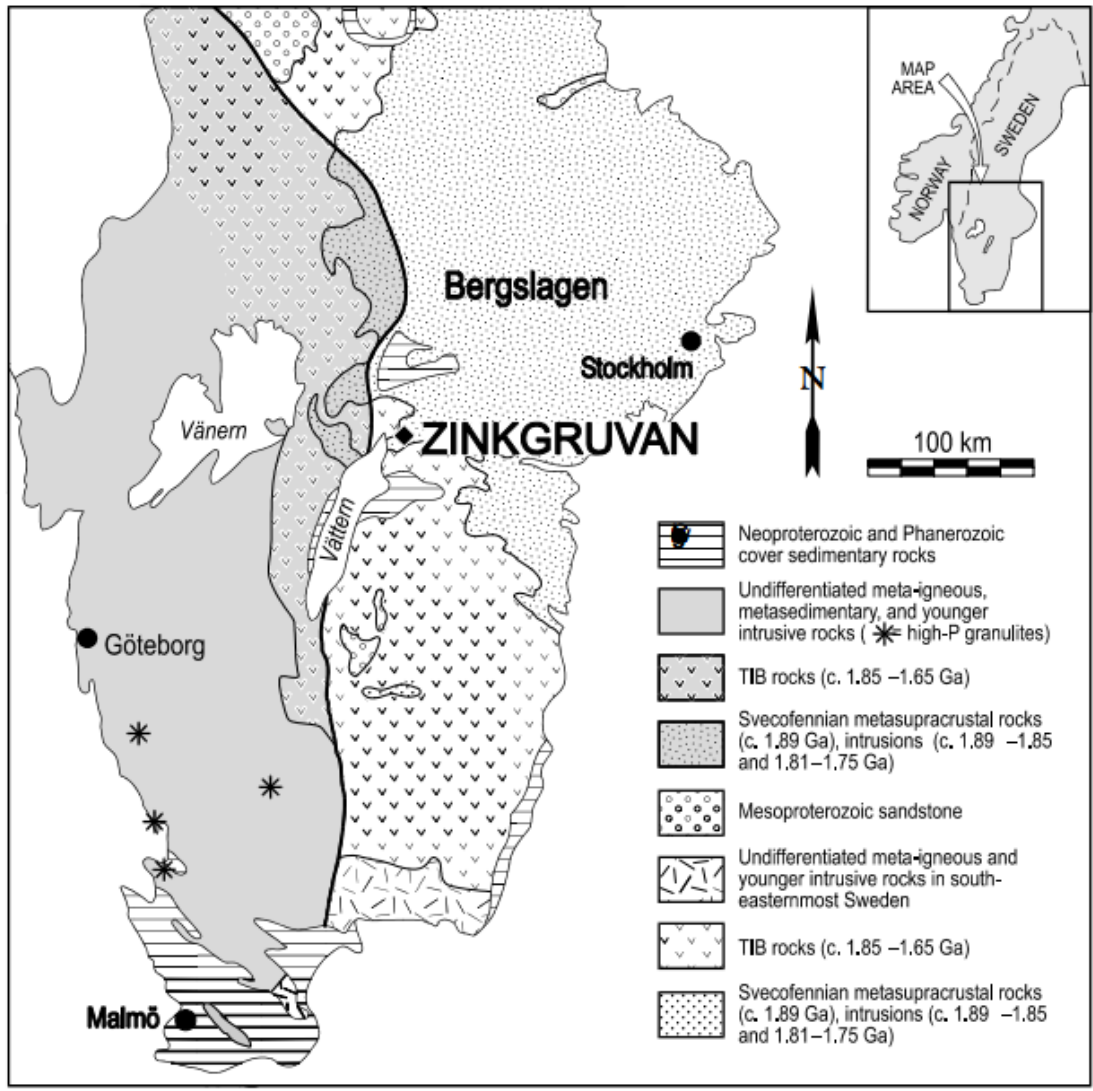


**Figure 5.1 :** Geology of southern Sweden (Bengtsson, 2000).

The fault which cuts the ore bodies is Knalla fault. The outcrop of the area is mainly covered by quartz microcline rocks. The units between quartz microcline and argillic metasediments unit are complex (Bjärnaborg, 2009). Figure 5.2 shows the local geological units of Zinkgruvan Mine site. The area is also characterized by metamorphic structure and these structure has been folded and faulted.



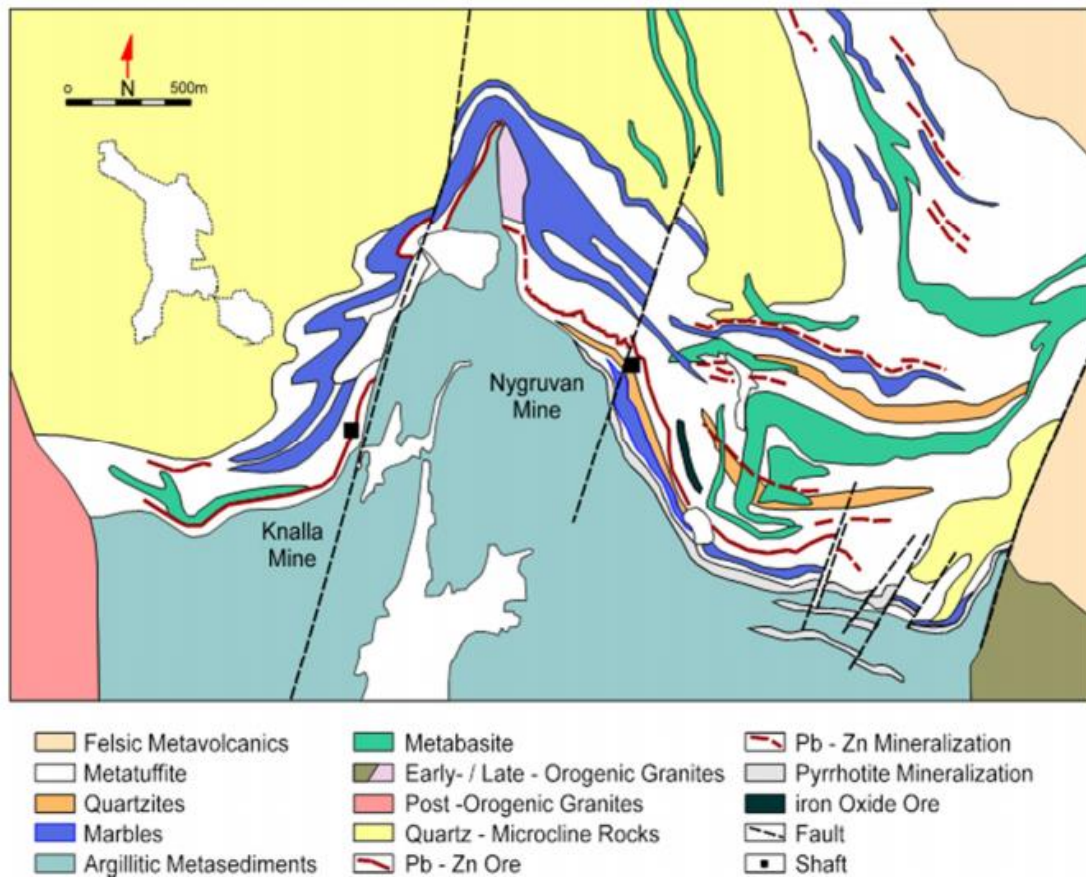


**Figure 5.2 :** Generalized geology map of Zinkgruvan mine site (Owen and Meyer, 2013).

## 5.2 Mine Operation

Zinkgruvan ore body was found for the first time in 16<sup>th</sup> century but the production has been ongoing since 1857 (Björnaborg, 2009). The mine is located northwest of the village of Zinkgruvan. The first produced mineral was copper. The zinc mineral was found at Zinkgruvan area during the middle of 20<sup>th</sup> century. Today zinc-lead-silver are produced and mine is deeper than 1100 m below the surface (Owen and Meyer, 2013).

Nygruvan ore body was removed firstly. Today operations are focused on the ore body at Knalla. Deep ore bodies have been found at both mine sites, so mine operation will be redesigned (Owen and Meyer, 2013). Figure 5.3 shows the active production areas in Zinkgruvan mine. The local network were installed where to be indicated as “1” (Ny 1125).

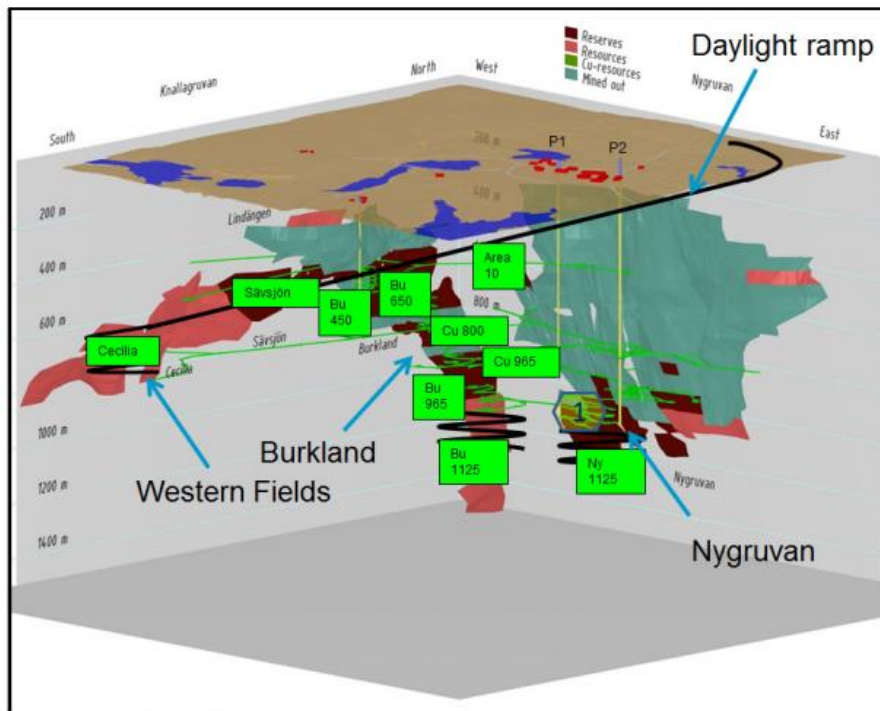


**Figure 5.3 :** Mine operation sites (Owen and Meyer, 2013).

The mining methods used are underhand and overhand mining sublevel stopping. The underhand is used below 1130 meter for Burkland and Nygruvan. Above that level a different version of overhand mining sublevel stopping is used.

The ore excavated from top to bottom. The production levels are planned before extraction. There are gaps between stope levels which are not mined. After finishing extraction in the stope, the opening is back filled and mining operations start below the level which is backfilled.

The stope height is between 30 and 50 meters and the width of the stope is between 20 and 25 meters. The production sequences are showed in Figure 5.4. The excavation method used in Zinkgruvan mine stopes is drilling and blasting. The diameter of production blast holes is changing between 89 and 100 mm.

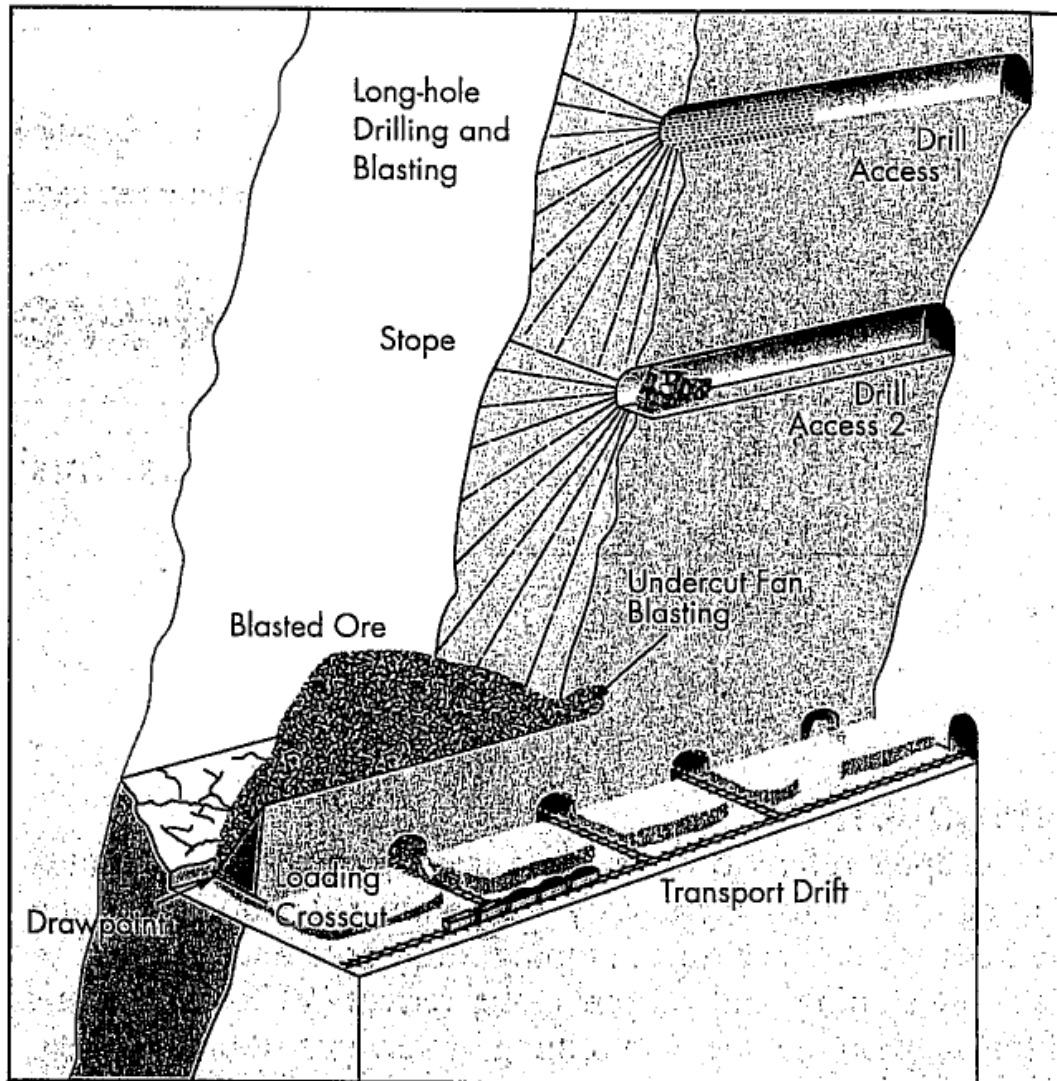


**Figure 5.4 :** Mining methods at Zinkgruvan mine (Pakalnis and Hughes, 2011).

### **5.3 Seismic Events Data Processing**

#### **5.3.1. Seismic systems and data**

Zinkgruvan mine is seismically active and the seismic activity in the mine has been monitored since November 1996 (Björnberg, 2009). Additionally to the permanent seismic monitoring system, a local network consisting of 18 sensors was installed in May-August 2015 at ~1100 depth, in area around 40×50m<sup>2</sup> (Figure 5.5). The installed sensors are 4.5 Hz geophones – uniaxial and three-axial and sample rate of the sensors were 12 kHz. The sensors are synchronized by local time. Some of the sensors in the network are installed on the surface of the excavated drift (walls or roof) and some are installed in drill holes at distance around 9 m from the drift (vertically or horizontally).

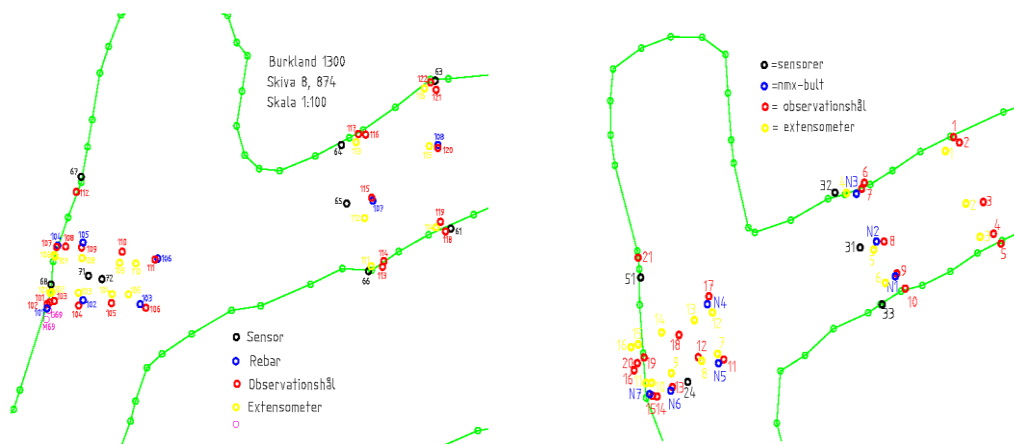


**Figure 5.5 :** Local network installation at site 871 and 874. The black circles show the sensor, the red dots are observation wells and the yellow dots are extensometer.

The blast and the rockburst was in near proximity to the local network and rockburst occurred at Zinkgruvan mine on July 2, 2015 at 15:00 (local time), caused by a production blast. Another blast was produced near the local seismic system on July 1, 2015 at 15:00. Large number of seismic events were recorded after the production blasts. More than 3000 events were recorded altogether by the local network between July 1 and 2, 2015 and processed automatically by the IMS Trace software.

The accuracy of the automatic arrival times did not allow precise calculation of the kinematic and dynamic source parameters. That is why manual processing had to be done. As manual processing of so many events was not possible, microseismic events were filtered by following two criteria. First, events, which were recorded by less than 15 sensors, were eliminated because if the event magnitude was too low less sensors would record it. Second, only the seismic events recorded 3 hours before the blasting and until midnight on the same day were processed. After applying these two criteria approximately 271 events were left and these events were manually processed.

### 5.3.1 Number of seismic events with time

Figure 5.6 shows the number of all events recorded per half an hour by the local system. Approximately 30 events were recorded every half an hour before each blast on July 1 and July 2. The number of events increased dramatically immediately after the blasting to ~200 events and then the seismic event number dropped off approximately 1.5 hours later on both days. The complete relaxation could not be

followed on July 2. First, two higher magnitude seismic events occurred after the main shock on this day (see Figure 5.6). Second, the connection between the seismic system and the server was cut during the rockburst and the data in the local system were saved only until ~18:00 on July 2. The secondary increase in the number of events on July 2 is most probably related to the larger seismic events with Mw 0.2 and 0.4. The largest event on July 1 was with Mw 0.6 and on July 2 with Mw 1.2.

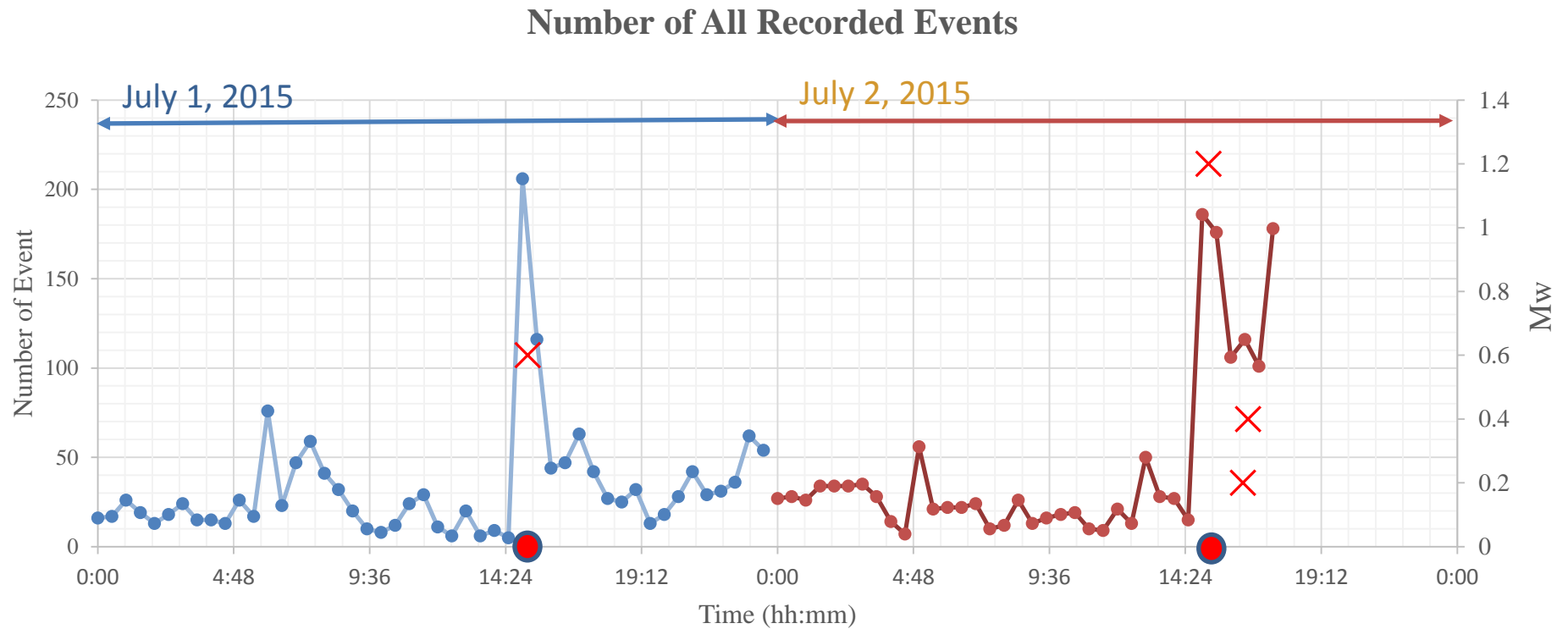


**Figure 5.6 :** Number of recorded seismic events. Blasts are marked as red circles. Red crosses show the highest moment magnitude events (the magnitude scale is shown on the right side of the graph).

### 5.3.2 Data processing

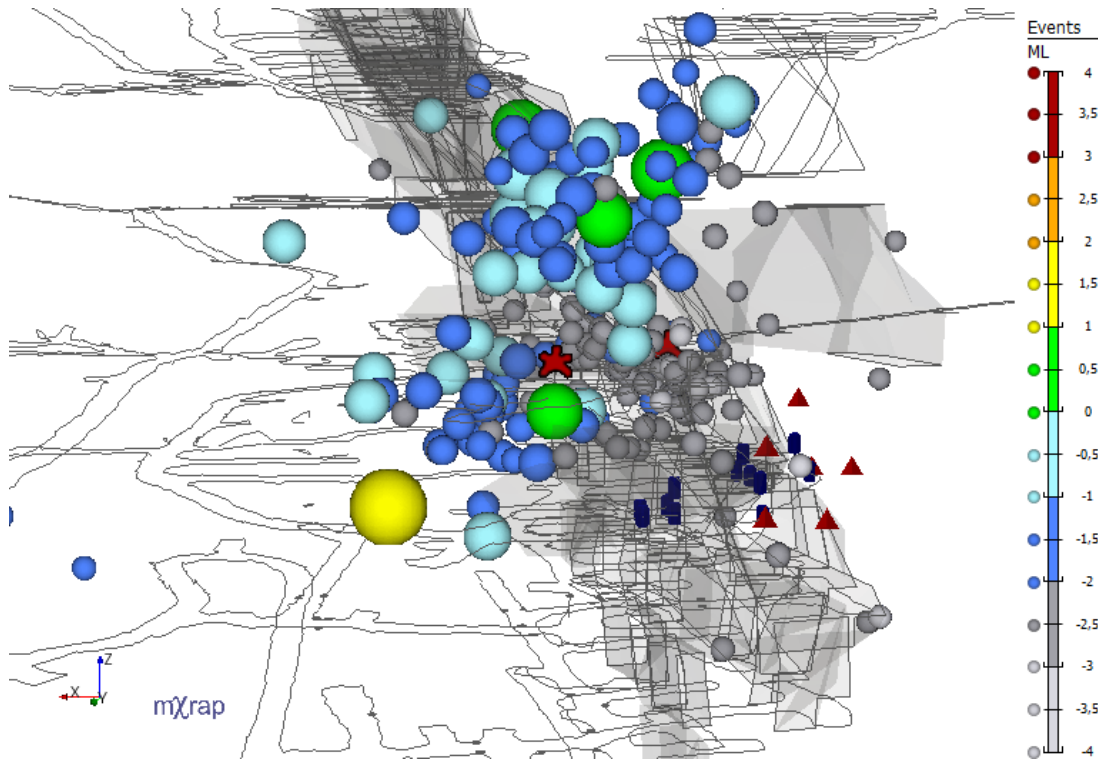
The arrival times on all recorded waveforms (4517 waveforms from 271 events) were picked manually and hypocenter locations were calculated using IMS Trace software. The arrival times were verified and re-adjusted until average hypocentral distance (AHD) was less than 5%. Only few events were located with AHD higher than 5% and the average AHD was 4.47%. This result indicates that phase picking and source locations were reliable. The high frequency slope of the displacement spectrum was tested as  $\omega^{-2}$  and  $\omega^{-3}$  in order to get more precise source parameters. The initial default slope of  $\omega^{-2}$  was changed to  $\omega^{-3}$  for almost half of the processed events because the misfit between theoretical and stacked event displacement spectra was smaller for these cases.

For Zinkgruvan case study only data from the local seismic system was used. Data from the permanent seismic system was not used as the sensors in this system are far from the area of the studied seismic events, which were comparatively small.

### 5.3.3 Hypocenter locations

Event location visualization was done by mXrap program. mXrap is very powerful and user friendly program, developed by the Australian Center for Geomechanics (<http://www.acg.uwa.edu.au/home>). Seismic event locations could be visualized in 3D and source parameters could be added as symbol properties. Figure 5.7 shows all hypocenter locations of the manually processed seismic events. Seismic event is represented as circles with size and color depending on the local magnitude. As seen on Figure 5.7, the highest magnitude ( $M_w=1.2$  on July 2) event was found at the lower edge of the formed cluster of all seismic events.

The sensor locations are concentrated within  $40 \times 50 \text{ m}^2$  area at around  $\sim 1100 \text{ m}$ . The red triangles show triaxial sensors and the blue cylinders - uniaxial sensors. The blast events are shown as red stars, in the middle of the cluster.



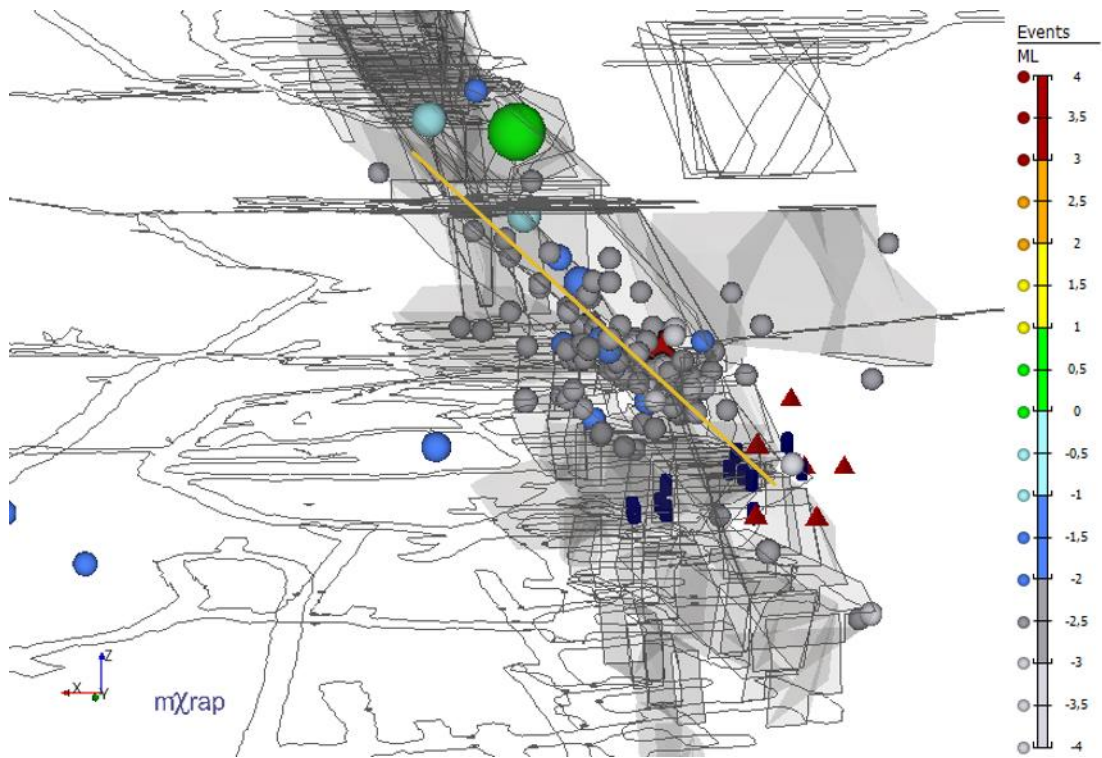
**Figure 5.7 :** All manually obtained events locations (vertical plane). Size of the circle and the color correspond to the magnitude. The sensor locations are shown as blue cylinders (uniaxial sensors) or red triangles (triaxial sensors).

Figure 5.8 shows the events only on July 1. The approximate location of the blast on this date is shown as red star in the middle of the cluster. The largest (main) seismic event which was recorded at 15:10 on July 1 ( $M_w=0.6$ ) is located at the upper edge of the cluster. It occurred approximately 15 minutes after the blast.

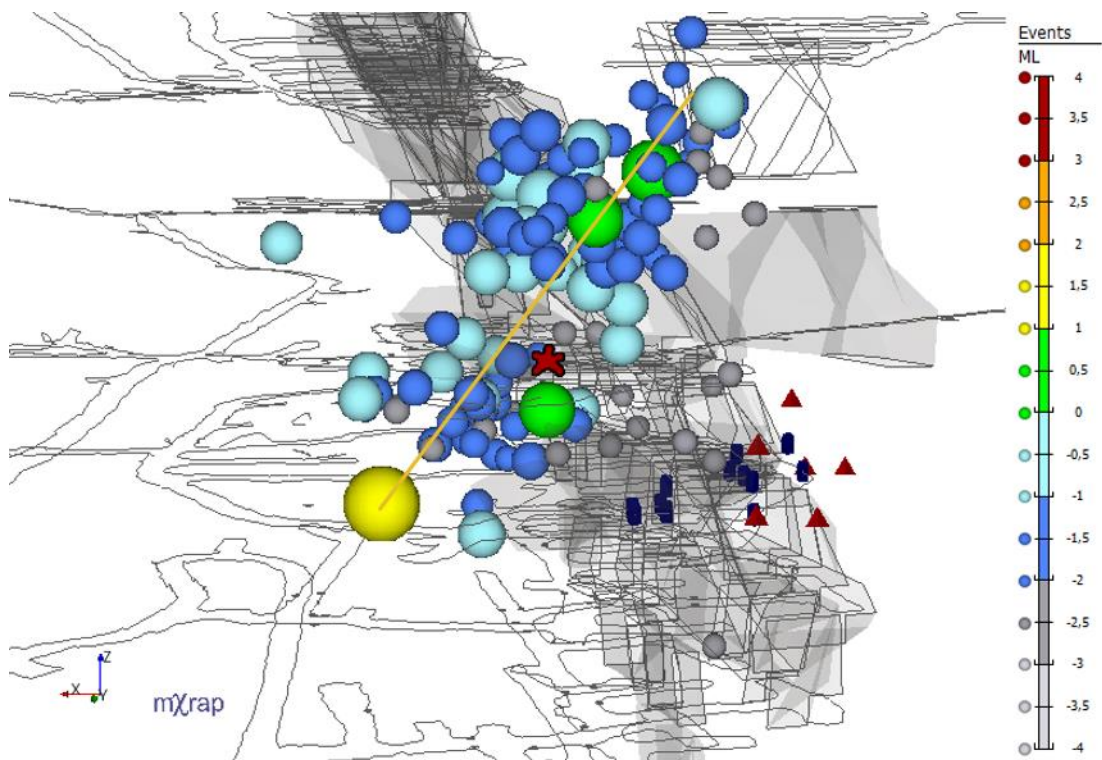
The seismic events on July 1 formed a cluster with dimensions  $\sim 50\text{m} \times 30\text{m} \times 60\text{m}$ . Only a few events were located outside of the cluster. The cluster follows the slope of the ore (shown in grey). The orientation of the cluster is defined as orange line. The distance between the blast and the largest event is 90 m.

Figure 5.9 shows the seismic event locations on July 2, 2015. These events also formed a cluster, with orientation almost perpendicular to the orientation of the cluster on July 1. In this case, the largest magnitude event ( $M_w=1.2$ ) was located at the lower edge of the cluster. The distance between the largest seismic event, which occurred during the blast and the average location of the blast on July 2 was  $\sim 35$  m. The formed cluster had dimensions  $50\text{m} \times 60\text{m} \times 80\text{m}$ .





**Figure 5.8 :** Seismic event locations on July 1, 2015.



**Figure 5.9 :** Seismic event locations on July 2, 2015.

### 5.3.4 Magnitude, seismic moment, and energy distributions

The seismic event on July 1 and July 2 had very different source parameter. The events on July 2 in general were found to be larger than the events on July 1. The results for the magnitude, seismic moment and energy distribution will be described here.

Moment magnitude distributions for July 1 and July 2 are given in Figure 5.10 and Figure 5.11, respectively. The moment magnitudes on July 1 in overall were lower than on July 2. 60% of all processed seismic events of July 1 had moment magnitude below -2.5. Less than 5% of seismic events had moment magnitude higher than 0 (only 1 event). The largest number of seismic events was with magnitudes between -3.3 and -2.5.

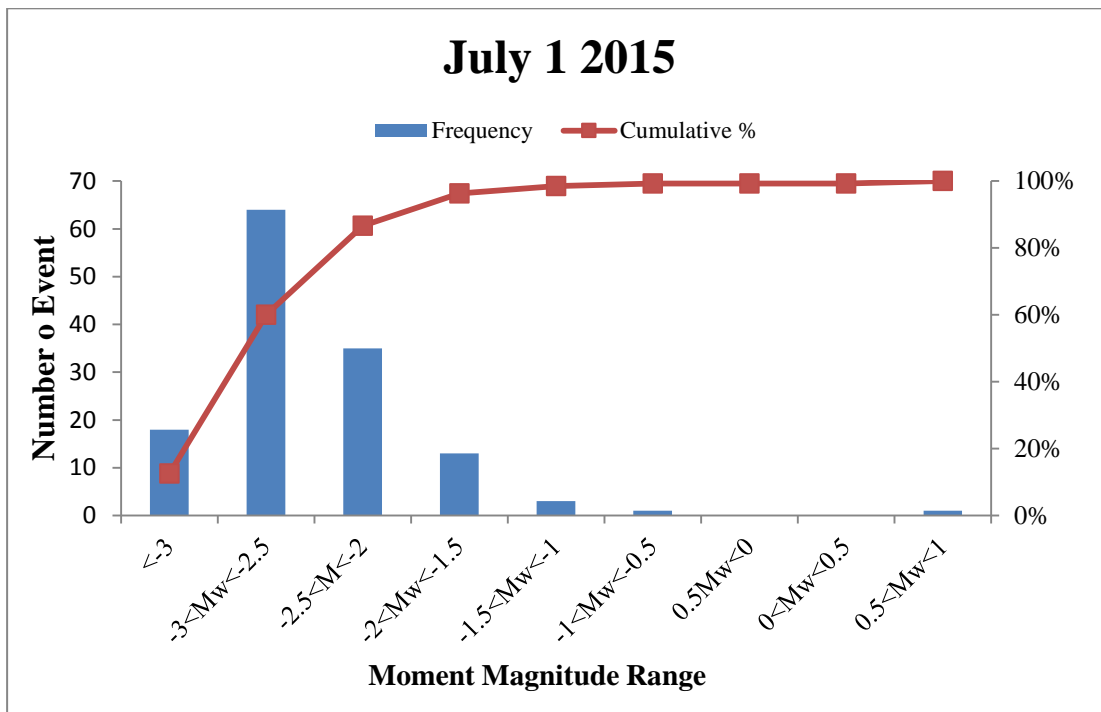


**Figure 5.10 :** Moment Magnitude distribution on July 1, 2015.

The moment magnitude distribution for July 2 (Figure 5.11) shows that firstly, 60% of the event moment magnitudes were below -1.5. Secondly, there were three events with moment magnitudes above 0. The maximum number of events was with magnitudes between -2 and -1.5.

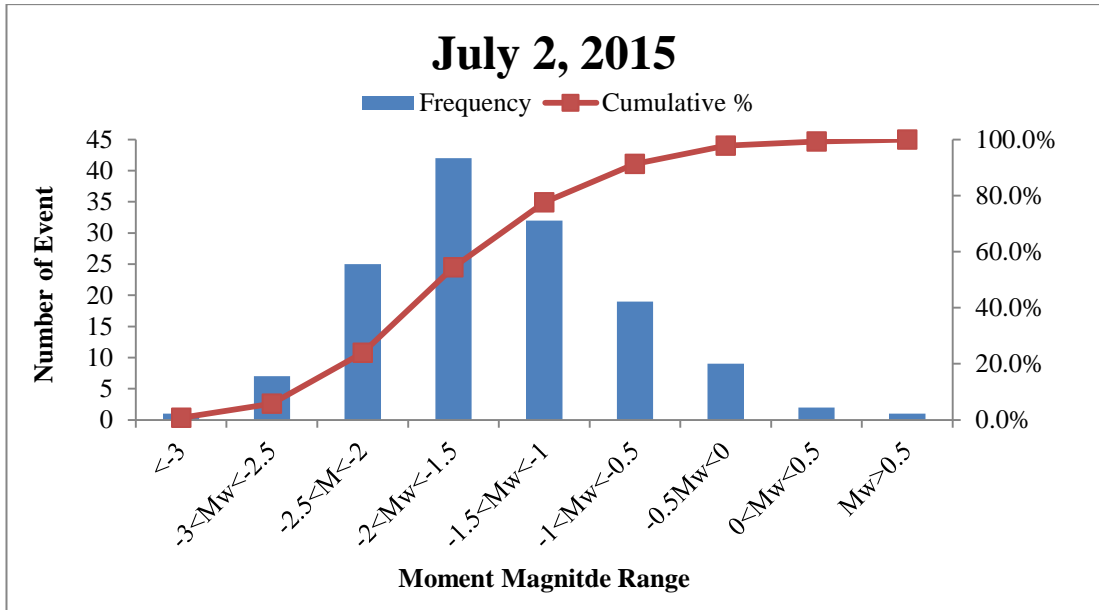


**Figure 5.11** : Moment Magnitude distribution on July 2, 2015.

The relationship between the energy and moment magnitude given in Figure 5.12 shows that in overall the July 1 seismic energy values were lower than July 2 energies. Moreover, the energy released by the events on July 1 with the same moment magnitude was lower than by the events that occurred on July 2. Data for the events on July 1 do not show very good correlation between the energy and the moment magnitude (correlation coefficient 0.49) while there is good relationship between the energy and moment magnitude for July 2 seismic events (correlation coefficient 0.81).

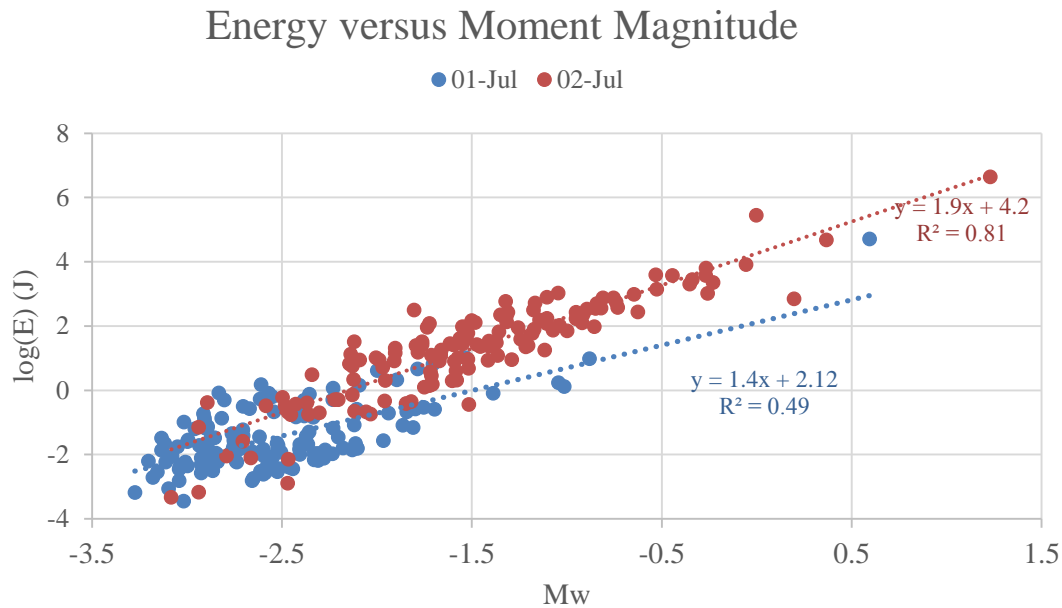


**Figure 5.12 :** Logarithm of energy versus moment magnitude for both days – July 1 (blue) and July 2 (red), 2015.

Figure 5.13 shows seismic events of July 1 (top) and July 2 (bottom). The size of the circle represents the local magnitude of the event. Any relations could not be found between energy and magnitude or spatial distribution of seismic events.

Seismic events with lower energy on July 1 generally occurred at the upper half of the cluster. Seismic events around the production blast of July 1 had relatively higher energy (Fig. 5.13a). The seismic energy distribution on July 2 was more complicated. Only a few seismic events occurred around the blast location on this day but they had comparatively large energy even their moment magnitude was lower (Fig. 5.13b). If we combine the two figure 5.13 (a and b) the gap on July 2 was actually the area of most intense seismic activity on July 1. Possibly most of the accumulated energy was released after the blast on July 1 and this was the reason for the gap.

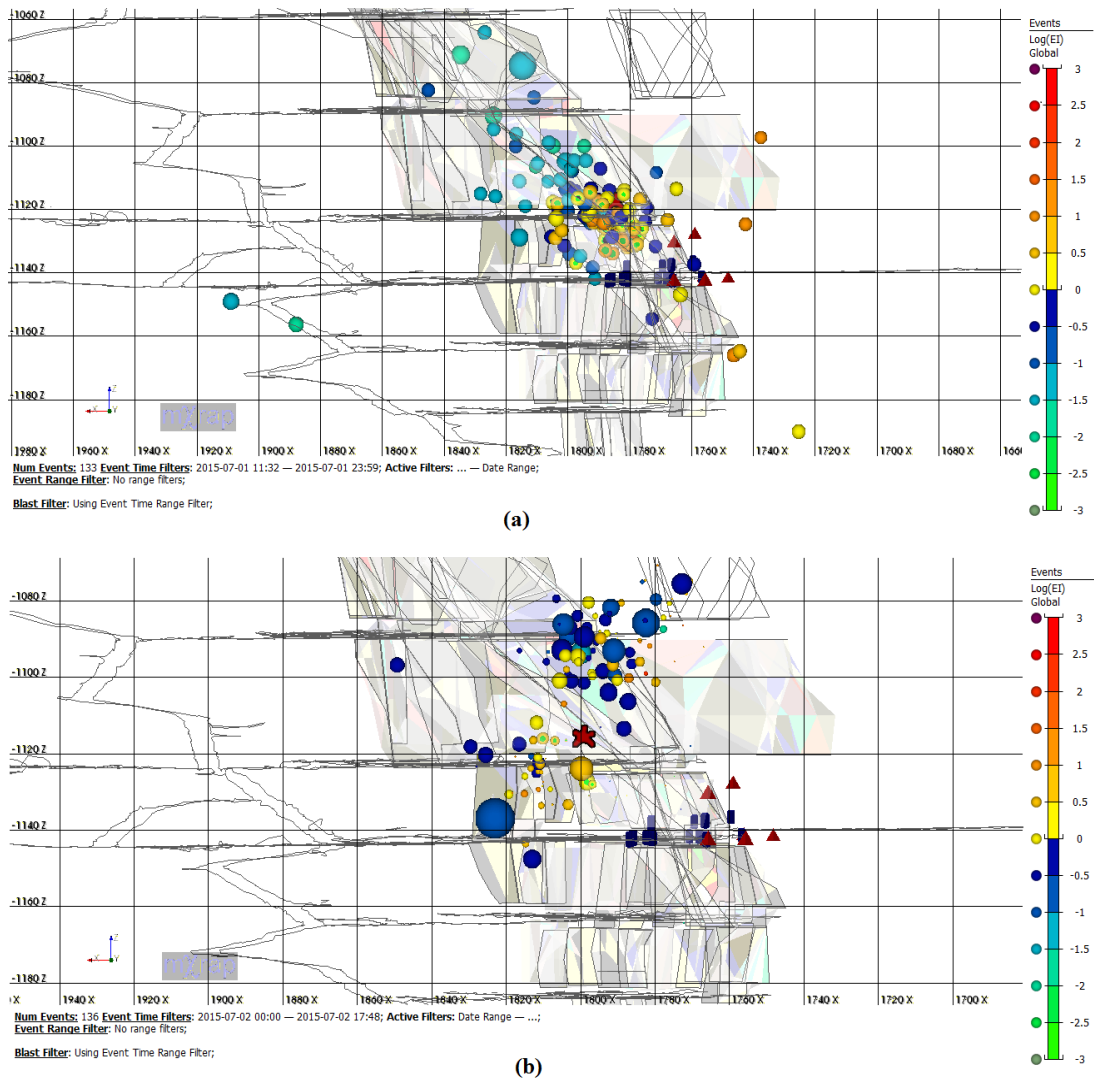
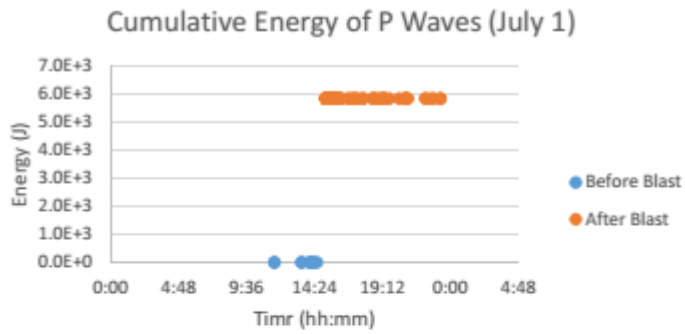


**Figure 5.13 :** Seismic energy of seismic events on (a) July 1 and (b) July 2. The color and the size of the circles show the energy and local magnitude, respectively.

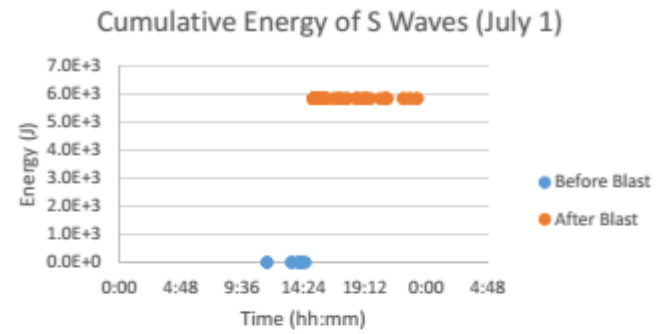
More total energy was released on July 2 compared to July 1. Figure 5.14 shows the cumulative energy of P and S waves for each day. The cumulative energy release patterns for both days are different but the P and S waves energy graphs are almost same for individual days. Blue dots indicate the seismic energy before the blasts and orange dots - after the blasts.

On July 1 the seismic event at 15:10 with  $M_w=0.6$  released the highest amount of energy ( $1.7 \times 10^6$  J) on this date. On July 2 the highest magnitude event  $M_w$  1.2 recorded during the blasting, had energy  $4.4 \times 10^6$  J. Other two high magnitude events  $M_w = 0.2$  and  $M_w=0.4$  released energy of  $6.9 \times 10^2$  J and  $4.8 \times 10^4$  J, respectively. However, the largest energy ( $1.5 \times 10^5$  J) was released during the event with a moment

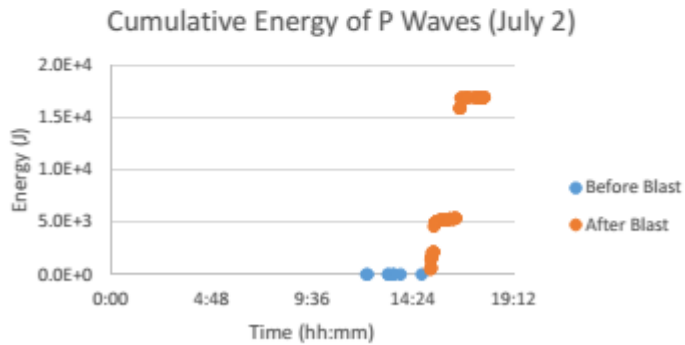
magnitude of -0.1 recorded approximately half an hour after the blast. One significant energy step is seen on July 1 and two steps on July 2. All of them are related to the largest seismic events.



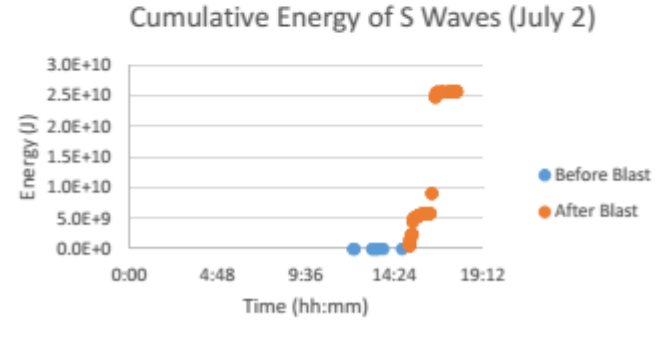
(a)



(b)



(c)



(d)

**Figure 5.14** : Cumulative energy radiation for P and S wave on July 1 and July 2, 2015 (Blue dots are for the events before the blast and orange dots are for the events after the blast).

Table 5.1 shows a summary of the type of the events based on the  $E_s/E_p$  ratio results of manually processed events. 63% of all events resulted as shear events ( $E_s/E_p > 10$ ). The rest of the events that occurred were non-shear ( $E_s/E_p < 10$ ). Some difference in the percentage of the shear and non-shear events was observed on July 1 and 2. The events on July 1 were 68% shear, but on July 2 60% of the events were shear (Table 5.1).

Summary of the  $E_s/E_p$  based type of the largest magnitude events is shown in Table 5.2. Four events had magnitude larger than 0. Half of them were shear events. The seismic event at July 2 on 15:13 with the highest magnitude that caused the rockburst was a non-shear event. A relation between moment magnitude and  $E_s/E_p$  ratio was not found.

**Table 5.1 :** Percentage of types of recorded seismic events on July 1 and July 2, 2015.

	July 1, 2015		July 2, 2015	
	Number of Event	Percentage	Number of Event	Percentage
<b>Shear</b>	92	68	81	60
<b>Non-shear</b>	44	32	55	40
<b>Total</b>	135	100	136	100

**Table 5.2 :** The highest moment magnitude event information.

The highest Mw				
Date	Time	Mw	Type	$E_s/E_p$
01/07/2015	15:10:54	0.6	Shear	13.9
02/07/2015	15:13:51	1.2	Non-Shear	9.1
02/07/2015	16:26:14	0.2	Shear	12.5
02/07/2015	16:37:37	0.4	Non-Shear	6.0

$E_s/E_p$  ratio distributions for each day are given in Figure 5.15. According to this figure shear and non-shear events on July 1 are mixed spatially, e.g. it is not possible to define



a specific areas with shear and non-shear events. Most of the non-shear events of July 2 are located at the upper part of the main cluster. The relatively lower magnitude seismic events on July 2 were mostly shear events.

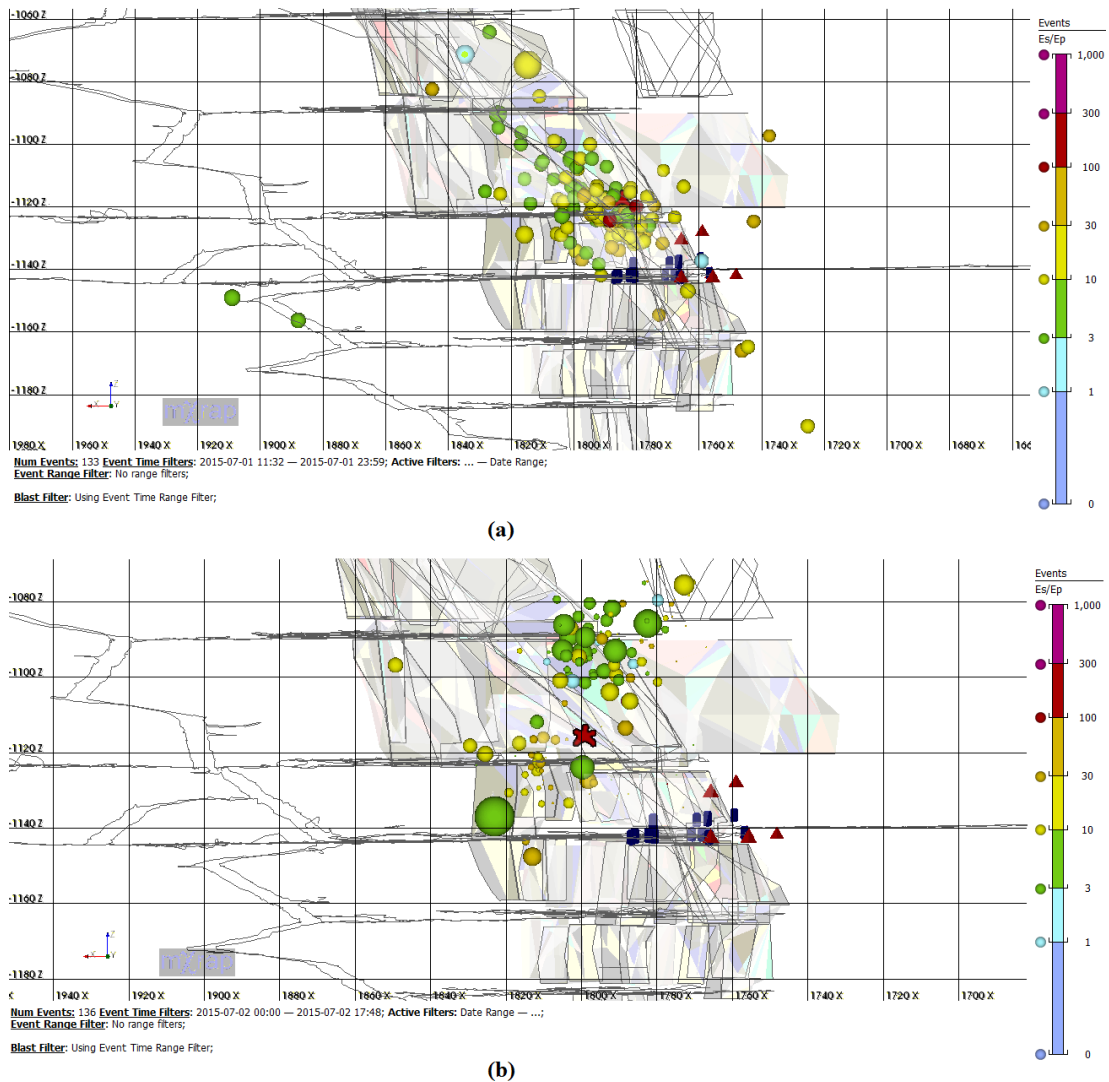
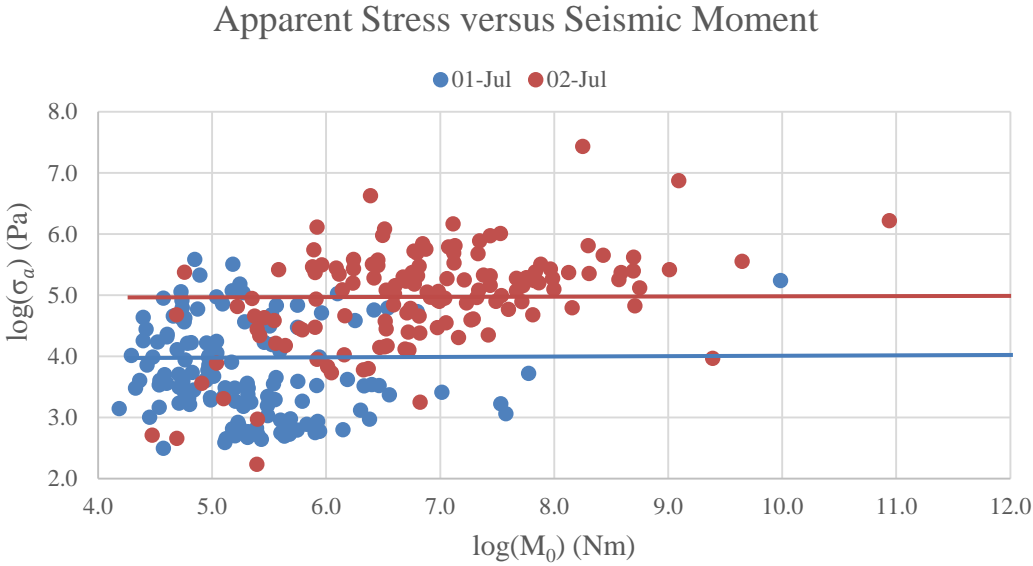


**Figure 5.15 :** Es/Ep of seismic events on (a) July 1 and (b) July 2. The color and the size of the circles show the Es/Ep ratio and local magnitude, respectively.

### 5.3.5 Apparent stress and stress drop

Apparent stress versus moment magnitude graph is given in Figure 5.16. No very good correlation could be found between them but in general the apparent stress increases with the seismic moment. In overall, the apparent stress on July 1 was lower than on July 2 even for the same moment magnitude events. The correlation between the apparent stress and the seismic moment was 0.003 and 0.2 on July 1 and July 2, respectively. The apparent stress of the events on both days varied in a wide range,

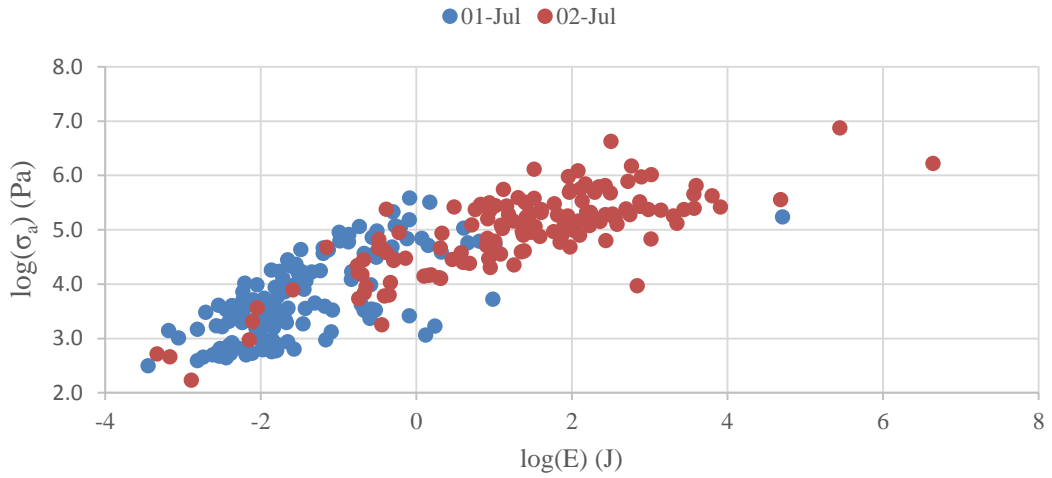
with approximately 1000 times difference between the largest and smallest apparent stress for each day. In total the ratio between the largest to smallest apparent stress on both days was approximately 100 000 times (Figure 5.16).



**Figure 5.16 :** Logarithm of apparent stress versus logarithm of seismic moment on July 1 (blue dots) and July 2 (red dots).

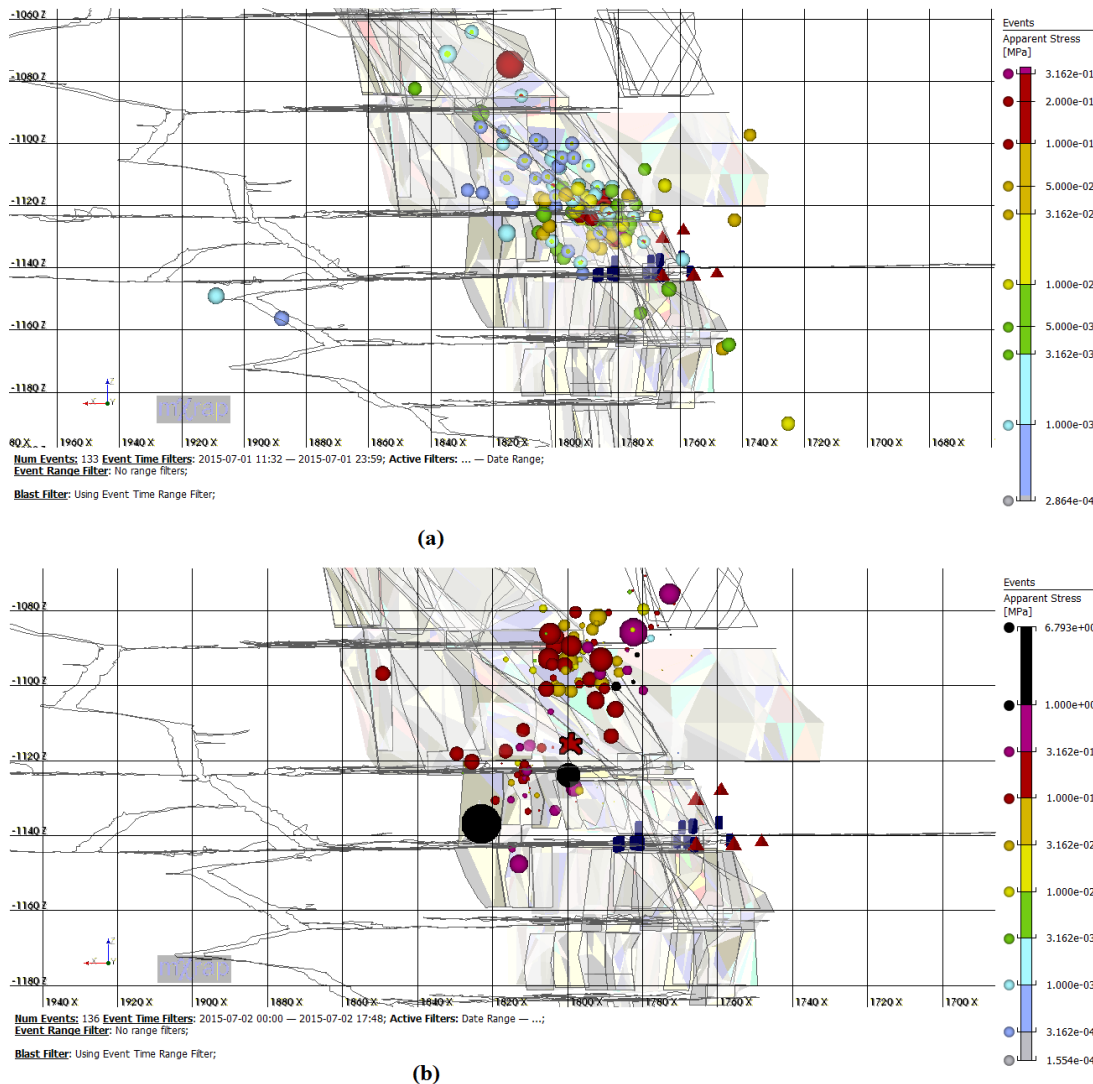
Figure 5.17 shows the logarithm of apparent seismic and the logarithm of seismic energy. According to the graph, apparent stress increased with seismic energy. The apparent stress and seismic energy values of the seismic events on July 1 were always lower than events on July 2. Limited number of seismic events on July 2’s apparent stress and energy were lower  $10^5$  Pa and less than 1 J, respectively. Moreover, more than half of the seismic events on July 1 were found within that range.

## Apparent Stress versus Seismic Energy



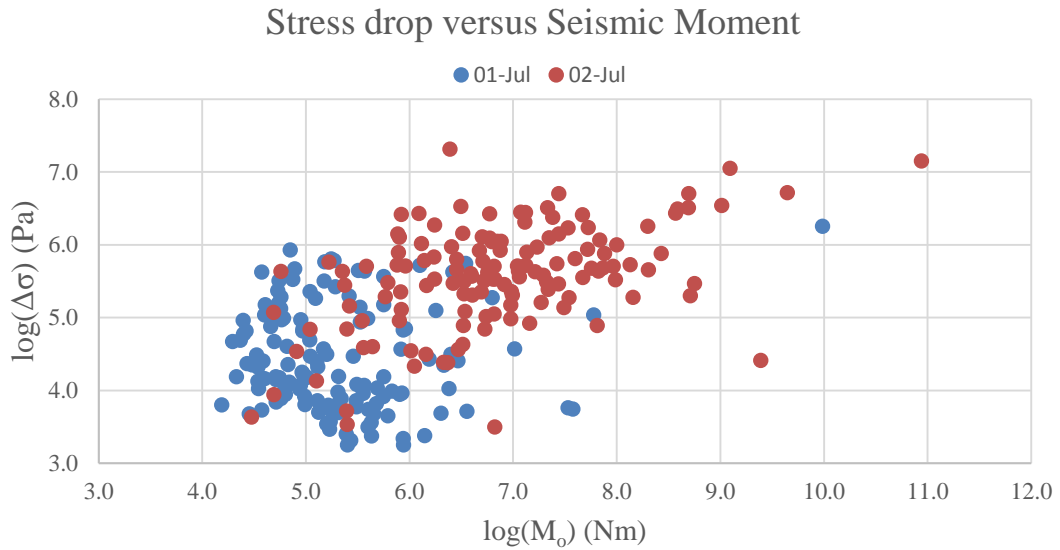
**Figure 5.17 :** Logarithm of apparent stress and logarithm of seismic energy on July 1 (blue dots) and July 2 (red dots).

Figure 5.18 shows the apparent stress of the seismic events on both days. The highest apparent stress seismic events on July 1 were found at two different locations: the highest moment magnitude event was at the upper edge of the cluster and other larger events were close to the blast. The apparent stress of July 2 seismic events were comparatively higher than of July 1 events. Very few events had apparent stresses lower than 0.03 MPa.



**Figure 5.18 :** Apparent stress of seismic events on (a) July 1 and (b) July 2. The color and the size of the circles show apparent stress and local magnitude, respectively.

The logarithm of the stress drop and the seismic moment graph is shown in Figure 5.19. As similar in Figure 5.16, the relation between seismic moment and stress drop was weak. However, a trend was also seen as stress drop increased with seismic moment. Seismic event on July 1 seismic event seismic moments change between 4 and 10 Nm in logarithmic scale though the stress drop change between 3 and 6.5 Pa (in logarithmic scale). The seismic moment change on July 2 seismic event is between 4.5 and 11 Nm and change of stress drop (in logarithmic scale) of same events are between 3.5 and 7.31 Pa. The event with 7.1 Pa stress drop and 9.1 seismic moment is the production blast of July 2. On the other hand, the production blast source parameters on July 1 is not higher than July 2.



**Figure 5.19 :** Stress drop versus logarithm of seismic moment on July 1 (blue dots) and July 2 (red dots).

The stress drop change with respect to energy is given in Figure 5.20. Stress drop refers to the stress difference on the fault (fracture) before and after a seismic event. Seismic events on July 1 had in general lower values for both stress drop and energy. The range of stress drop is between 3.0 and 7.25 Pascal (in logarithmic scale) for given days. The seismic energy and stress drop increase linearly. The highest stress drop was found at seismic event with moment magnitude 0.6 and -1.8 on July 1 and July 2, respectively. A trend was found between stress drop and seismic energy. Although, source parameter of seismic event on July 1 were lower, stress drop increased with seismic energy.

### Stress drop versus Seismic Energy

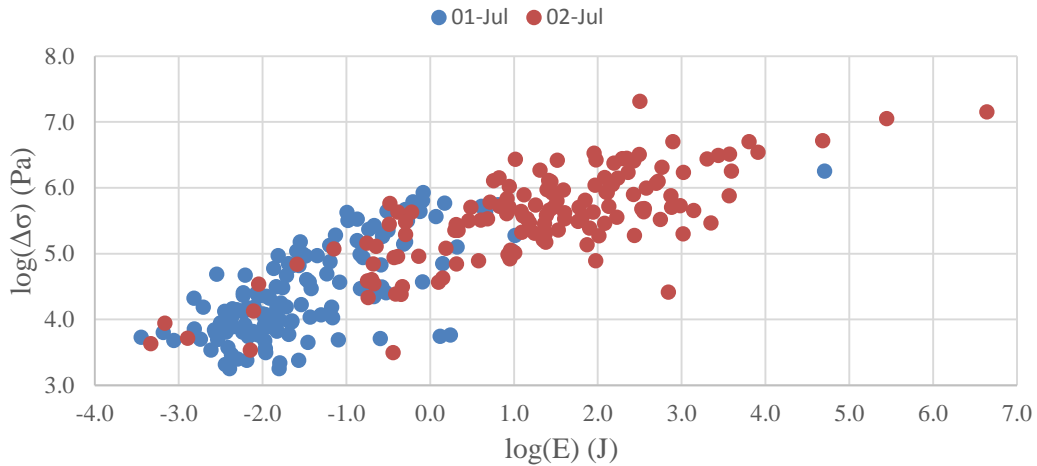


**Figure 5.20 :** Logarithm of stress drop versus logarithm of seismic energy on July 1 (blue dots) and July 2 (red dots).

Figure 5.21 shows the logarithm of apparent stress to the logarithm of stress drop. The stress drop and apparent stress on July 1 seismic events are lower July 2 seismic events. The theoretical line show the relation with stress drop and apparent stress ( $\Delta\sigma/\sigma_a = 4.3$ ) (Baltay et al, 2011). However, the induced seismic events were placed at lower level of the theoretical line. The ratio of Zinkgruvan Mine’s seismic events were 3.3 and 3.0 on July 1 and July 2 seismic events, respectively.

### Stress Drop versus Apparent Stress

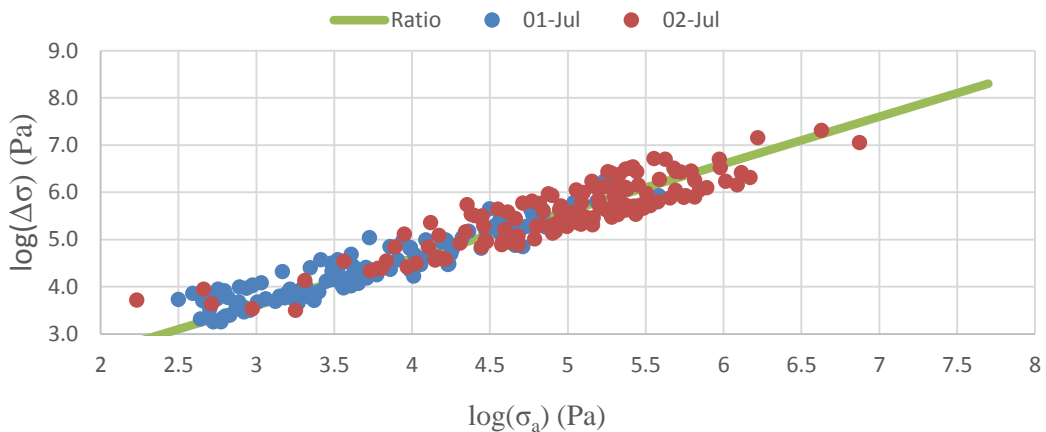


**Figure 5.21 :** Logarithm of apparent stress versus stress drop on July 1 (blue dots) and July 2 (red dots).

Static stress drop of seismic events is shown in Figure 5.22 for July 1 (top) and July 2 (bottom). Stress drop distribution was similar to the apparent stress distribution, shown in Figure 5.17. Average static stress drop was 0.1 MPa for July 1, which is ~10 times lower than the average stress drop on July 2.

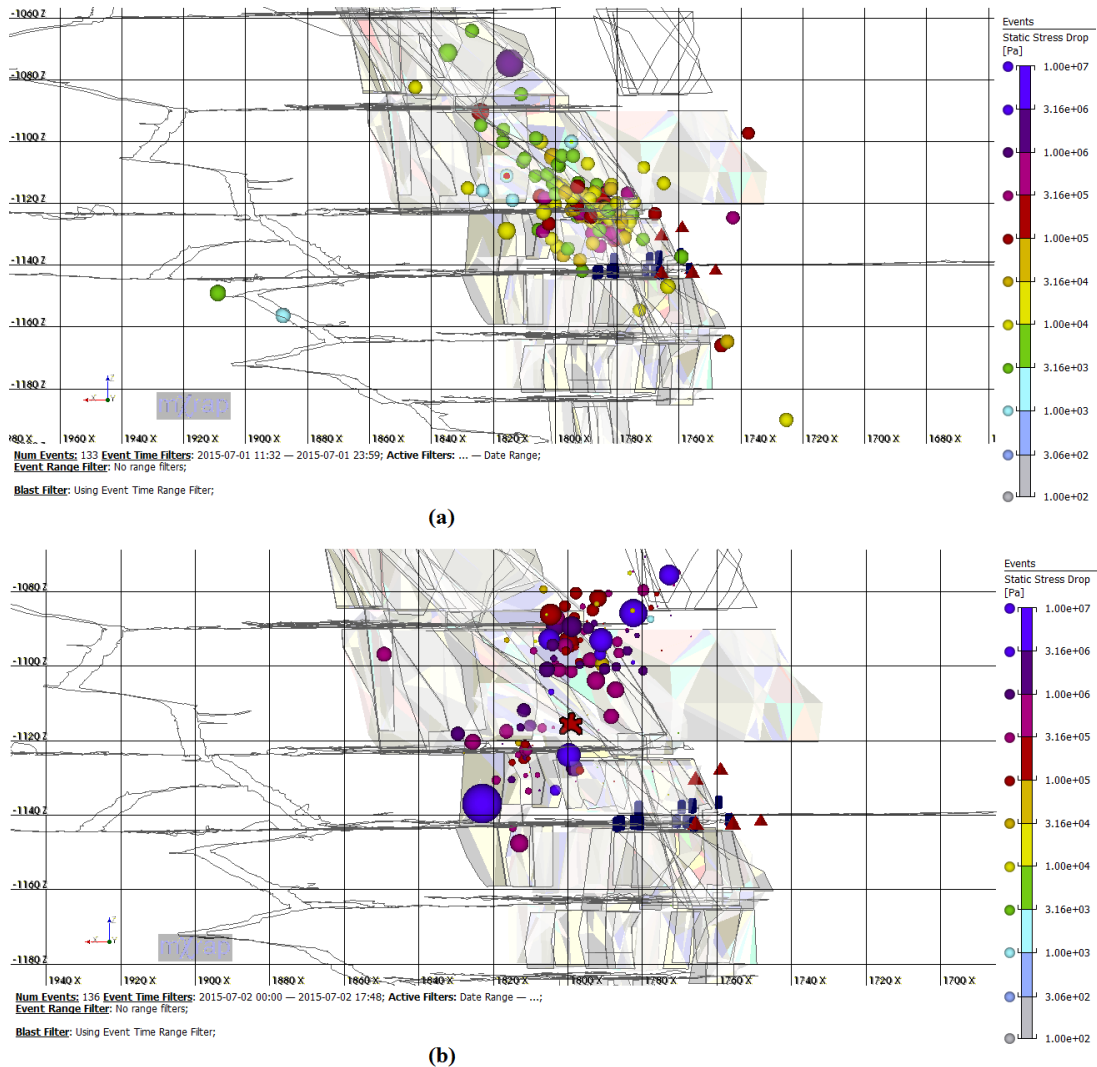


**Figure 5.22 :** Stress drop of seismic events for (a) July 1 and (b) July 2. The color and the size of the circles show the stress drop and local magnitude, respectively.

### 5.3.6 Source radii

Source radius refers to the crack or the fault size. Source size and corner frequency are inversely proportional and corner frequency in general decreases when moment magnitude increases, i.e. the source radius of seismic event must increase with the magnitude. Zinkgruvan local system data mostly comply with that statement (Figure 5.23). The corner frequency and the radius are very sensitive to the high-frequency slope of the spectrum. The change in the slope applied individually for each event ( $\omega^{-$

<sup>2</sup> or  $\omega^{-3}$ ) change substantially the estimated radius to smaller size, respectively larger stress drop (see Equation 3.25).

The largest source radius (37.6 m) was estimated for the event at 16:26 on July 2, Mw 0.2. The second highest source radius was 18.2 m, for the Mw -1.0 event, at 15:13 on July 1. In overall most of the radii were estimated to be less than 5 m with the radii of the events on July 1 comparatively larger than on July 2. The radius of the largest event on July 2, at 15:13, that caused the rockburst was calculated to be 14.7 m.

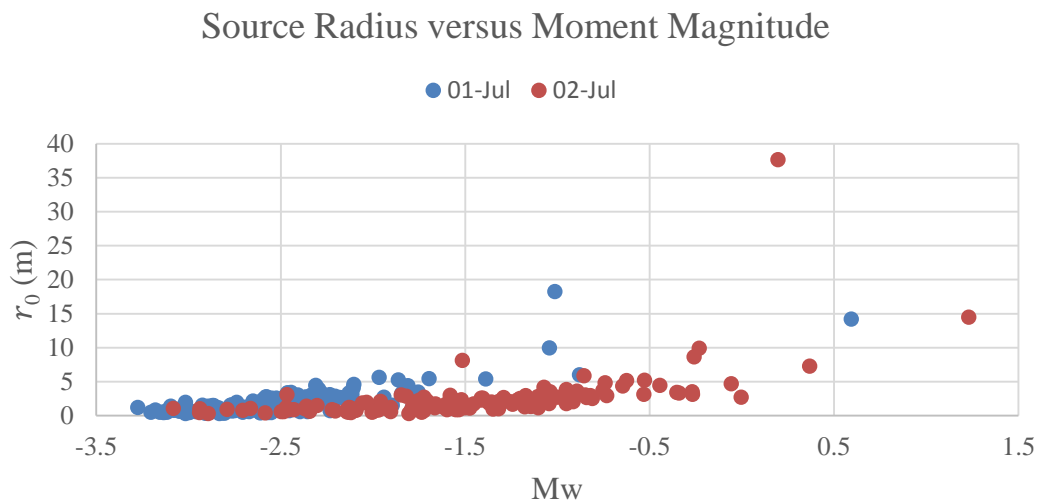


**Figure 5.23 :** Source radius versus moment magnitude on July 1 (blue dots) and July 2 (red dots).

### 5.3.7 Summary and conclusions about the activity in Zinkgruvan

Seismic activity at Zinkgruvan Mine between July 1 and July 2, 2015 has been investigated. The main purpose of this study was to find a relation between seismic activity and blasting, and possible information about the source mechanism of the rockburst on July 2.

The source locations of the seismic events on both days formed individual clusters, with different locations, size, and orientation. Cluster dimensions were around  $\sim 50\text{m} \times 30\text{m} \times 60\text{m}$  and  $\sim 50\text{m} \times 60\text{m} \times 80\text{m}$  for July 1 and July 2, respectively. The cluster orientations were almost perpendicular to each other. The highest moment magnitude events on July 1 and July 2 were on the edges of the clusters but on July 1 at the top and on July 2 on the bottom of the corresponding cluster. In both cases the blast was located in the middle of the corresponding cluster. The moment magnitude of all events



ranged between -3.3 and 1.2 with the events on July 1 generally smaller than on July 2.

In total the dynamic source parameters were calculated for 271 seismic events that occurred on July 1 - 2, 2015. During the calculation the initial default slope of  $\omega^{-2}$  was changed to  $\omega^{-3}$  for almost half of the processed events because the misfit between theoretical and stacked event displacement spectra was smaller for these cases.

Dynamic source parameters of seismic events on both days showed consistently different values and relationships. July 1 seismic events had lower energy, lower apparent stress and stress drop, and larger source radii for the same magnitude than the events on July 2. The apparent stress did not show strong correlation with seismic moment for neither day but in generally increased with the seismic moment increase. Source radii generally increase with moment magnitude. On July 1 the radii were generally lower than 5 meter, with only three values higher than 10 meter. On July 2 the Mw 0.4 event source radius of 37 meter was found, which is the largest size for all seismic events.

As a conclusion, although both blasts were in comparatively close proximity on two consecutive day they caused seismic activity with very different character – number of events, location, and dynamic source parameters. It can be assumed that the seismic activity and the rock response to blasting depend on some factors, as local geology, geomechanical properties and conditions, and possibly pre-existing structures that have to be taken into account in further studies. The orientation of the cluster and dynamic parameters of the events on July 2, 2015 could be used to identify a possible fracture or fault as a source of the main shock. The source radius of 37 m for this event is consistent with the half of the maximum length of the cluster on July 2 (~80 m). The type of the mechanism was found to be non-shear. Both types of information is very important as at this moment the available data do not allow the mechanism of the seismic event to be determined by moment tensor inversion.



## **6. GARPENBERG MINE**

The second dataset of induced seismic events were taken from Garpenberg Mine (Sweden). The same problem on geology is also observed at Garpenberg Mine. The general geology was mentioned to get an idea about the mine site. The mining method and ore body were briefly explained. This study focused on relation between the production blast and rockmass responses and the source parameters similarities and differences of the local and permanent networks and a new methodology was tested.

### **6.1 Geology**

Garpenberg Mine site is located in the middle of Swedish metallogenic province, where iron oxide and sulfide intercalated during early Proterozoic in metamorphic and metasedimentary unit (Vivallo, 1985). Figure 6.1 explains the geological sequences of Garpenberg area. Vivallo (1985) described that volcanic unit formed in shallow water environment.

The subvertical isoclinal fold in northeast direction formed after two different deformation phases (Vivallo, 1985).

From top to bottom, the stratigraphic succession at the Garpenberg mines is given in Figure 6.1. Allen et al (2008), describes these units:

- 1) Upper hanging-wall rhyolitic pumice breccia
- 2) Lower hanging-wall limestone-volcanic breccia-conglomerate sequence
  - a) Matrix-supported, polymict limestone-volcanic breccia with dacitic tuffaceous matrix
  - b) Lenses of rhyolitic and dacitic pumice breccia and ash-siltstone
  - c) Basaltic to andesitic volcanic breccia, sandstone and siltstone
  - d) Clast-supported, polymict limestone-volcanic breccia, crystal-rich sandstone, siltstone
  - e) Clast-supported, limestone breccia-conglomerate

- 3) Limestone (including calcitic marble, dolomite, skarn)
- 4) Upper footwall felsic volcanoclastic succession
  - a) Rhyolitic ash-siltstone
  - b) Rhyolitic pumice breccia-sandstone 48
  - c) Dacitic pumice breccia-sandstone
  - d) Rhyolitic pumice breccia-sandstone, ash-siltstone
- 5) Basalt lava and volcanoclastic rocks
- 6) Lower footwall rhyolitic ash-siltstone and minor coarse volcanoclastic units In addition there are several shallow intrusions:
- 7) Weakly feldspar-porphyrific dacite
- 8) Strongly feldspar-porphyrific dacite
- 9) Weakly feldspar-porphyrific basalt and andesite (commonly actinolite-biotite-epidote rock)

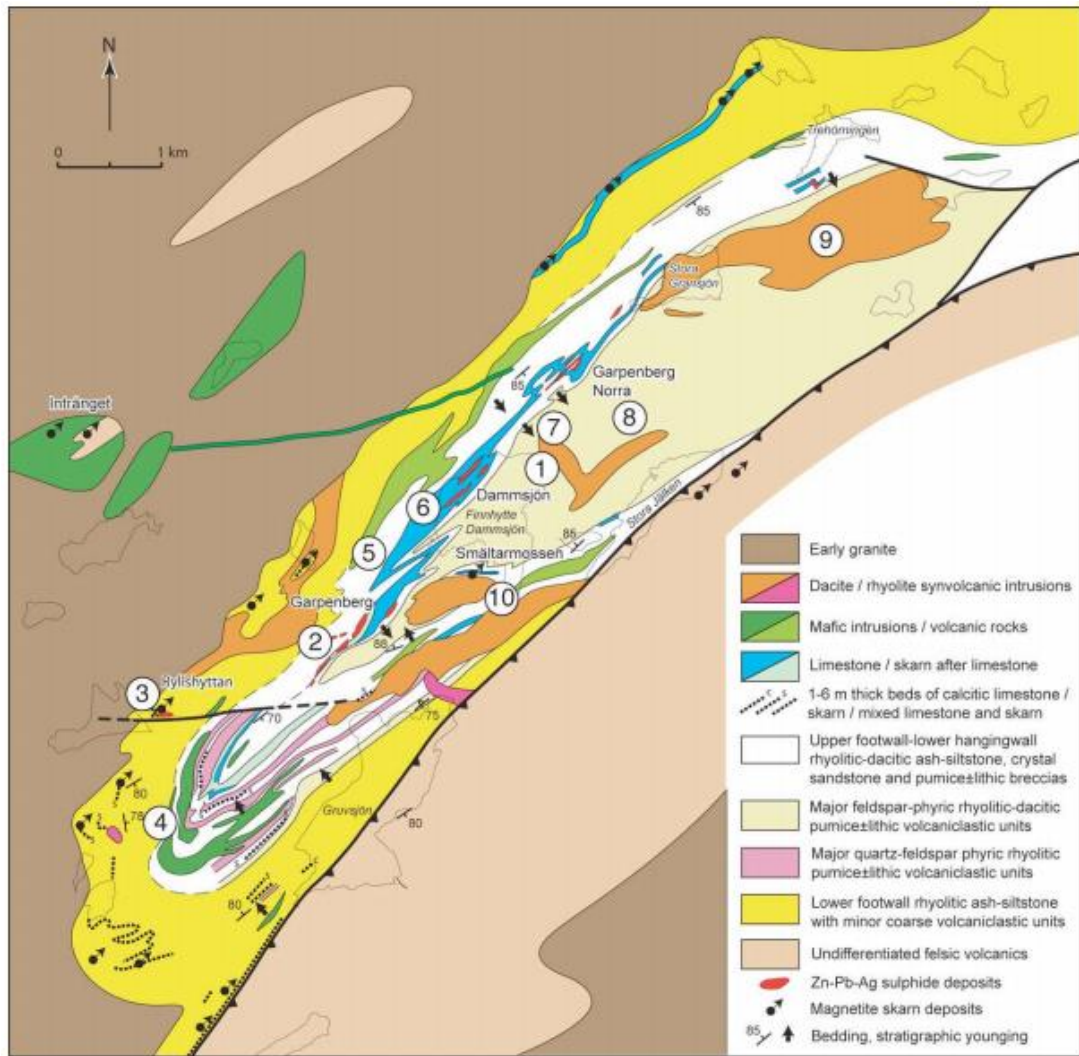


**Figure 6.1 :** Geology map of Garpenberg (Allen et al, 2008).

Garpenberg area has been metamorphosed. This metamorphism could be separated into two stages. M1 metamorphism characterized with alteration and low-pressure and M2 is low grade metamorphism during which amphibolite turned to greenschist (Vivallo, 1985).

## 6.2 Mine Operation

Garpenberg mine is one of the oldest mine sites of Sweden. Production has been continuing since 13<sup>th</sup> century (Allen et al, 2008). Garpenberg ore deposits are irregular and as given in Figure 6.2, multi-lens strata-bound and pod-like (Allen et al, 2008).

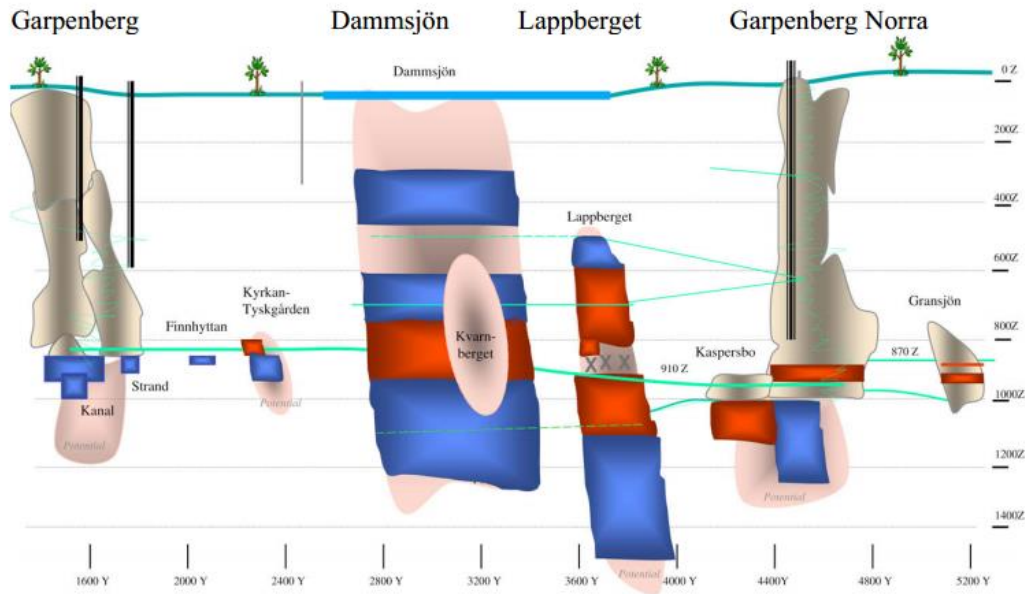


**Figure 6.2 :** Garpenberg mine ore bodies distribution (Allen et al, 2008).

Mining operation has been ongoing between 500 m to 1200 m approximately. Mainly sublevel stopping method was used for extracting the ore (Boliden Garpenberg, 2016).

### 6.3 Seismic Events Data Processing

#### 6.3.1 Seismic systems and data

Seismicity in Garpenberg mine site is monitored by two IMS seismic systems: permanent and local systems. The permanent system was installed in 2012 and the number of sensors increased to 27 at 2015. These sensors are distributed around the whole mine. The local system, which consists of 16 sensors, was installed in 2015 at depth ~720 m in Lapperget ore body. The installed sensors are 4.5 Hz geophones – uniaxial and three-axial (Figure 6.3). The sample rate of the sensors are 12 kHz and 6 kHz for the local and the permanent networks, respectively.

Production blasts are performed almost every day but the seismicity related to them could be recorded by both systems only for a few of them. Production blast on October 10, 2015 was one of the blasts close to the local seismic system (Figure 6.3) and it was the biggest production blast within the given days. Seismic before and after this blast between October 8 and 13, 2015 was the aim of the study.

The seismic events recorded by the permanent and local systems initially were processed by IMS Trace program – manually for the permanent system (routine

processing by IMS) and automatically for the local system. In total more than 1700 seismic events were recorded by both seismic systems for the period 8 to 13 of October, 2015. Subset of these events, recorded well by both system was selected and processed further. The initial comparison of the results obtained by both systems showed that the kinematic and dynamic parameter were not the same and in some cases the difference was much larger than the expected error. In order to find more accurate solutions, manually data processing was done on specific events for data from both systems separately and on merged data.

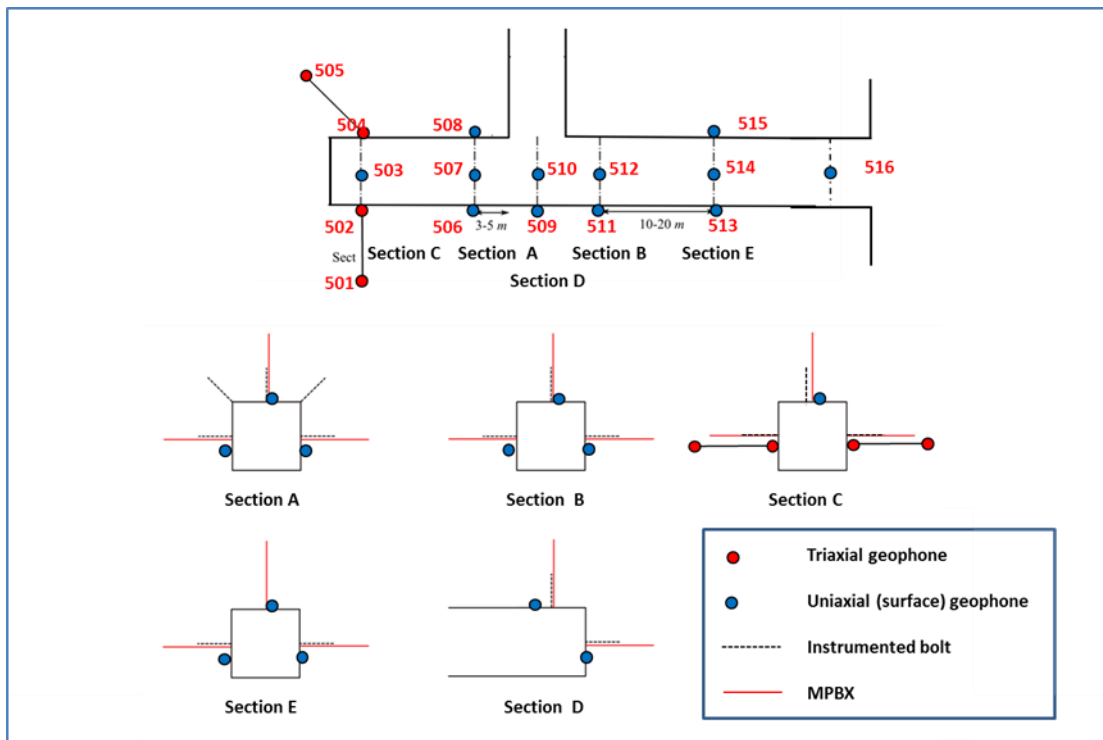


**Figure 6.3 :** Location of the geophones in the local seismic system in Garpenberg mine with the number of the sensor sites. Blue circles are uniaxial (surface) geophones and red circles are three-axial (surface or borehole) geophones. The vertical profiles with the sensor positions are shown too.

These events chosen for the experiment had to have magnitude large enough so that to be recorded by both systems. Most of the higher magnitude events within the given days were close to the local system, because the production blast location was close. Third database was created by merging the data from sensors of both systems. This database is called Merged Database and consisted of 30 events at the beginning of the data processing.

Briefly, data processing was done on total on 90 events recorded by the local seismic system from October 8 to October 13 2015, including 30 events recorded by each seismic systems, and merged database. The kinematic and dynamic source parameters were evaluated in order to determine the most accurate solutions and the factors that affect the accuracy.

**6.3.1 Number of seismic events with time**

Seismic events were recorded between October 8 and 13, 2015. Each system recorded more than 1700 seismic events for this period of time. October 10’s blast caused increase in the number of seismic events recorded by the local system. During the studied period there were also other blasts. Only these blasts close to the local system and clearly visible in the recording are listed in Table 6.1 with their date and approximate time.

**Table 6.1 :** Blasts near the local seismic system in Garpenberg Mine between October 8 and 13, 2015.

<b>Date</b>	<b>Blast Time</b>
08/10/2015	04:00
09/10/2015	04:00 and 16:00
10/10/2015	16:00
11/10/2015	16:00
12/10/2015	16:00
13/10/2015	04:00

Usually the local seismic system does not record large number of real seismic events. There is a lot of noise that triggers the system. On average there are less than 5 events within half an hour (Figure 6.4). The number of events increased dramatically (up to 110 events per half an hour) after the production blast on 10<sup>th</sup> October 2015, and the number of seismic events did not reach ‘normal’ (pre-blasting) level almost 6 hours after the blast. The number of events recorded by the local seismic system are plotted in Figure 6.4 in different color for each day. Although there were other blasts (as shown



in Table 6.1) during the study period they did not cause very dramatic change in the seismic activity, only some increase after the blast on October 11 (Figure 6.4). The largest magnitude events are also shown on the graph. The two largest events – Mw 0.8 and 0.9 occurred after the blasts on October 10 and 11, 2015, respectively.

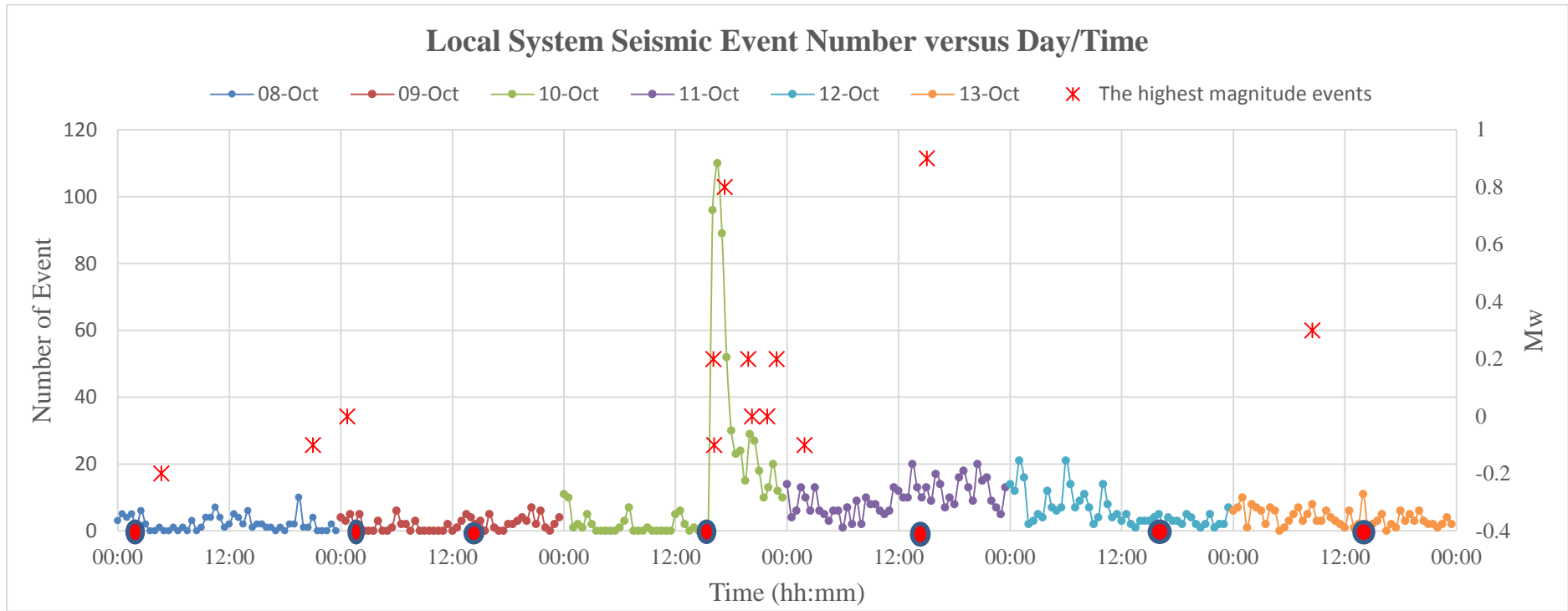


**Figure 6.4 :** Number of seismic events recorded by the local seismic system between October 8 and 13, 2015 (per half an hour). Blasts are marked as red circles. Red crosses show the highest moment magnitude events (the magnitude scale is shown on the right side of the graph).

### 6.3.2 Data processing

This study focused on comparison of kinematic and dynamic parameters obtained by the data from the local and permanent seismic systems and the merged database. Firstly, the local system seismic events were checked and 242 events were eliminated at first place because of the low S/N ratio. In totally 30 events were found with local magnitude higher than -1.5. These events were also recorded by the permanent system. The control parameter was trigger time of the events. If both system recorded the same event, the time differences must be within maximum one millisecond. These events were copied to a new database and permanent and local systems data were merged and processed.

Manual data processing was done on 90 seismic events totally. These dataset consists of equal number of events from merged database, permanent and local systems. Firstly, the blast on October 10 event was processed to define if any possible errors exist in the timing in the local and permanent systems. No problems were found with the timing. The results for the October 10 blast location using all three dataset are given in Table 6.2. The results of the hypocenter location are compared with the ‘real’ surveyed location provided by the mine. The comparison of the results shows that both the depth and east coordinates were calculated with large errors but the north was estimated much better. The location obtained by the permanent system was much better (closer to the ‘real’ one) than the one obtained by the local system. This result indicates that the location calculation of the seismic events might not be very accurate enough either. That is why a test was made to merge the data from both seismic system and to verify if the merged data can allow better accuracy.

It has to be mentioned that the attempt in this study of merging data from both seismic systems was the first one for Garpenberg mine. It has not only scientific but also a practical value for the data processing in the future.

**Table 6.2 :** October 10 production blast location calculations.

	<b>North (m)</b>	<b>East (m)</b>	<b>Depth (m)</b>	<b>Error (m)</b>
<b>Absolute Location</b>	3800.6	498.8	-703.9	0
<b>Local Network</b>	3882.2	563.5	-720.1	105.82
<b>Permanent Network</b>	3787.6	522.0	-720.7	31.03

### **6.3.3 Hypocenter locations**

As mentioned before the initial data processing results, especially in terms of source location, were not very encouraging for seismic events recorded by each - permanent and local systems. The results were very different. It was important to determine which solution was better than the other. In order to give a meaningful answer, the seismic event locations were classified in terms of azimuthal coverage by the sensors.

Seismic events occur the whole mine and the sensor coverage by the permanent system is not optimal for all of them. These sensors are concentrated mainly at deeper levels compared to the local seismic system, which purpose is to monitor a limited area where larger seismic events are expected.

Garpenberg Mine seismic event location is visualized by mXrap software (Figure 6.5). Only 26 events were added to the image because one of the events was a blast and other three seismic events were too far from the rest of the event which formed cluster. Table 6.3 shows all processed seismic event location differences of each networks.

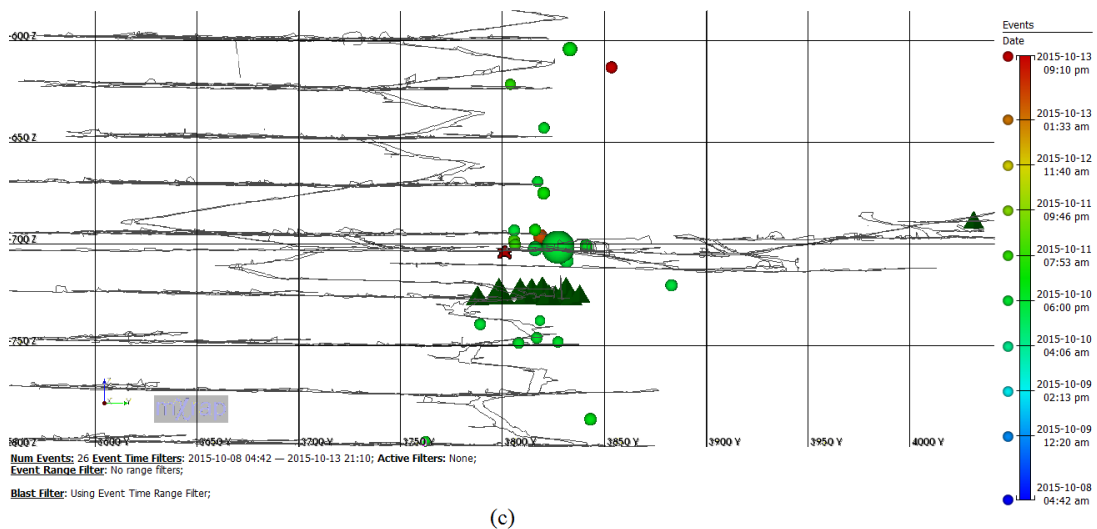
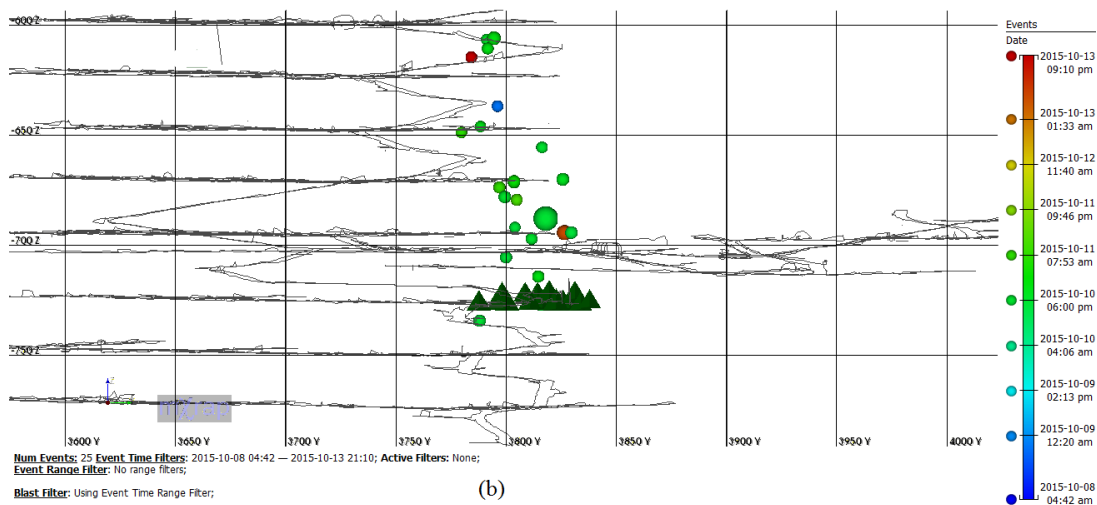
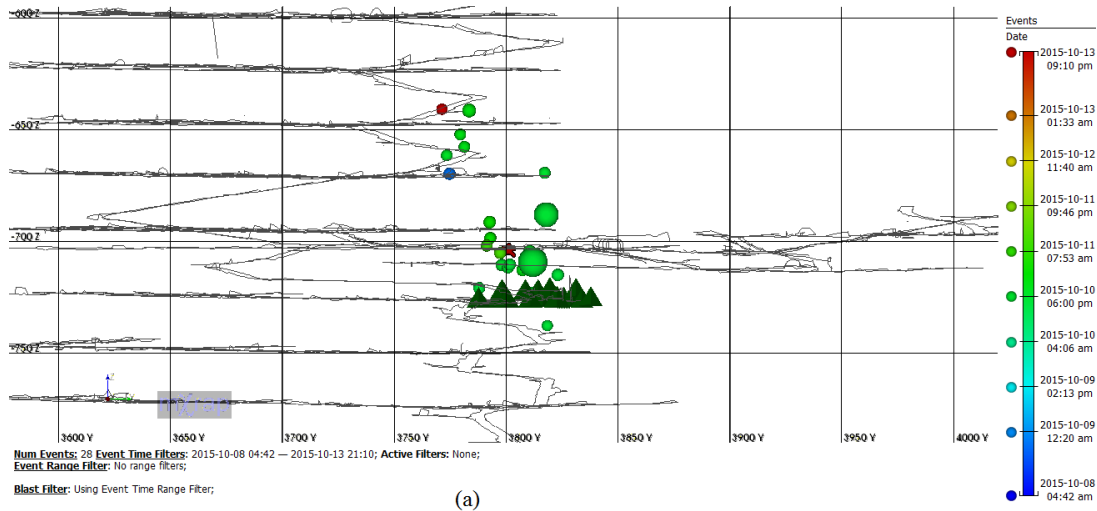


**Figure 6.5 :** Seismic event locations in the (a) Merge Database, (b) Permanent Network and (c) Local Network with event time as color and the circle size representing the seismic event moment magnitude.

**Table 6.3** : Seismic events locations differences.

<b>Good Sensor Coverage</b>									
	<b>Merge to Permanent</b>			<b>Merge to Local</b>			<b>Permanent to Local</b>		
<b>Event</b>	<b>Dif X (m)</b>	<b>Dif Y (m)</b>	<b>Dif Z (m)</b>	<b>Dif X (m)</b>	<b>Dif Y (m)</b>	<b>Dif Z (m)</b>	<b>Dif X (m)</b>	<b>Dif Y (m)</b>	<b>Dif Z (m)</b>
2	2.24	21.45	32.68	63.30	46.87	34.14	65.54	25.42	1.46
6	15.75	6.51	20.56	6.86	8.40	6.78	8.88	1.89	13.78
7	8.08	1.69	4.71	19.03	4.08	17.03	10.95	5.77	12.32
10	5.94	6.05	21.16	4.24	15.35	7.68	1.71	9.30	13.47
11	0.48	0.95	13.60	0.00	0.00	0.00	0.48	0.95	13.60
12	24.23	1.40	32.25	27.89	18.85	35.50	3.66	17.45	67.75
13	10.63	10.75	14.48	15.40	7.06	36.92	4.77	3.69	51.40
15	3.06	17.80	54.63	37.79	46.88	18.57	40.85	29.08	36.05
17	0.04	15.24	34.33	24.97	30.63	3.67	24.93	15.39	30.66
18	8.62	7.04	11.35	30.80	19.17	139.12	22.18	26.20	150.47
19	14.79	7.18	1.57	25.11	35.75	73.26	39.90	28.58	71.69
20	5.49	12.17	41.29	38.87	21.48	181.48	33.38	9.31	222.77
21	3.77	11.02	35.17	51.95	49.61	37.24	48.18	38.59	2.07
29	0.28	13.27	17.22	0.25	5.34	15.46	0.02	7.94	1.75
30	4.88	12.89	26.02	67.62	82.07	27.72	62.74	69.18	1.70

**Table 6.3 (Continued) : Seismic events locations differences.**

<b>Bad Sensor Coverage</b>									
<b>Event</b>	<b>Merge to Permanent</b>			<b>Merge to Local</b>			<b>Permanent to Local</b>		
	<b>Dif X (m)</b>	<b>Dif Y (m)</b>	<b>Dif Z (m)</b>	<b>Dif X (m)</b>	<b>Dif Y (m)</b>	<b>Dif Z (m)</b>	<b>Dif X (m)</b>	<b>Dif Y (m)</b>	<b>Dif Z (m)</b>
1	27.40	5.13	30.55	236.91	116.48	95.28	264.31	121.61	64.73
3	12.40	0.81	14.26	21.00	31.28	84.91	33.40	32.09	99.17
5	247.30	174.56	41.22	8.15	7.53	50.83	255.45	167.04	92.06
8	0.87	0.68	10.09	12.02	15.04	35.50	11.15	14.36	45.59
14	53.72	23.50	11.51	60.60	22.54	16.57	6.88	0.96	5.06
9	56.64	24.47	7.67	50.15	35.87	28.40	6.49	11.40	20.73
24	46.55	29.94	8.29	77.61	42.31	29.54	31.05	12.37	21.25
22	38.80	10.67	27.25	39.51	27.24	23.48	0.71	16.58	3.77
23	30.86	12.93	42.36	15.39	11.15	69.81	15.47	24.08	27.45
25	21.02	5.59	27.94	27.49	14.70	1.57	6.48	9.11	26.37
26	2.12	7.52	25.60	22.04	8.29	6.90	24.16	0.77	18.70

Figure 6.5 shows the location of seismic events of each system individually. The merged, permanent and local network locations were given from top to bottom in Figure 6.5, respectively. The scale and color of the circles represent the moment magnitude and the seismic event time, respectively. The red star shows the October 10<sup>th</sup> blast location from permanent system solution. Table 6.3 shows the results of the comparison of all locations (difference along each coordinate and total distance between the hypocenters). The minimum and maximum difference between hypocenters was found 7.5 m/305 m, 0.5 m/280 m and 8.6 m/318 m for merged to permanent, merged to local and permanent to local databases, respectively. According to Table 6.3, the highest differences in each components of hypocenter were found at permanent and local database comparison. The minimum and maximum values of Y component were always rather lower than other components. The averages of hypocenter difference were lower at merged to permanent database comparison.

### **6.3.3.1 Bad coverage**

Station coverage is an important parameter for determining source location. Each sensor have different travel time depending on distance from seismic event source (Gibowicz and Kijko, 1994). As described in Chapter 3, travel time is related with the arrival time. If sensors are located well around the seismic event, each sensors would be triggered at different time which means that the source location could be define better.

In Garpenberg mine, the sensors of the permanent network are installed mostly below the sensors of the local network in the mine. However, this coverage is not enough to locate all seismic activity around the mine accurately.

To explain the effect on the sensor coverage on seismic activities, the seismic events were classified as their sensor coverages. In this chapter was focused on mainly examples of “bad” sensor coverage, but in Chapter 6.3.3.2 the “good” sensor coverage will be discussed. There were two examples about “bad” sensor coverage and the results of kinematic and dynamic source parameters were compared with respect to networks. Figure 6.6 (ray paths) and Figure 6.7 (waveform with arrival time) show the seismic event at 04:42 on October 8, 2015 location and waveforms. Moreover, Table 6.4 shows the source parameters of this seismic event. On the other hand, Figure 6.8



(ray path) and Table 6.5 show another “bad” coverage example at 16:04 on October 10, 2015.

The hypocenter locations for each seismic system were far from each other. The merged to permanent system source location difference was 41 m. The source location differences were more than 200 meter for merged to local and permanent to local comparison. The main reason is that the local network could covers only a small angle around the hypocenter if it is far away.

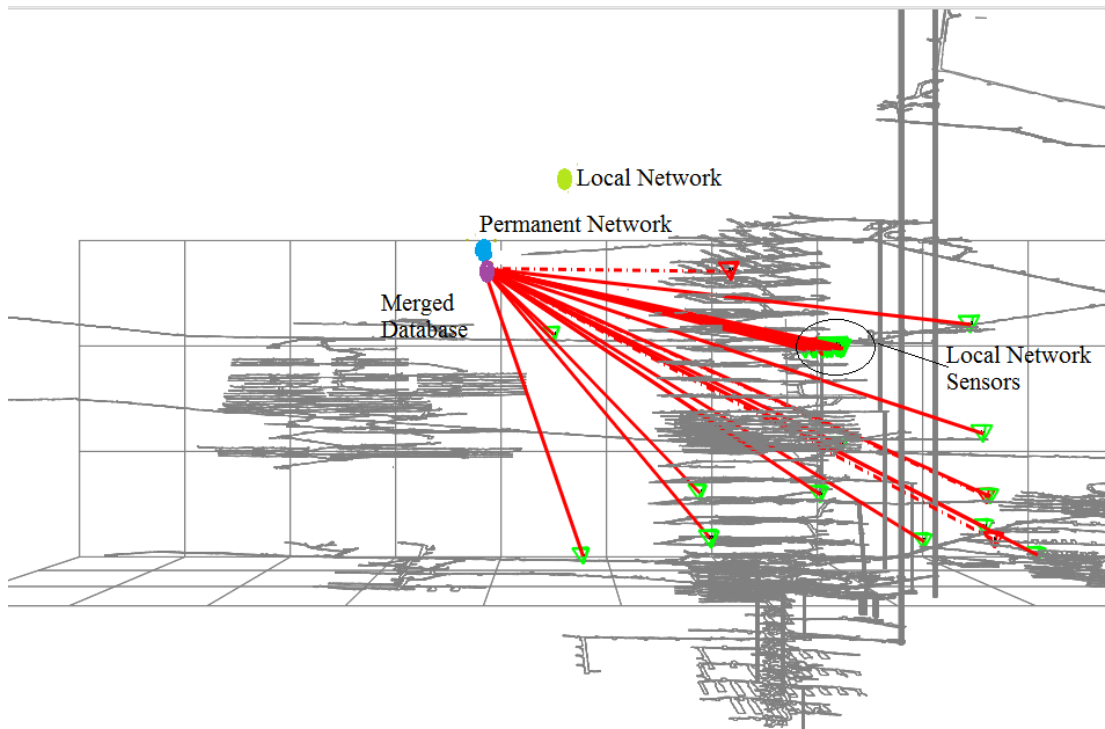


**Figure 6.6 :** The ray path fort the seismic event at 04:42 on October 8, 2015 and the theoretical ray paths from the sensors (red lines) (case of bad sensors coverage).

Table 6.4 shows how source parameters changed with respect to seismic network in this case of bad coverage. As seen from this table, there was no significant difference in the hypocenter location in Y-direction. However, the differences in X-direction and depth were very large, especially between the results for the local system compared with the two other cases – the permanent and merged data. Each one of the dynamic parameters also changed depending on the data used for the calculation. The largest effect was on the corner frequency, energy, apparent stress and stress drop.

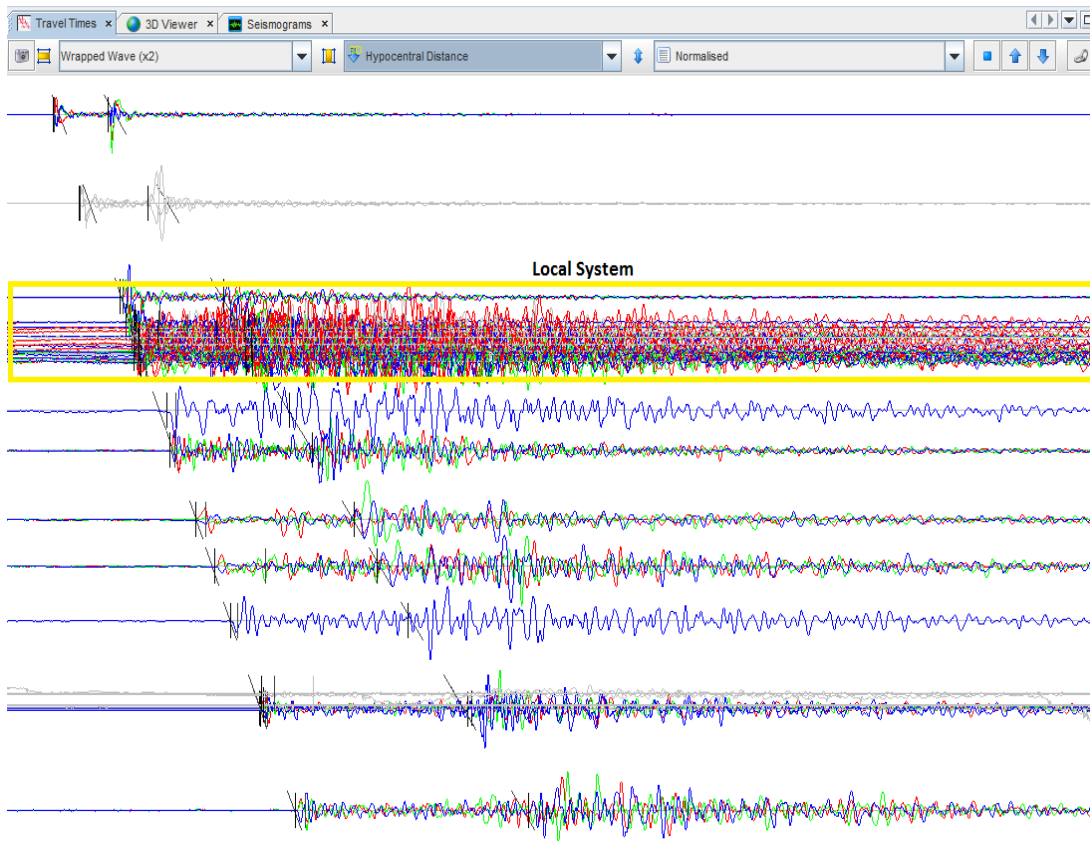


**Figure 6.7 :** Travel times for the event at 04:42 on October 10, 2015.

The energy from the permanent network solution was 4 to 6 times higher than the energy from the local or merged data. This data was a very important example because energy of the permanent seismic events were generally 4 to 6 times lower. Most probably this a results of the small angle coverage and effect of the radiation pattern. As the amplitudes and the seismic energy vary around the seismic source following the radiation pattern, when the coverage is too small the energy might be too high or too small depending on the orientation of the source mechanism, compared with, averaged over larger angle around the source of permanent system. The corner frequency also changed depending on the dataset. Because of that, the stress drop and source radius were also obtained with large differences. Despite the large difference also in the  $E_s/E_p$  ratio the type of the event remained the same for all dataset – non-shear event.

**Table 6.4** : Source parameters of October 8, 2015 at 04:42.

08/10/2015 04:42			
	Merged	Permanent	Local
LocX [m]	497.5	524.9	260.6
LocY [m]	3296.9	3291.8	3413.4
LocZ [m]	-604.9	-574.3	-509.6
AHD [%]	1.6	1.2	1.0
Local Magnitude	-1.3	-1.0	-1.3
Moment Magnitude	-0.2	-0.1	-0.3
Energy [J]	152.2	899.1	195.7
Energy P [J]	40.5	91.9	30.2
Energy S [J]	111.7	807.2	165.5
EnergyS/EnergyP	2.8	8.8	5.5
Moment [Nm]	6.2E+08	9.2E+08	4.5E+08
Moment P [Nm]	1.0E+09	1.5E+09	7.3E+08
Moment S [Nm]	3.1E+08	3.5E+08	2.4E+08
Corner Freq [Hz]	148.7	278.0	172.1
Apparent Stress [Pa]	8065.5	32381.3	14445.0
Source Radius (Brune) [m]	8.8	4.7	7.6
Static Stress Drop [MPa]	0.2	1.0	0.2

After the blast on October 10 at 16:04 another seismic event was recorded. The average moment magnitude of this seismic event was -0.1 and this event was recorded by all sensors of local system. Figure 6.8 shows the source location of the seismic event at 16:04 on October 10, 2015 obtained by the local, permanent, and merge dataset. This seismic event is a very good example of how the location could change if more sensors are added. Each one of the system – the local and the permanent systems had not very good sensor coverage but the combination of the sensors of both systems –merged dataset had much better coverage. As seen in small picture at right up side (Figure 6.8

b), the local sensors give source location above the sensor plane. When the permanent system sensors are used for the source location solution, the location was found below the local seismic system plane (Figure 6.8 c). Although four sensors of permanent system recorded this event, only two of them was used, because of the low S/N ratio on the other two.

The dynamic source parameters were given in Table 6.5. This seismic event source parameters were not same path with previous example. The highest dynamic source parameter values, except corner frequency, were found local system solution. Although the corner frequency of merged and local system, the apparent stress and static stress drop are close to each other. Energy generation of seismic event were not in same pattern which effected the origin of event. Local network pointed out that this event was shear. Even though, merge database and permanent network solution specified it as non-shear event. That changes could be explained by attenuation till some point but further studies are needed.

The source location of each system shows huge differences. The higher differences in location were in both X-direction and depth. The error on location was similar with the previous bad sensor coverage example. It could be said that the source location accuracy is the biggest challenge if event was not covered well by sensors.

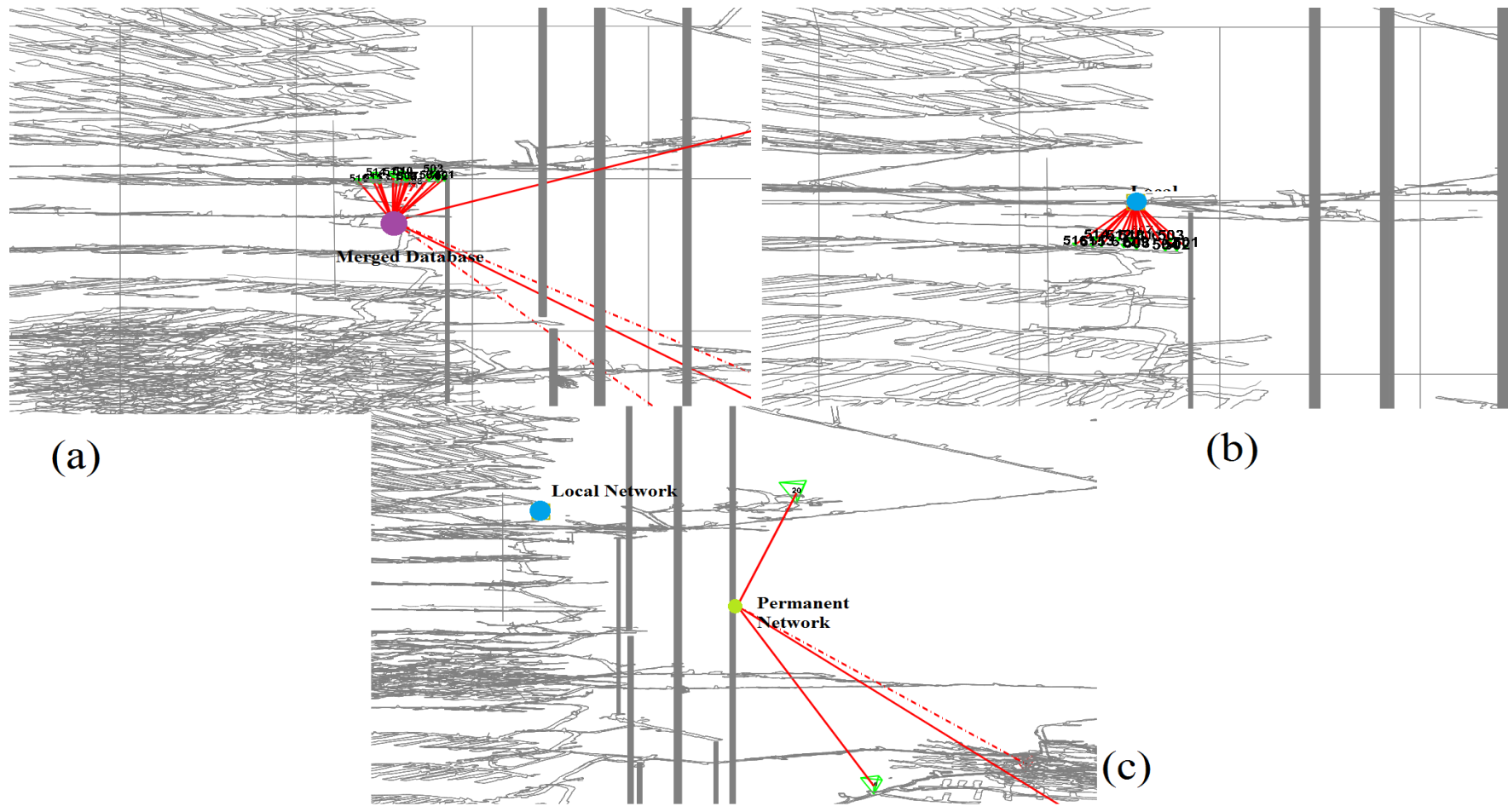


**Figure 6.8 :** Seismic event locations calculated with data from (a) Merged Dataset, (b) Local Network and (c) Permanent Network. The red lines are the theoretical ray paths from the sensors (case of bad sensor coverage).

**Table 6.5** : Source parameters of October 10, 2015 at 16:04.

<b>10/10/2015 16:04</b>			
	Merged	Permanent	Local
<b>LocX [m]</b>	537.5	290.2	545.7
<b>LocY [m]</b>	3808.2	3982.7	3815.7
<b>LocZ [m]</b>	-752.9	-794.1	-702.1
<b>AHD [%]</b>	5.1	1.3	9.3
<b>Local Magnitude</b>	-0.2	-0.7	0.0
<b>Moment Magnitude</b>	0.2	0.1	0.3
<b>Energy [J]</b>	4.2E+04	2.0E+03	6.0E+04
<b>Energy P [J]</b>	2.8E+03	5.4E+02	2.9E+03
<b>Energy S [J]</b>	3.9E+04	1.4E+03	5.7E+04
<b>EnergyS/EnergyP</b>	13.6	2.6	19.7
<b>Moment [Nm]</b>	2.3E+09	1.8E+09	3.2E+09
<b>Moment P [Nm]</b>	2.8E+09	3.6E+09	3.0E+09
<b>Moment S [Nm]</b>	2.3E+09	7.6E+08	3.2E+09
<b>CornerFreq [Hz]</b>	214.5	198.3	192.0
<b>Apparent Stress [Pa]</b>	5.9E+05	3.5E+04	6.1E+05
<b>Source Radius (Brune) [m]</b>	6.8	6.7	6.8
<b>StaticStressDrop [MPa]</b>	4.2	0.9	4.8

### 6.3.3.2 Good sensor coverage

The event at 16:10 on 10 October 2015 is an example of good sensor coverage. The event location and sensor distribution are given on Figure 6.9. Unlike previous examples, the locations obtained for all systems and merged dataset were close together.

Figure 6.10 gives the merged dataset waveforms at 16:10 on 10 October 2015. The local sensor were very close to hypocenter. Because of that, the discrimination of P and S waves was difficult, however, total AHD was less than 5%.

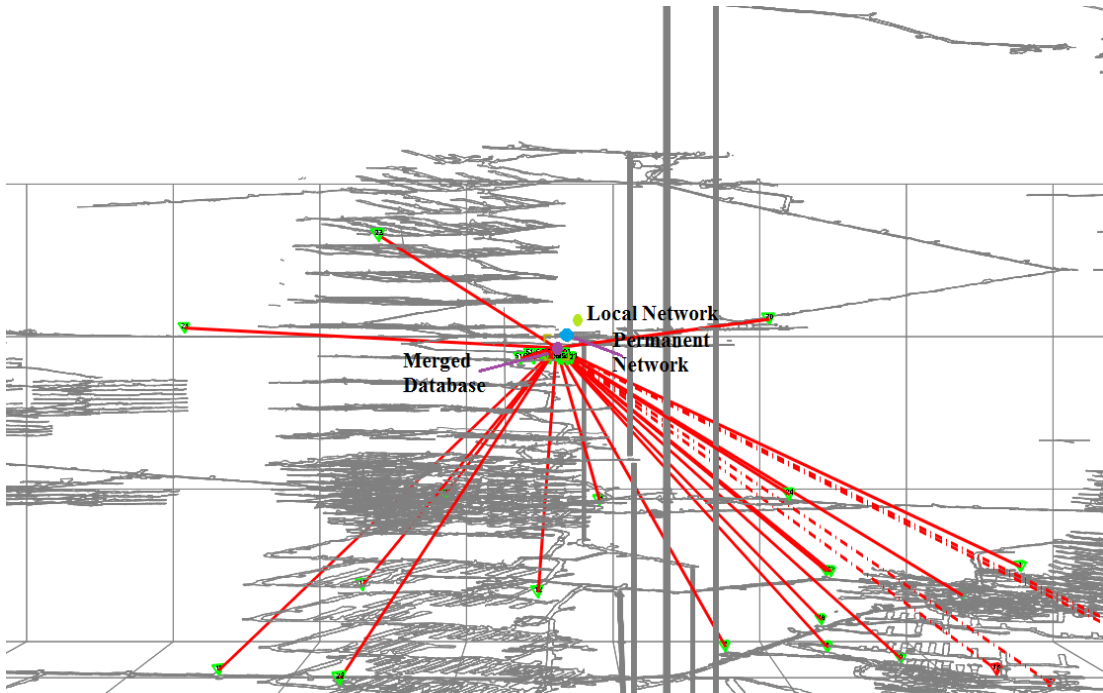


**Figure 6.9 :** Ray path of the seismic event at 16:10 on 10-October 2015 (red lines represent the theoretical ray paths to the sensors (example of good sensors coverage)).

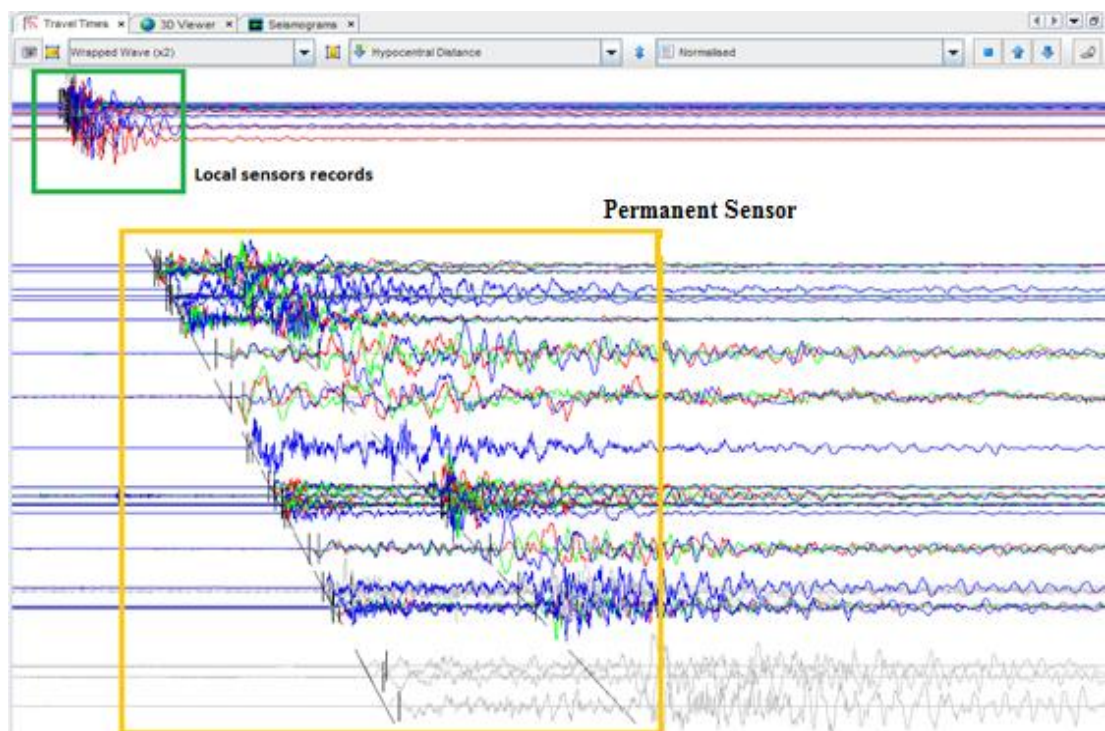


**Figure 6.10 :** Travel times for the event at 16:10 on 10-October 2015.

Merged, permanent and local dataset solutions are given in Table 6.6. The total location differences were 26 m, 16 m and 12 m for Merge-Permanent, Merge-Local and Permanent-Local, respectively. These differences are comparable with the real

accuracy of the hypocenter locations. Moment magnitudes and seismic moment of the seismic event were also close to each other. The highest seismic moment and energy were calculated by the local system as in the cases of the bad coverage. This event was found as a shear event from the local data but shear for the other two cases.

**Table 6.6** : Source parameters of October 10, 2015 at 16:10.

<b>10/10/2015 16:10</b>			
	Merge	Permanent	Local
<b>LocX [m]</b>	502.7	518.5	509.6
<b>LocY [m]</b>	3822.7	3829.2	3831.1
<b>LocZ [m]</b>	-714.9	-694.3	-708.1
<b>AHD [%]</b>	3.5	2.3	3.6
<b>Local Magnitude</b>	-0.9	-1	-0.3
<b>Moment Magnitude</b>	-0.1	-0.1	0.3
<b>Energy [J]</b>	1297.0	450.1	13207.1
<b>Energy P [J]</b>	159.0	74.2	366.9
<b>Energy S [J]</b>	1138.2	376.0	12840.2
<b>EnergyS/EnergyP</b>	7.2	5.1	35.0
<b>Moment [Nm]</b>	8.89E+08	9.57E+08	3.27E+09
<b>Moment P [Nm]</b>	1.45E+09	1.95E+09	1.01E+09
<b>Moment S [Nm]</b>	5.8E+08	4.56E+08	3.52E+09
<b>CornerFreq [Hz]</b>	126	104	80
<b>Apparent Stress [Pa]</b>	4.8E+04	1.6E+04	1.3E+05
<b>Source Radius (Brune) [m]</b>	10.3	12.5	16.2
<b>Static Stress Drop [MPa]</b>	0.2	0.1	0.3



According to this result, the Merge-Permanent results were close to each other. If the event had a good coverage, the source locations were reliable, and the dynamic parameters too.

### 6.3.4 Magnitude, seismic moment, and energy distributions

Although the dynamic parameters obtained from data from the local, permanent and merged dataset are in the same range, they are not exactly the same for each event. Figure 6.11 shows the seismic events energy versus moment magnitude for each dataset. According to the graph, the energy of the seismic events obtained from the local system is the highest. The moment magnitude differences of each system for each event are given in Table 6.7. The local system moment magnitudes are generally larger than the rest of them with maximum difference of 0.2 magnitude units. The second largest moment magnitudes were found in the merge dataset. These values are also highest for the local system. The graph in Figure 6.12 shows how seismic moment changes with respect to events code (number), given in Table 6.7.

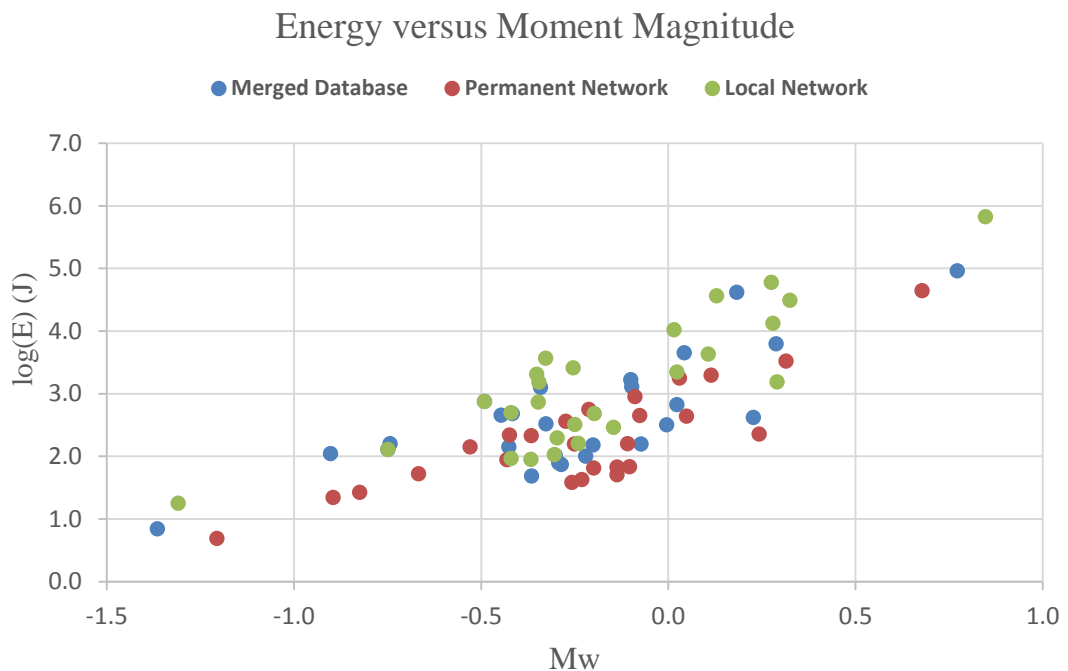


**Figure 6.11** : Logarithm of energy versus seismic moment. The green, red and blue dots represent the local network, the permanent network and merged dataset, respectively.

**Table 6.7** : Processed seismic events moment magnitude with respect to seismic networks.

Day and Time	Code of the events	Moment Magnitude		
		Merged	Permanent	Local
08/10/2015 04:42:54	1	-0.2	-0.1	-0.3
08/10/2015 21:00:01	2	-0.1	0.0	-0.3
09/10/2015 00:42:58	3	0.0	-0.1	-0.1
10/10/2015 16:04:42	5	0.2	0.1	0.3
10/10/2015 16:10:40	6	-0.1	-0.1	0.0
10/10/2015 16:38:03	7	-0.4	-0.3	-0.3
10/10/2015 16:43:58	8	-0.7	-0.9	-0.7
10/10/2015 16:51:39	9	-1.4	-1.2	-1.3
10/10/2015 17:18:45	10	0.8	0.7	0.8
10/10/2015 17:53:47	11	-0.5	-0.4	-0.5
10/10/2015 18:13:25	12	-0.3	-0.3	-0.4
10/10/2015 18:14:05	13	-0.7	-0.7	-0.3
10/10/2015 18:18:21	14	-0.9	-0.8	-0.4
10/10/2015 19:06:20	15	-0.3	-0.1	-0.4
10/10/2015 19:50:59	16	0.2	-0.1	0.4
10/10/2015 20:14:02	17	0.0	0.1	0.1
10/10/2015 21:24:42	18	-0.3	-0.1	-0.2
10/10/2015 21:53:17	19	0.0	0.2	0.1

**Table 6.7 :** Processed seismic events moment magnitude with respect to seismic networks (Continued).

Day and Time	Code of the events	Moment Magnitude		
		Merged	Permanent	Local
<b>10/10/2015 22:07:11</b>	20	-0.2	0.1	-0.1
<b>10/10/2015 22:52:53</b>	21	0.2	0.2	0.0
<b>11/10/2015 01:31:53</b>	22	-0.6	-0.4	-0.2
<b>11/10/2015 01:53:22</b>	23	-0.1	-0.2	0.0
<b>11/10/2015 07:06:45</b>	24	-0.3	0.0	-0.3
<b>11/10/2015 08:37:01</b>	25	-0.4	-0.4	-0.5
<b>11/10/2015 12:06:34</b>	26	-0.3	-0.3	-0.5
<b>11/10/2015 15:03:56</b>	27	0.9	0.8	1.0
<b>11/10/2015 16:04:17</b>	28	0.0	0.0	0.0
<b>13/10/2015 08:30:40</b>	29	0.3	0.3	0.3
<b>13/10/2015 21:10:07</b>	30	-0.4	-0.1	-0.4

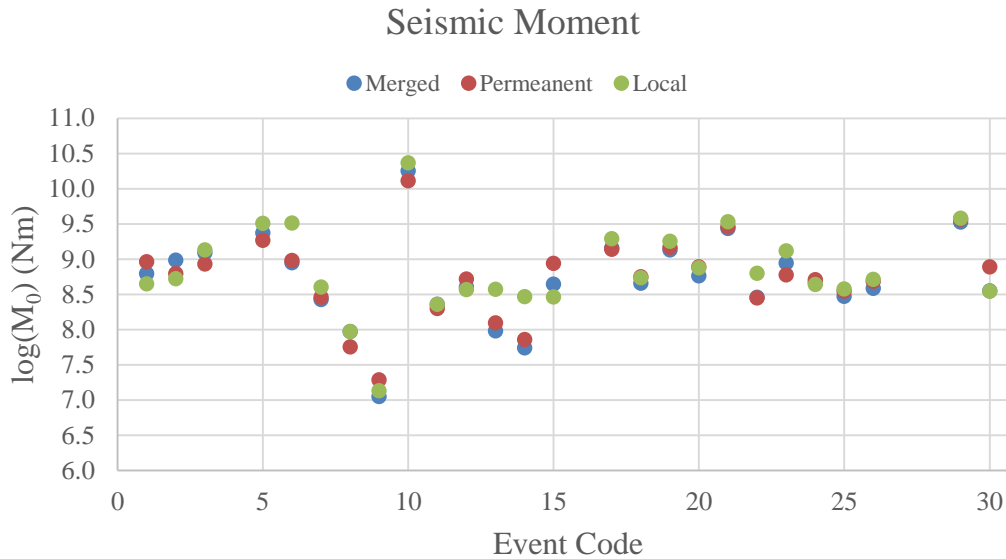


**Figure 6.12 :** Seismic moment changing with respect to the events code (number). The green, red and blue dots represent the local network, the permanent network and merged dataset, respectively.

Table 6.8 shows the highest/lowest values of some source parameters. The listed source parameters calculated by local system source parameters are always higher than the other systems. The results are summarized with respect to the seismic system:

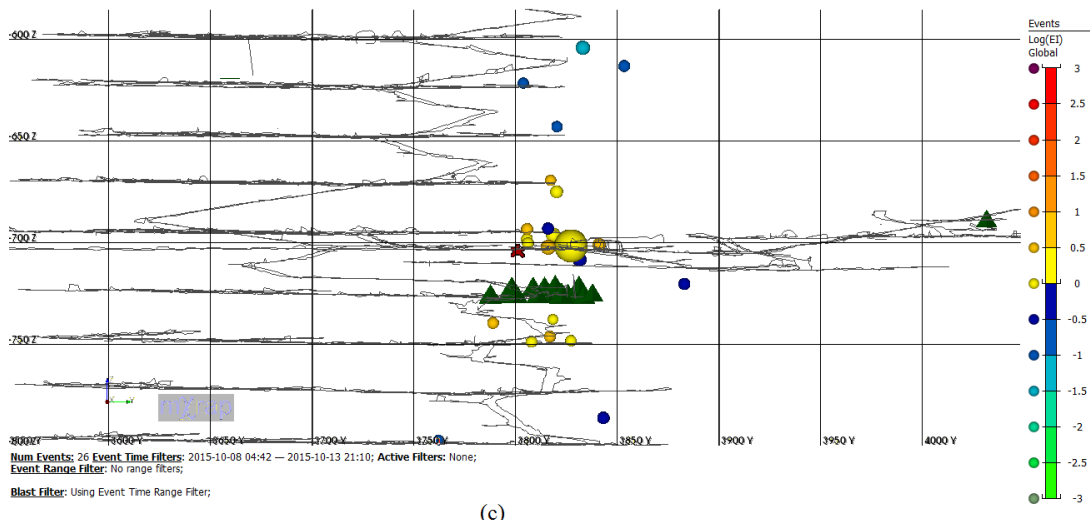
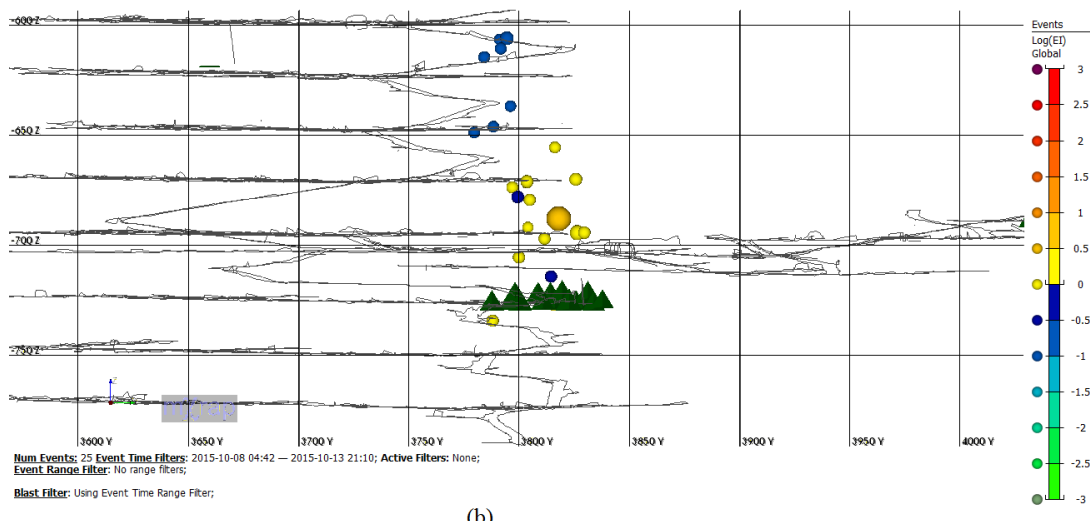
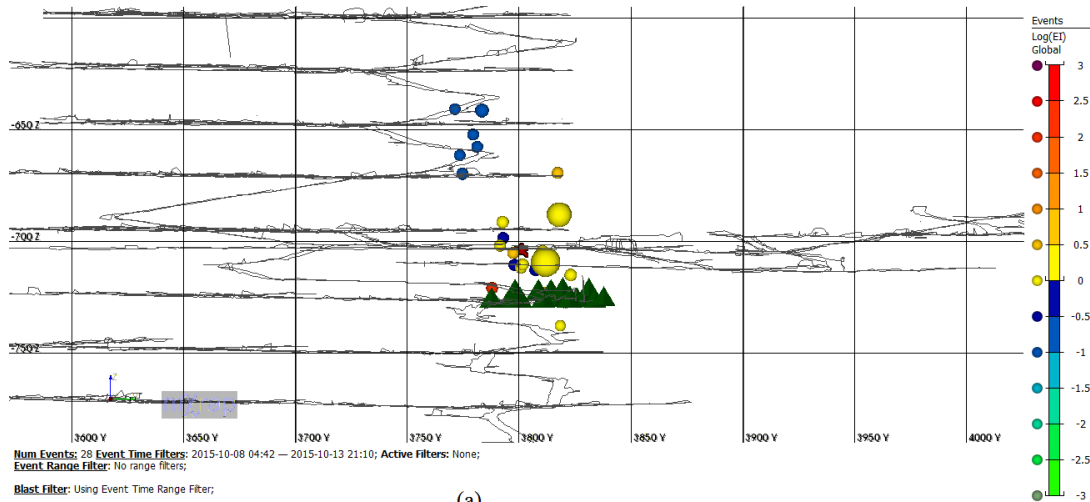
- Merged Database: Moment magnitude range is between -1.4 and 0.8 and only 7.6% of total events were shear events. The largest moment magnitude event was recorded at 17:18 on October 10, 2015. Moreover, the maximum values of source parameters were found for that event.
- Permanent Network: Moment magnitude varies between -1.2 and 0.7. The highest values of the moment magnitude 0.7 was found for the same event on October 10, 2015 at 17:18 event. All of the permanent system seismic events were non-shear events.
- Local system: Moment magnitudes were between -1.2 and 0.7. The highest moment magnitude was the same as for the other datasets. The local system data showed that 36% of the events were non-shear. This results did not match the results from the merge and permanent systems.

**Table 6.8 :** The highest and the lowest values of some source parameters.

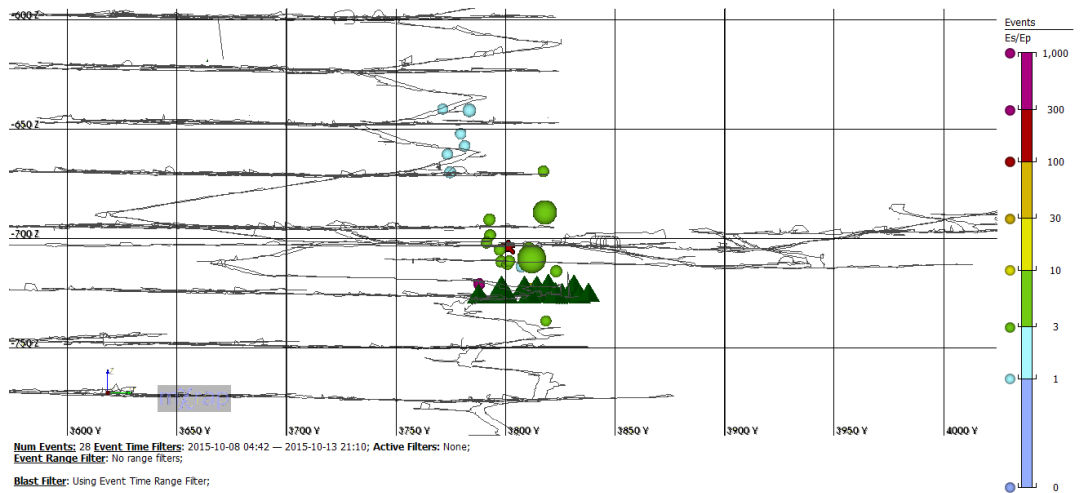
		Seismic Energy (J)	Seismic Moment (Nm)	Apparent Stress (Pa)	Stress Drop (MPa)	Source Radius (m)
<b>Merged Database</b>	The Highest	9.1E+04	1.8E+10	5.9E+05	4.2E+00	3.3E+01
	the Lowest	6.9E+00	1.1E+07	4.5E+03	2.3E-02	3.4E+00
<b>Permanent Network</b>	The Highest	4.4E+04	1.3E+10	1.1E+05	1.5E+00	4.2E+01
	The Lowest	4.9E+00	1.9E+07	2.2E+03	2.1E-01	3.0E+00
<b>Local Network</b>	The Highest	6.7E+05	2.3E+10	9.5E+05	5.1E+00	4.2E+01
	The Lowest	1.8E+01	1.4E+07	8.1E+03	4.3E-02	3.4E+00

Figure 6.13 shows the hypocenter location defined with the data from the merged database (top), permanent system (middle) and local network (bottom). The size of the circle represents the moment magnitude and their color the seismic energy. Seismic events with lower moment magnitude generally radiated lower energy. However, some higher moment magnitude events also had lower seismic energy. The lowest seismic energy events were located at the upper part of the cluster in each case. The seismic energy of calculated by the local network was relatively higher than in the other two cases.

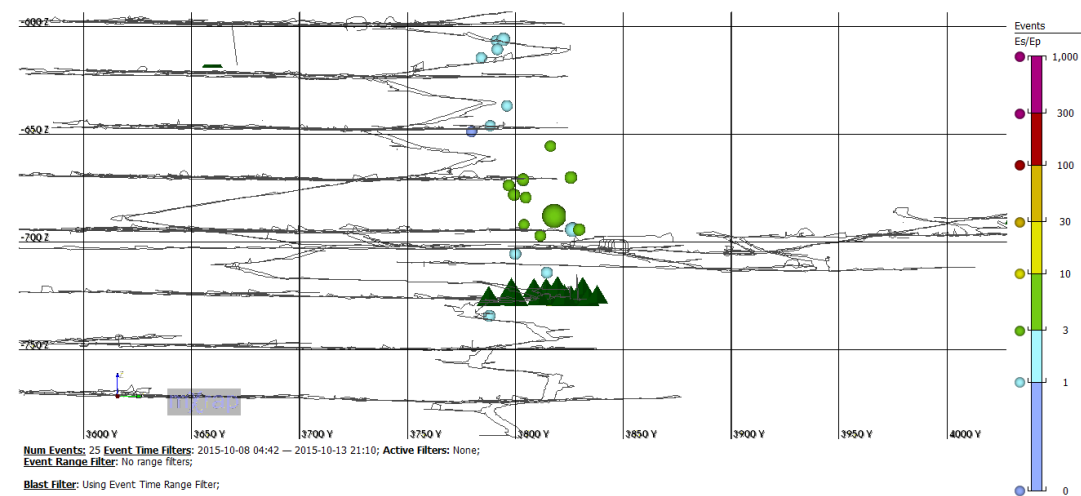
The  $E_s/E_p$  ratio of the seismic events obtained separately from the merged database, the permanent and local systems are shown in Figure 6.14. The type of the seismic events was defined based on the  $E_s/E_p$  ratio. The events in the most upper part of the cluster were almost pure tensile events ( $E_s/E_p < 3$ ) (light blue color) based on the data from all three databases. The events with locations close to the local sensors showed non-shear type for the merged and permanent network databases but mostly shear type for the local database with  $E_s/E_p$  ratio mostly between 10 and 30.



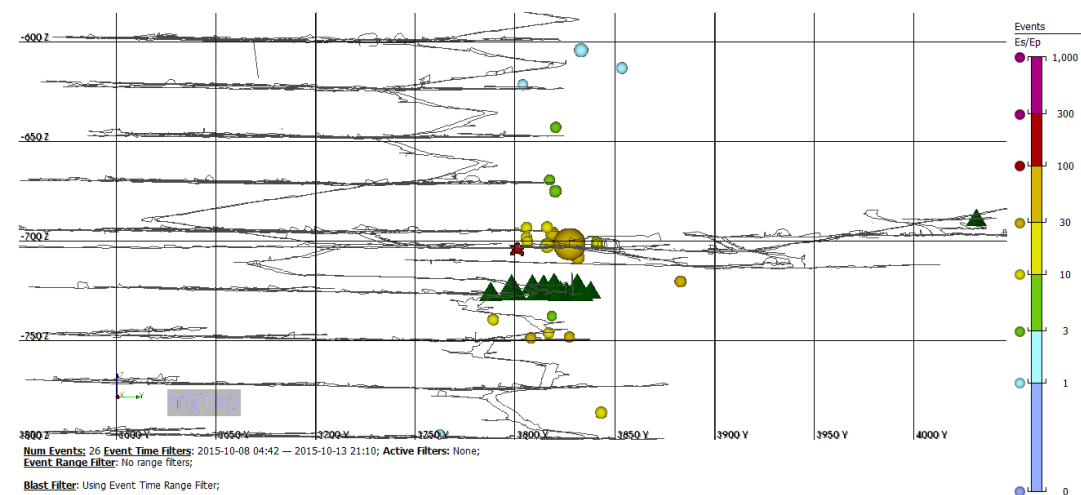
**Figure 6.13** : Seismic energy of seismic events of (a) merged database, (b) permanent network and (c) local network. The green triangles show the local network sensors and the size of the circles represent the moment magnitude.



(a)



(b)



(c)

**Figure 6.14 :** Seismic energy of seismic events of (a) merged database, (b) permanent network and (c) local network. The green triangle shows the local network sensors and the size of the circles represent moment magnitude.

### 6.3.5 Apparent stress and stress drop

Stress drop is dependent parameters on the corner frequency. An increment in the corner frequency results to a decrement on the stress drop. The apparent stress is not dependent on the corner frequency but it is calculated directly from the seismic energy and seismic moment. The minimum and maximum values of apparent stress and stress drop are given in Table 6.8.

Figure 6.15 shows how apparent stress changes with respect to the seismic moment for individual networks. According to that, the local system apparent stress solutions are the highest and the lowest values are seen in the permanent network. There is some weak trend of increasing in the apparent stress with seismic moment.

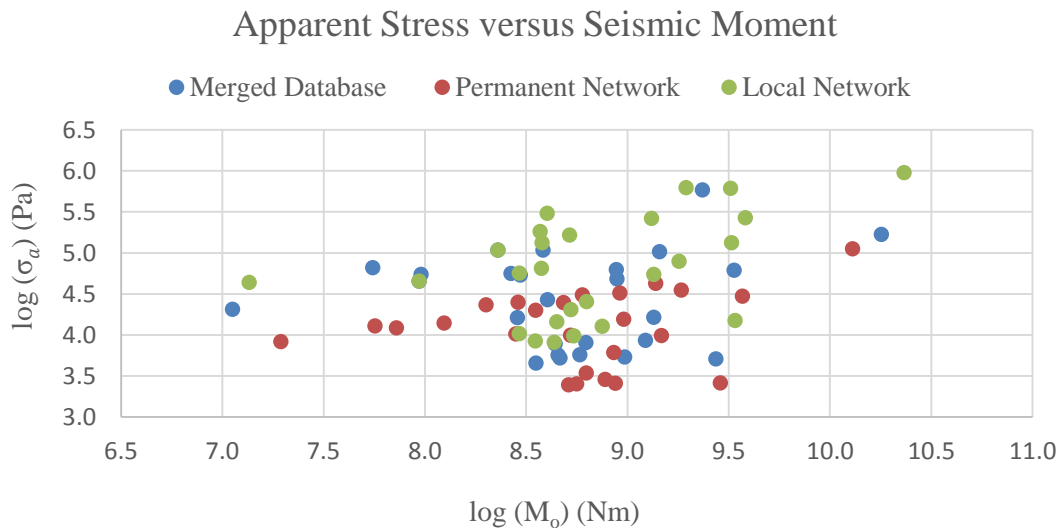


**Figure 6.15 :** The logarithm of apparent stress versus logarithm of seismic moment. The green, red and blue dots represent the local network, the permanent network and merged dataset, respectively.

The logarithm of apparent stress and energy graph is shown in Figure 6.16. According to the graph, apparent stress increased with seismic energy. It is obvious that the permanent network events apparent stress and the energy is lower than rest of the system and the correlation of apparent stress relation to seismic energy was in low degree. The trend of the apparent stress and the seismic energy of merged dataset was more chaotic.



## Apparent Stress versus Seismic Energy

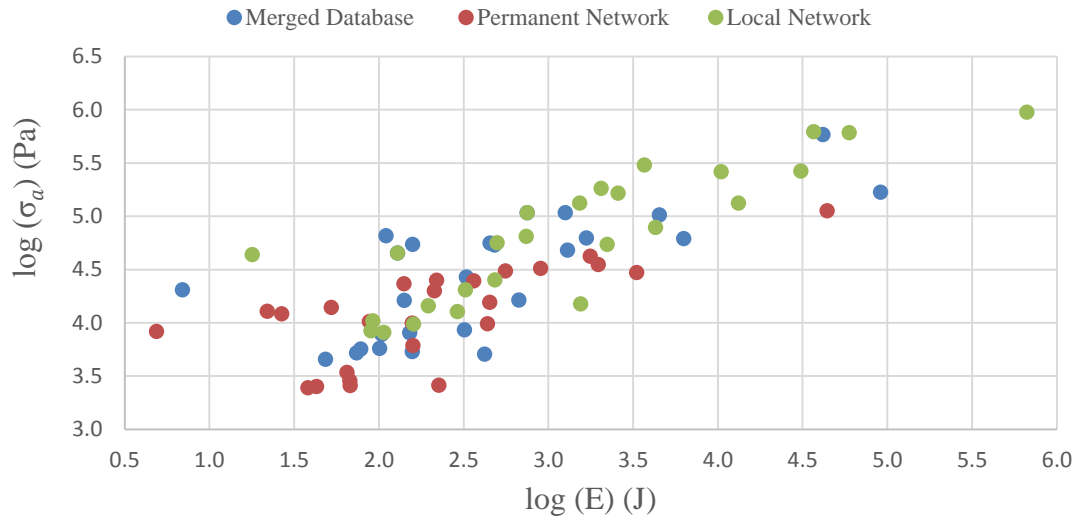
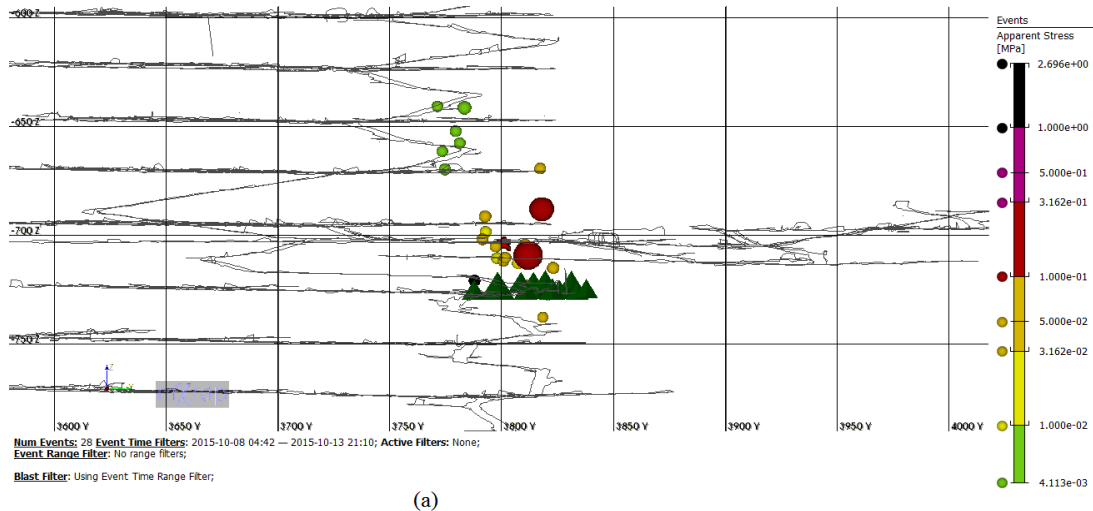
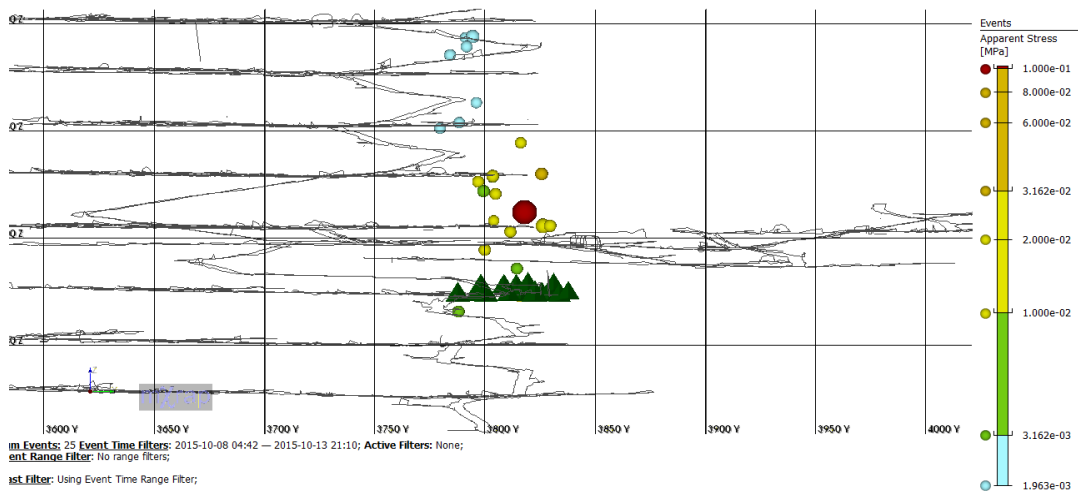


**Figure 6.16 :** The logarithm of apparent stress and energy. The green, red and blue dots represent the local network, the permanent network and merged dataset, respectively.

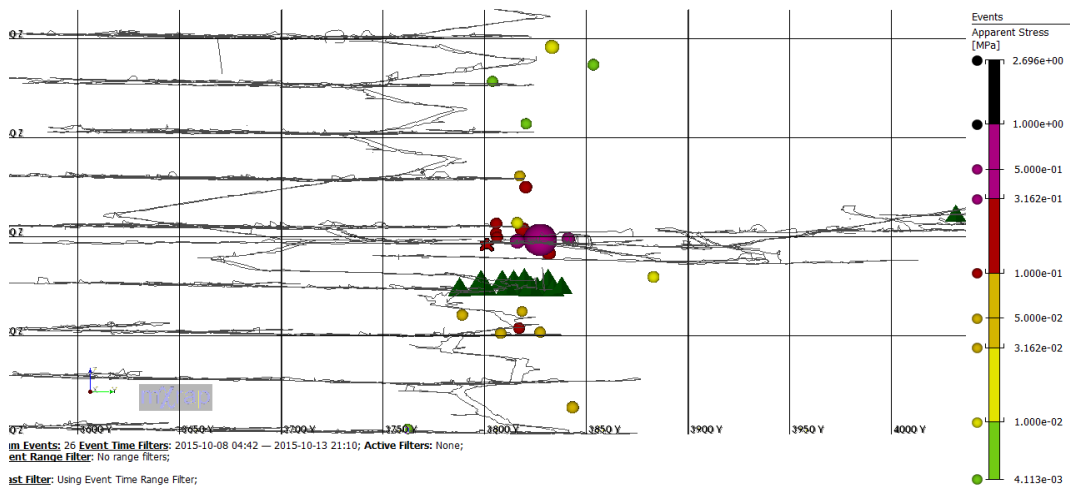
The apparent stress of seismic events is shown in Figure 6.17 - from top to bottom defined from the merged, permanent and local network databases, respectively. The lowest apparent stresses were found from the permanent network. The lower apparent stress seismic events located mostly upper side of the cluster of the permanent and the merged datasets. On the other hand relation between the apparent stress and location was almost random of the local network.



(a)



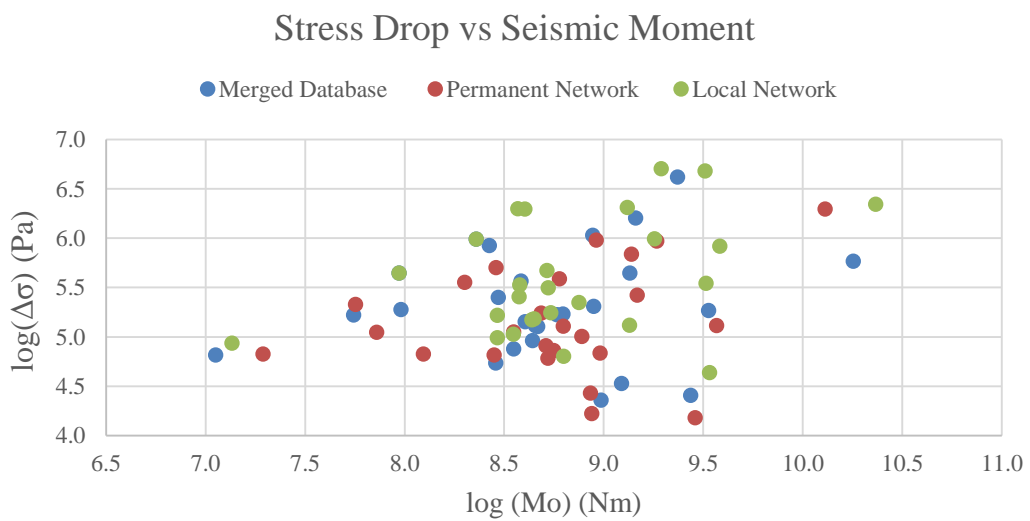
(b)



(c)

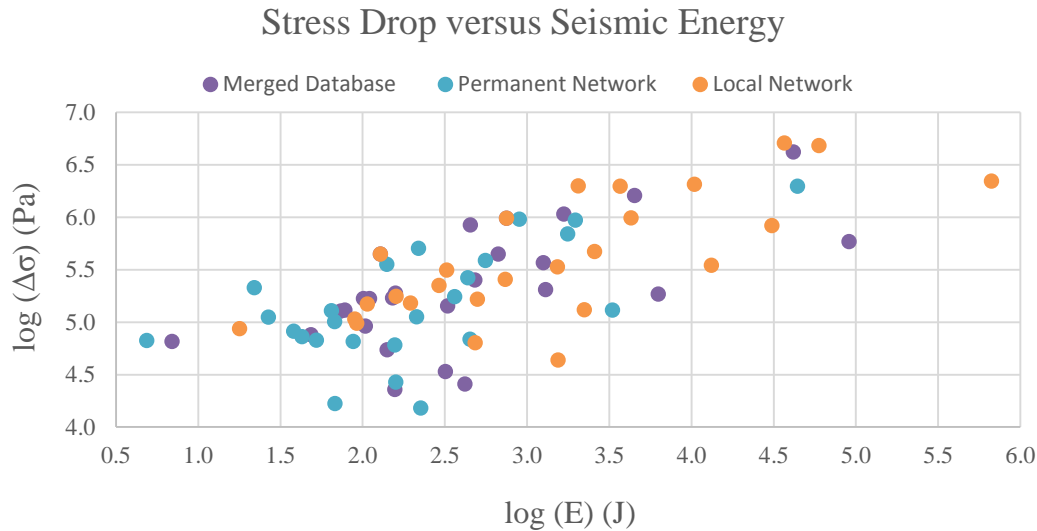
**Figure 6.17 :** Apparent stress of seismic events of (a) merged database, (b) permanent network and (c) local network. The green triangles show the local network sensors and the size of the circles represent moment magnitude.

The logarithm of the stress drop and logarithm of seismic moment graphs is shown in Figure 6.18. The stress seismic moment range was from  $10^7$  to  $10^{10}$  Pascal when stress drop range was between  $10^4$  and  $10^6$  Pa for the permanent network. When the merged and local system were examined with same way, the stress drop and magnitude ranges were found wilder than the permanent system. There are three straight lines where seismic moments were 8.5, 9.0 and 9.5 and stress drop changed widely. Moreover, some of the events seismic moment was between 8.5 and 9.0 Nm and their stress drop range were from 4.75 to 5.25 Pa. The highest stress drop value of local network was occurred on October 10 at 20:14 with moment magnitude 0.1.



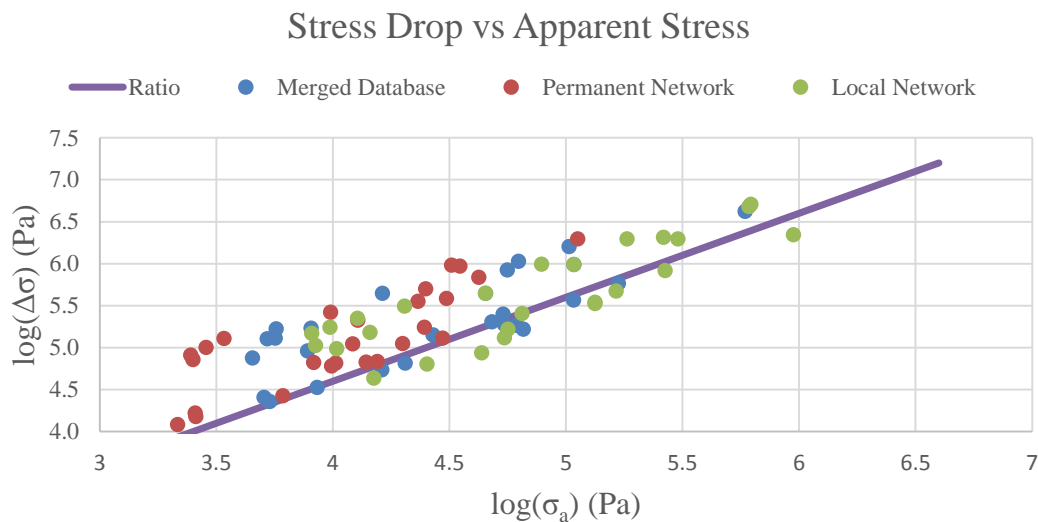
**Figure 6.18 :** Stress drop versus logarithm of seismic moment. The green, red and blue dots represent the local network, the permanent network and merged dataset, respectively.

The logarithm of stress drop as a function of the logarithm of energy is given in Figure 6.19. Stress drop changes in a limited range (from 4 to 6.5 Pa). The stress drop increased with seismic energy generally but the stress drop of several seismic events were very different even if they had similar seismic moment. The highest stress drop was found in the local network. The average stress drop was 5.6, 4.7 and 5.9 Pa for the merged database, permanent and local network, respectively.



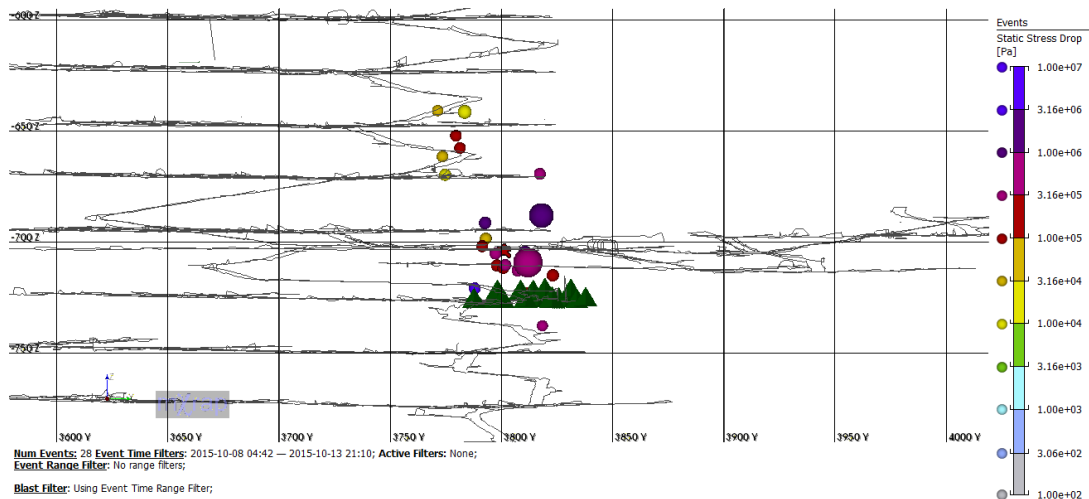
**Figure 6.19 :** Stress drop and logarithm of the seismic energy. The orange, blue and purple dots represent the local network, the permanent network and merged dataset, respectively.

Figure 6.20 shows the logarithm of stress drop and the logarithm of apparent stress of Garpenberg Mine seismic events with all databases. Most of the permanent system seismic events had lower stress drop and apparent stress. The higher values of given parameters were obtained by local network solutions. This theoretical line is generally fits crustal events but as seen in Figure 6.20, the theoretical line did not fit to induced seismic events at Garpenberg Mine. The ratio of stress drop and the apparent stress is 3.1, 3.5 and 3.1 for the merged, permanent and local systems, respectively.

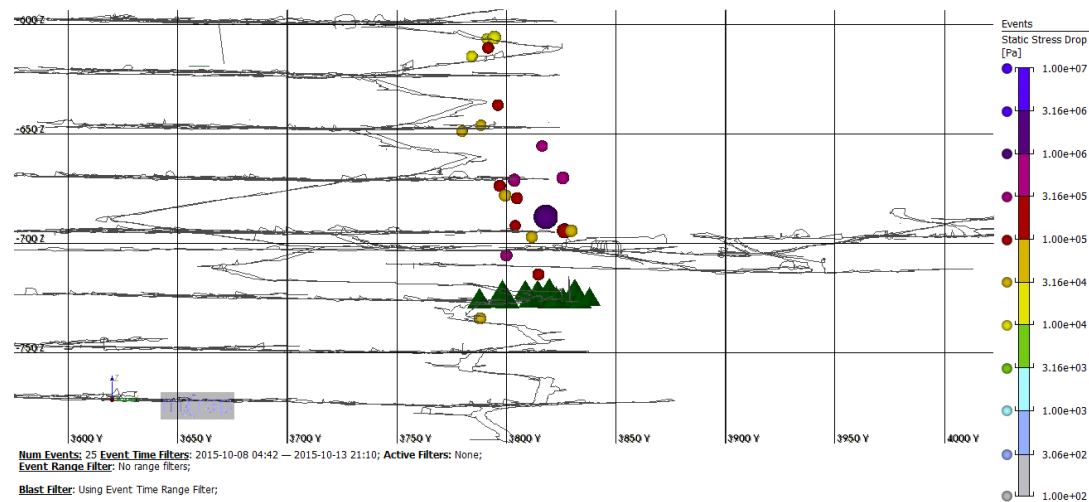


**Figure 6.20 :** The logarithm of stress drop and the logarithm of apparent stress. The green, red and blue dots represent the local network, the permanent network and merged dataset, respectively.

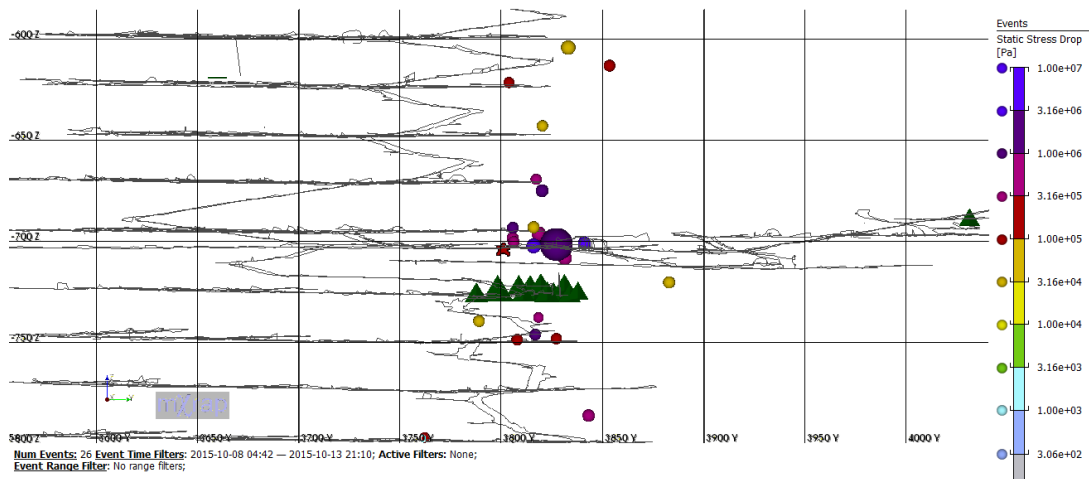
Stress drop of merged, permanent and local seismic events are shown in Figure 6.21 from top to bottom, respectively. The highest stress drop was estimated for the largest moment magnitude events. The stress drop spatial distribution was not similar with apparent stress.



(a)



(b)



(c)

**Figure 6.21** : Stress drop of seismic events of (a) merged database, (b) permanent network and (c) local network. The green triangle shows the local network sensors and the size of the circle represents moment magnitude.

### 6.3.6 Source radii

Source radius is also a function of the corner frequency and velocity of the medium. The medium of Garpenberg mine site was assumed as homogenous in order to avoid complexity of data processing. That is why the differences in source radii calculated by different datasets are only dependent on the corner frequency.

Figure 6.22 shows how source radius changes with respect to the moment magnitude. The maximum source radii were found in the permanent network solutions because this event's corner frequency is the lowest over all events. Source radius increases with moment magnitude as can be expected. The largest radius is around 40 m for Mw 0.3 event.

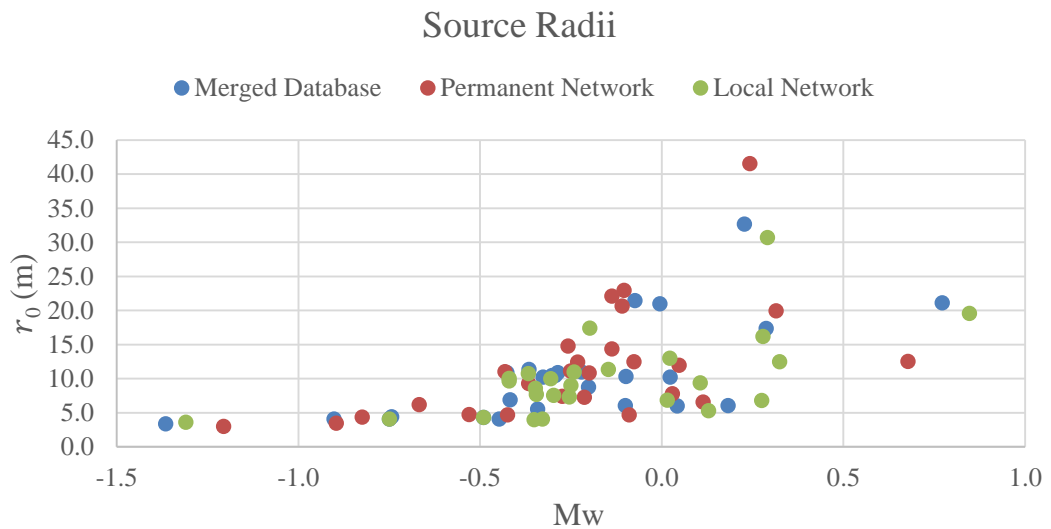


**Figure 6.22 :** Source radius versus moment magnitude. The green, red and blue dots represent the local network, the permanent network and merged dataset, respectively.

### 6.3.7 Summary and conclusions about the activity in Garpenberg

In this study the seismic event data processing at Garpenberg Mine was quite different from the routine data processing to obtain the source parameters. The aim was to find more precise solution for the kinematic and dynamic source parameters from existing networks and created merged database and analyze how the parameters are affected by the data (seismic system) used for the calculation. A new merged dataset that includes data from both existing seismic system was created and all parameters of the seismic events were calculated for three different cases – local, permanent, and merged datasets.

It was found that the hypocenter locations are obtained well if the event occurred in the middle of the sensor sites (the case of good sensors coverage). In this case the total location differences between different datasets could be reduced to a few meters. Although data processing steps are handled well and the AHD is less than 5%, location differences increase up to 200 meters between each database when the event is outside of the good sensor coverage.

Dynamic source parameters are also affected by sensor coverage. The parameters in the local database are generally higher than in the permanent and merged ones. Figure 6.23 shows a summary how dynamic source parameters changed depending on the sensor coverage.

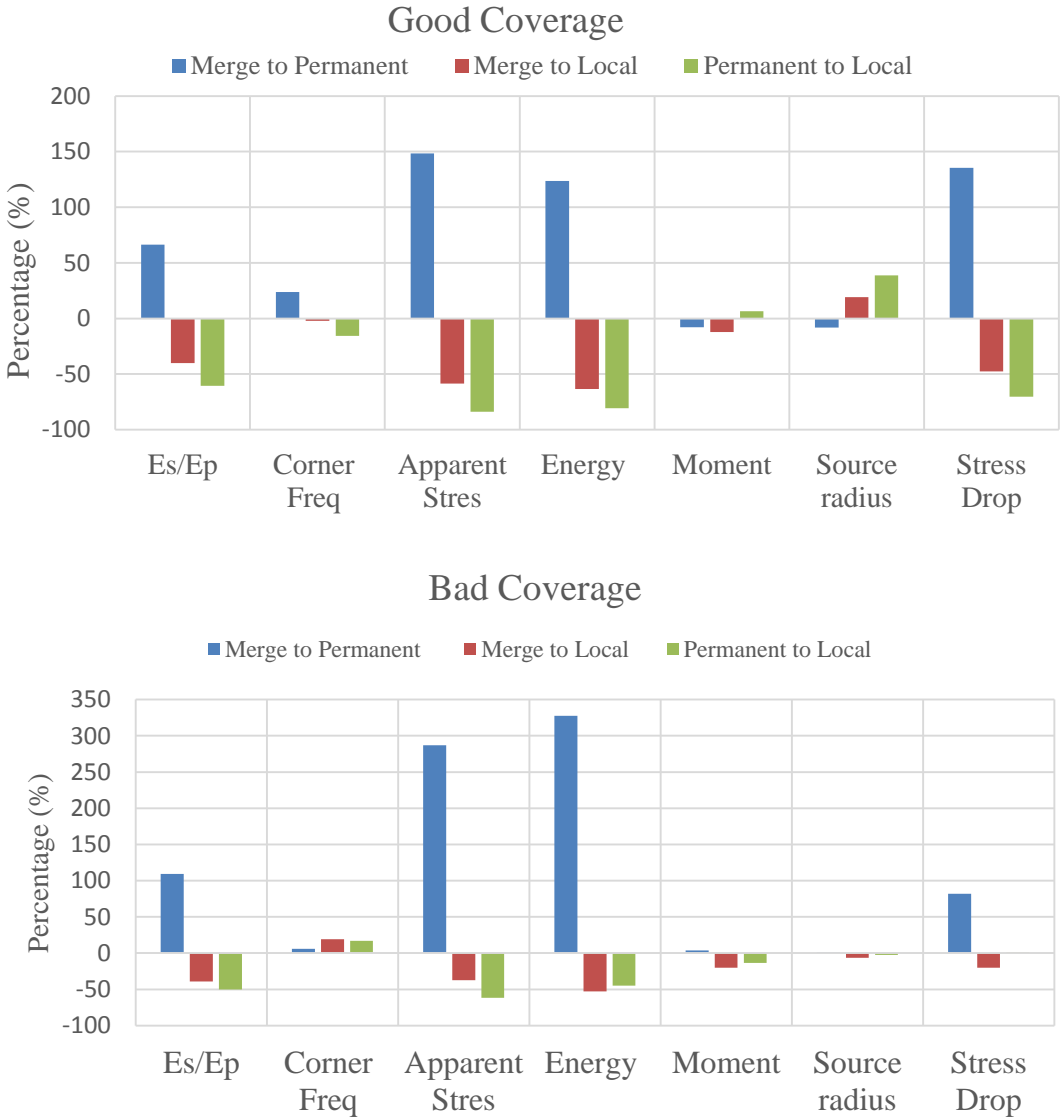


**Figure 6.23** : Dynamic seismic parameters change due to the coverage.



The source parameters which are a function of the corner frequency changes the most when the coverage was bad. The corner frequencies of P- and S- wave are shown in Figure 6.24 and Figure 6.25, respectively. Corner frequencies of P- and S- wave could not be separated in term of sensor coverage. Corner frequencies of local network were higher than corner frequency of permanent network seismic events. However, it is obvious that when the location of seismic event was with good sensor coverage, the change in source parameters was smaller. Seismic moment is the only parameter which is always less affected by sensor coverage.

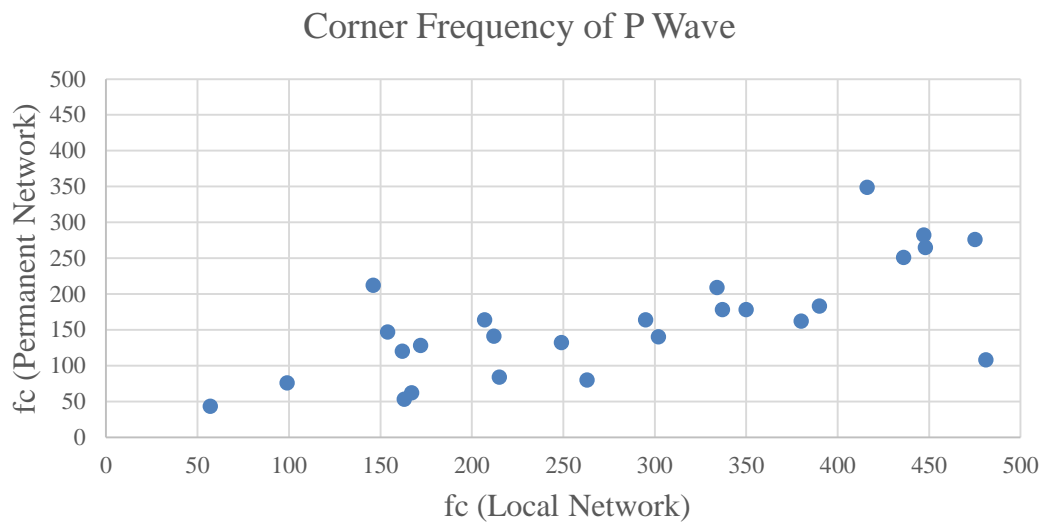


**Figure 6.24 :** Corner frequency of P wave.

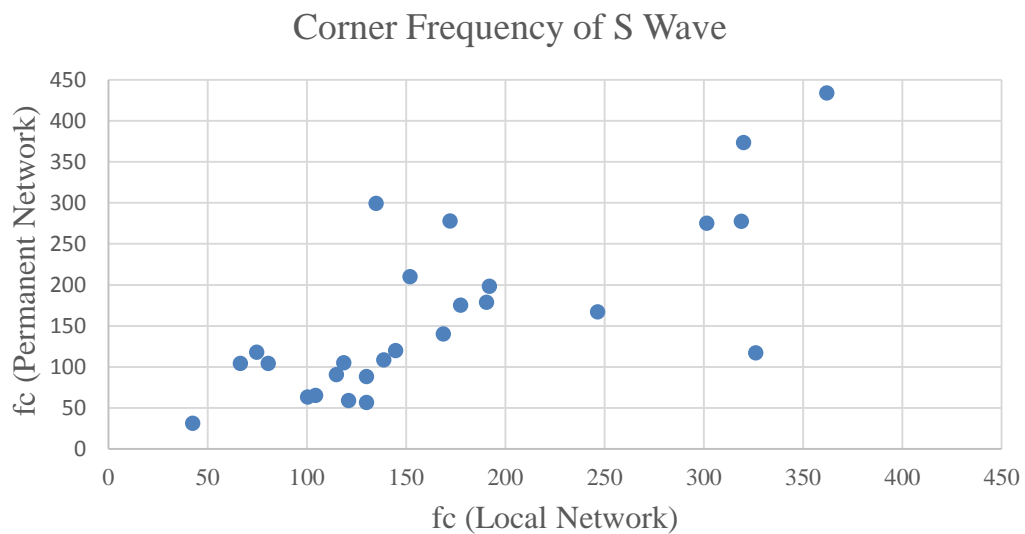


**Figure 6.25 :** Corner frequency of S wave.

The energy of the seismic events is highly affected by the location, due to the sensor coverage of the seismic event. One of the possible reasons is that the energy is affected by the radiation pattern of the seismic source. As shown in Figure 6.26, P and S wave has different radiation pattern and the location of sensor become critically important. If sensors is located on the  $x_3$  dimension mostly, the highest S wave energy will be recorded however, P wave will not be recorded. On the other hand, the P wave energy is the highest on between  $x_1$ - $x_3$  direction. If most of the sensors are placed along that direction, S wave will not be recorded, so the energy calculation become wrong. In order to get precise solution, sensors should be design to cover all radiation patterns.

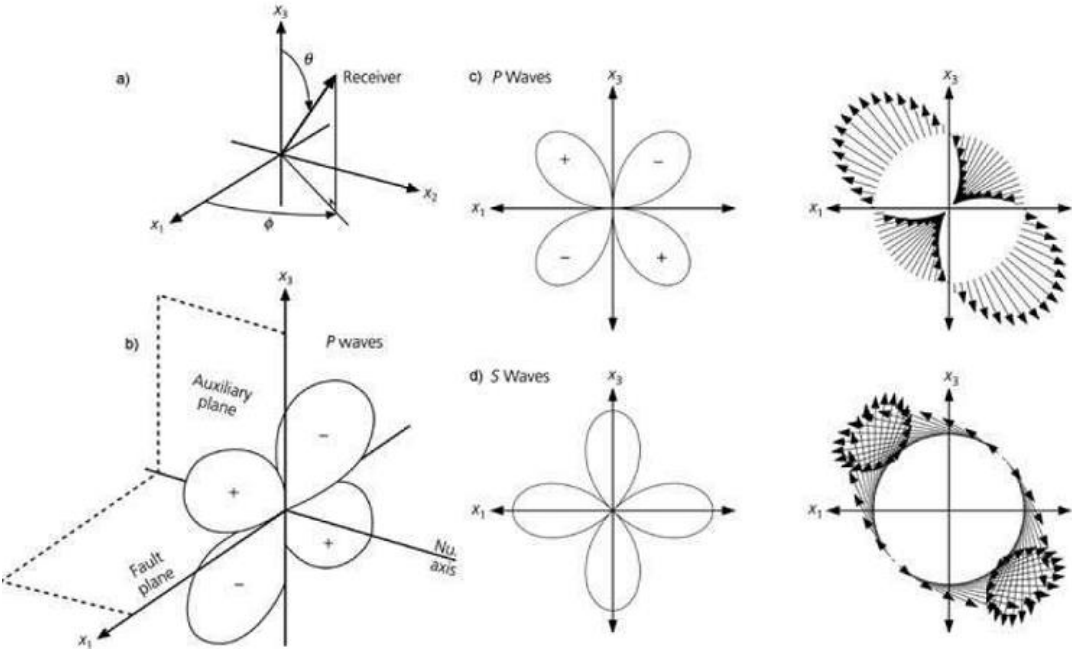


**Figure 6.26 :** Fault plane and body waves radiation patterns.

As Brune (1970) mentioned, estimation of energy of seismic wave depends upon the azimuthal coverage. The seismic energy of each of the body waves are shown in Figure 6.27 and 6.28, as good and bad coverage, respectively. The energy of P- and S- wave increased linearly under the good sensor coverage case (Figure 6.27). However, energy of S wave was always higher than energy of P wave. The energy correlation of seismic body waves were mostly visible for seismic events of the permanent network.

The energy of seismic body waves were almost random when event was classified as a bad coverage (Figure 6.28). The energy of bad coverage of seismic events were always lower than good coverage seismic events.

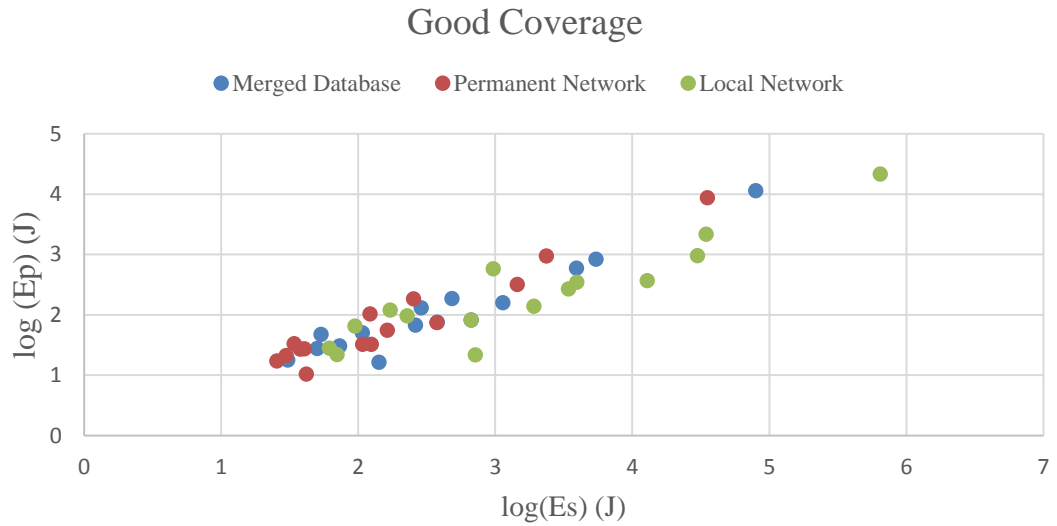


**Figure 6.27 :** Good coverage seismic events body waves energy.

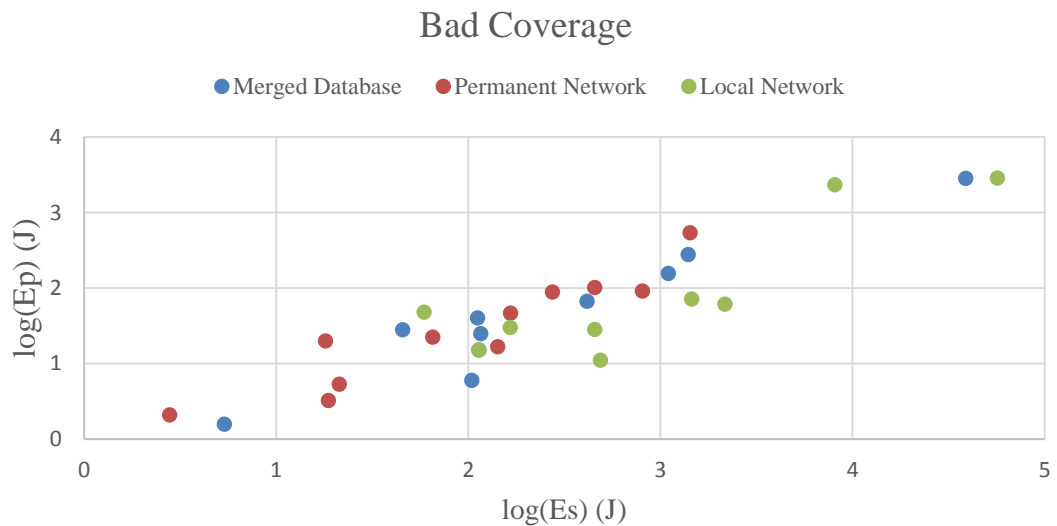


**Figure 6.28 :** Bad coverage seismic events body waves energy.

The second fact that the energy of the seismic events in the local system is almost always larger than from the permanent and merged system could be related to wrong (underestimated correction for attentions). Most of the processed events are close to the local seismic sensors and in this case the waves travel without losing much energy during the propagation. Possibly the attenuation for the sensors in the permanent system has to be verified. In order to estimate the effect of attenuation further studies are needed.

The problem with the determination of the kinematic and dynamic parameters in Garpenberg Mine was identified here. If the source location is close to the local seismic system, the dynamic source parameters calculated using only data from this system would be more accurate but location could be problematic if the sensors from the permanent seismic system are not used. The, merged database should be used to obtain more accurate results, as the sensors of both systems together provide the best possible coverage.

## **7. SEISMIC SOURCE PARAMETER AFTER BLASTING OF TWO MINES**

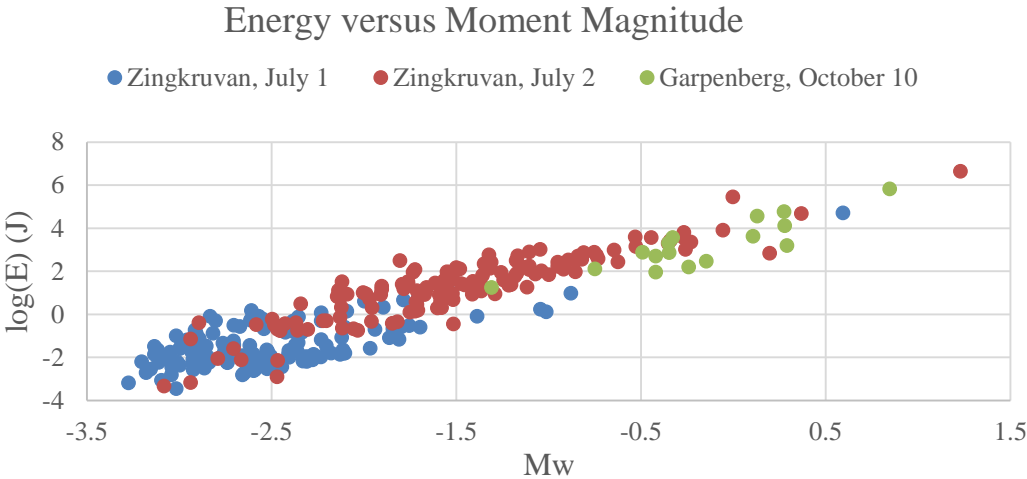
Zinkgruvan and Garpenberg mine sites are monitored by local networks. The local networks 18 and 16 sensors at Zinkgruvan and Garpenberg Mine, respectively. Moreover, Garpenberg Mine is also monitored by permanent network. It was noticed that these local seismic system record much lower magnitude events in close proximity than the permanent seismic systems from local seismic systems was used to study the seismicity after blasting nearby.

Seismic events on July 1 and July 2, 2015 in Zinkgruvan and seismic events around October 10, 2015 in Garpenberg mine were studied and source parameters were compared. The all seismic events were recorded by local network. Although, very few number of events recorded at Garpenberg local network comparatively Zinkgruvan Mine, the source parameters of seismic events were similar. The cluster dimension, moment magnitude, radiated energy, apparent stress and stress drop parameters were used to reveal the similarities of each local networks.

Zinkgruvan mine site is more sensitive to blast operations. After the production blast, more than 200 seismic events were recorded at first half an hour and more than 3000 events recorded consecutive days and maximum 10% of total event might be noise. Seismic activity dropped back to the pre-production blast level, around 1.5 hours later to the production blast. On the other hand, Garpenberg Mine seismic activity level and data quality were different. Within October 8 to October 13, more than 1700 seismic events were recorded by local network and 282 seismic events were noise. The production blast also caused sudden and dramatic increase on number of seismic events at Garpenberg Mine. Before the blast, averagely 5 events recorded within half hours, but more than 100 events recorded at the first half hours just after the blast.

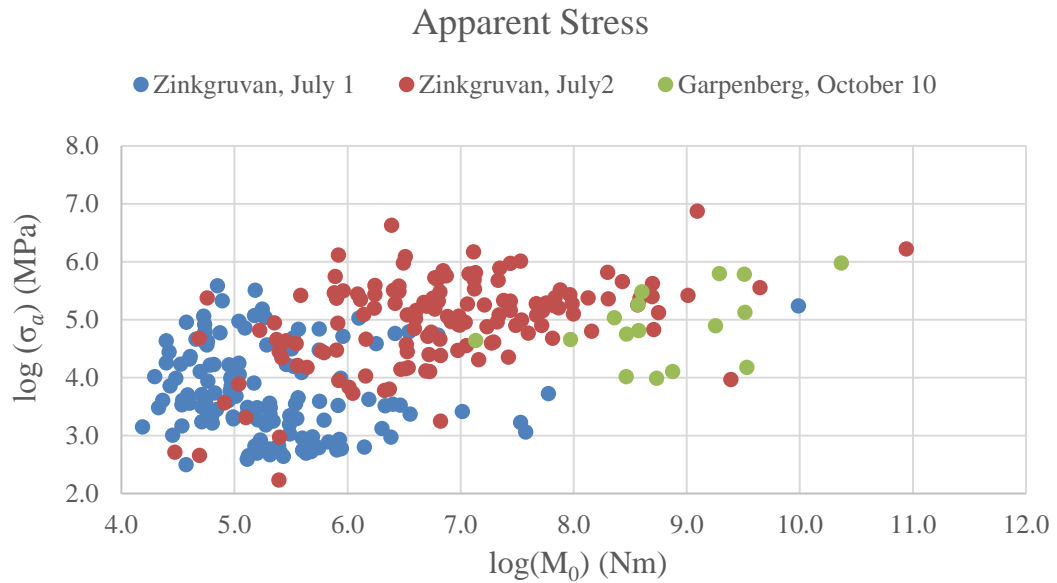
The cluster dimensions were 50m×60m×80m and 50m×80m×80m for Zinkgruvan and Garpenberg local networks, respectively. Moment magnitude range of each dataset were between -3.1 and 1.2, and between 1.3 and 0.9 for July 2 and October 10, respectively.

Figure 7.1 show logarithm of energy versus moment magnitude of Zinkgruvan July 1, Zinkgruvan July 2 and Garpenberg October 10 seismic events. The radiated energy of seismic events on October 10 were parallel to July 2 seismic events solutions. Radiated energy increases with moment magnitude on October 10 seismic events. Most probably, if lower magnitude seismic events dynamic solutions, the pattern of the seismic events fit well with July 2 seismic events.



**Figure 7.1 :** Logarithm of the energy versus moment magnitude of July 1 (blue), July 2 (red) and October 10 (green) seismic events.

Logarithm of the apparent stress and logarithm of seismic moment solution is given in Figure 7.2. The seismic events can be grouped as the seismic event dates and mines. July 1 seismic events apparent stress were the lowest. The average apparent stress of each groups were  $10^4$ ,  $10^5$  and  $10^5$  Nm for July 1, July 2 and October 10, respectively. The seismic moment of October 10 seismic events were higher but apparent stress relatively lower. The apparent stress level of July 2 and October 10 were same but seismic moment average of October 10 was 10 times more than July 2. In overall the apparent stress increases with seismic moment, based on all data.



**Figure 7.2 :** Logarithm of the apparent stress versus logarithm of the moment on July 1, July 2 and October 10 seismic events.

Figure 7.3 shows logarithm of stress drop versus logarithm of the radiated energy on July 1, July 2 and October 10 of seismic events. The average stress drop and radiated energy of seismic event on October 10 were lower than seismic events on July 2.

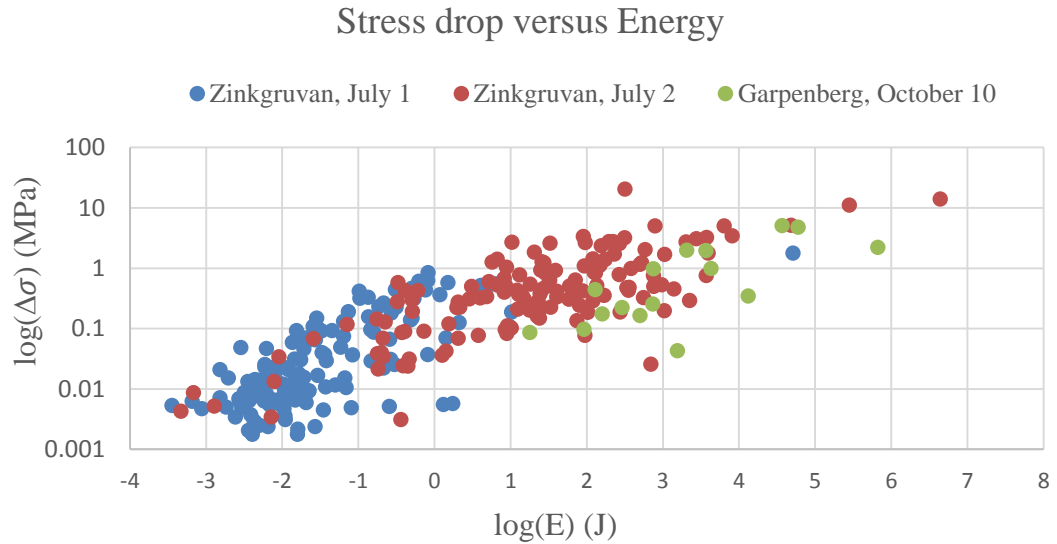


**Figure 7.3 :** Logarithm of the stress drop versus logarithm of the radiated energy on July 1, July 2 and October of 10 seismic events.

All given dynamic source parameters are necessary to explain rock responses after the blast sequence of each mine. Three and seven seismic events moment magnitude were bigger than 0 at Zinkgruvan mine on July 2 at Garpenberg mine on October 10, respectively.

The moment magnitude of processed seismic events of Garpenberg mine were higher and the radiated energy also increases with it. The trend lines of July 2 and October 10 were almost parallel. Even though the average apparent stress were same, the seismic moment of October 10 were extremely higher. The stress changing after the seismic events were bigger on October 10.



## **8. CONCLUSIONS**

The aim of this thesis was to obtain the kinematic and dynamic parameters of mining-induced seismic events caused by blasting in order to make some conclusions about the rock mass response to blasting in different conditions and mines. The work was carried out for data from two Swedish underground mines – Zinkgruvan and Garpenberg, with recently installed temporary local seismic systems in addition to the existing permanent seismic systems. Data had to be processed manually in order to obtain the parameters with the best possible accuracy. For Garpenberg mine merging data from the local and permanent systems was possible and sensitivity of the source parameters to sensor number and geometry configuration was tested to provide recommendations for future routine processing in the mine.

### **8.1 Zinkgruvan Mine**

Zinkgruvan is a seismically activate mine and a rockburst occurred on July 2, 2015 after production blasting that caused damage. More than 3000 seismic events were recorded by the local seismic system between July 1 and July 2. These events occurred mostly after a blast on July 1 and the blast on July 2 that caused the rockburst. Both blasts were located close to the local seismic system. The automatic processing of the data that is done by the IMS Trace software is not reliable for obtaining source parameters with good quality and accuracy. That is why a maximum possible number of events had to be processed manually. Using some criteria 271 seismic events were selected for manual processing and to carry on the study.

The results of the thesis showed that the locations of the events formed separate clusters on each date with dimensions  $\sim 50 \times 30 \times 60$  m and  $50 \times 60 \times 80$ , respectively. The moment magnitude of the events varied between -3.3 and 1.2. The highest magnitude events occurred on the edges of the clusters – on the top of the cluster on July 1 (Mw 0.6, 15 minutes after production blast operations) and at the bottom of the other cluster on July 2 (Mw 1.2, during production blasting).

The seismic activity on both days raised sharply immediately after the blasting and then gradually decreased to the pre-blasting level within 1.5 hours. On July 2 two more larger magnitude events occurred (Mw 0.2 and 0.4) within approximately two hours and after them the seismic activity started increasing again. As the seismic system was disconnected from the server due to the rockburst, data was available only for about three hours after the blasting and the complete sequence of events was not recorded.

The analysis of dynamic source parameters for each date showed consistent differences for the clusters on July 1 and 2. In general the events on July 1 had smaller magnitudes, seismic moment, seismic energy, apparent stress and stress drop compared with the events on July 2. The apparent stress did not show strong correlation with the seismic moment for neither date.

The available data is not enough for estimation of the actual mechanism (seismic moment tensor). Instead a proxy for the type of the mechanism based on the energy ratio  $E_s/E_p$  was used and it was found that the seismic events were predominantly of shear type but 67% of the events on July 1 were shear while 60% of the events on July 2 were shear. The rest of the events were classified as non-shear. The largest event on July 1 was defined as shear and the largest event on July 2 was defined as non-shear.

The information about the orientation and size of the cluster on July 2, as well as the type of the mechanism (non-shear), can be used to identify the size, orientation, and type of the seismic source. Additional geological and geotechnical information should be obtained to verify the possible parameters of the source of the event that caused the rockburst (damage).

The difference in the results about the seismic activity related to blasting on two consecutive days in Zinkgruvan mine in two areas not far from each other shows that there are factors, like local geology and rock mechanical properties, that most probably affect the response of the rock mass to blasting. More detailed studies similar to the one carried out in this thesis are necessary to define a relationship between the blasting activity and these factors. Ultimately the results of this kind of studies can help to define the potential for large seismic events due to blasting, and possibility for a rockbursts. They can help also for defining criteria for re-entry protocols (when it would be safe to enter the mine after blasting, e.g. how long will take for seismic activity to decrease after blasting).

## 8.2 Garpenberg Mine

Induced seismic events at Garpenberg Mine were automatically processed but the kinematic and dynamic solutions were different for each seismic networks. In order to be determined the precise solution for parameters of induced seismic event, a new method was defined. The local and permanent networks seismic events, which moment magnitude were bigger than -1.5, were merged and the new database is called merged database.

The biggest production blast was done on October 10, 2015 at 16:00, this activity increased the seismic activity and eight seismic events was found which moment magnitudes were bigger than -0.2. Any seismic hazard was not reported but the hypocentral location of these events were questionable even the residual error was lower than 5%. The seismic activity did not go down to the initial pre-blasting level even six hours after the blast.

Source location were classified as a sensor coverage. The total differences at source locations were close to each other if hypocenter is covered well. Under the bad sensor coverage, the total distance difference of hypocenter locations of network comparisons were found more than 200 m. The merged and permanent database seismic events source location are always close to each other because the permanent network sensors are dominant.

Bad coverage seismic events in merge database generally had extremely higher values than permanent network, such as apparent stress, stress drop, energy and  $E_s/E_p$  ratio. However, apparent stress and stress drop are linked to the corner frequency which the result quite similar, energy of same of event could be found as ten times higher at merge database. On the other hand local network seismic event parameters has been found always higher than Merge Database, even the calculated hypocenter of event was not close. The most surprisingly, the similarity of source parameters were optimum between permanent and local networks.

As result, the local network source location is less trustable because the back-azimuthal angle was lower if events hypocenter was far from it. However, dynamic source parameters are generally higher and they are not effected much from sensor coverage. The merged database seismic event source location determination is better

because local network sensor coverage lack might be covered by permanent network, or reverse. The dynamic source parameters of merge database are between the local network and permanent network. Further studies are still needed in order to reveal the change of dynamic parameters. However, the permanent network seismic event might be effected by attenuation which changes the waveform, because P- and S- wave origin changed.

The permanent network is generally designed because of the procedures of mine. On the other hand, the local network is installed to the limited area due to catch of a possible higher magnitude seismic events and/or rockburst. The limited area for local network is found by helping other mine methods.

The kinematic errors will be less than hundred meter for good sensor coverage case. Even if location was not precise but stay in the cluster, gives an idea about the area which is seismically active. The most important issue to do that, the local network should not be placed mostly on one plane.

This study will be improved if this method to be applied any mine areas which permanent network consists more sensors. Reducing number of sensor during data processing, changes on the kinematic solution should be defined. In this case, specific sensor could be removed, for investigation sensor coverage effects on the dynamic parameters. In order to be classified seismic event solution as sensor coverage, total number of processed event must be kept as much as possible. Focusing on seismic event which after the production blast will improve the number of seismic events for data processing.

This method might be a core study for finding optimum solution for a seismic system which has limited number of sensors. However, more studies are still needed and data processing might be improved.

## REFERENCES

- Aki, K., & Richards, P. G.** (2002). *Quantitative Seismology*, Second Edition, University Science Books Sausalito, California
- Alcott, J. M., Kaiser P. K., & Simser, B. P.** (1998). Use of Microseismic Source Parameters for Rockburst Hazard Assessment, *Pure Applied geophysics*, 153, 41-65
- Allen, R., Ripa, M. & Jansson N.** (2008). Palaeoproterozoic volcanic- and limestone-hosted Zn-Pn-Ag-(Cu-Au) massive sulphide deposits and Fe oxide deposits in Bergslagen, Sweden (IGCP Project 502), 33 IGC, XXXIII Geologorum Conventus
- Bengtsson, V. C.** (2000). Lithochemical Characteristic of a Profile Across the Nygruvan Orebody, Zinkgruvan, South-Central Sweden (Report No: B234). Göteborg: Earth Science Centre Göteborg University
- Björnaborg, K.** (2009). *The copper sulphide mineralization of the Zinkgruvan deposit, Bergslagen, Sweden* (Master Thesis), Lund University, Department of Geology, Lund
- Boliden Garpenberg.** (2016). Retrieved April 4, 2016, from [http://www.boliden.com/Documents/Press/Publications/Broschures/Broschyr\\_Garpenberg\\_EN.pdf](http://www.boliden.com/Documents/Press/Publications/Broschures/Broschyr_Garpenberg_EN.pdf)
- Bollinger, G. A.** (1989). Microearthquake activity associated with underground coal-mining in Buchanan County, Virginia, U.S.A, *Pure and Applied Geophysics*, 129(3), 407-413
- Brady, B. H. G & Brown, E. T.** (2004). *Rock Mechanics for Underground Mining*, 3<sup>rd</sup> Edition, Springer
- Brune, J. N.** (1970), Tectonic Stress and the Spectra of Seismic Shear Waves from Earthquakes, *Journal of Geophysical Research*, 75(26), 4997-5009
- Brune, J. N.** (1971). Seismic sources, fault plane studies and tectonics, *Earth & Space Science News*, 52(5), IUGG 178- IUGG 187

- Brune, J.N., Archuleta, R.J. & Hartzell, S.** (1979). Far-field S-wave spectra, corner frequencies, and pulse shapes. *Journal of Geophysical Research*, 84, 2262–2272
- Båth, M.** (1979). Introduction to Seismology, Second Revised Edition, *Springer*.
- Cao, A., Dou L., Yan, R., Jiang H., Lu, C., Du T., & Lu, Z.** (2009). Classification of Microseismic Events in High Stress Zone, *Mining and Technology*, 19, 0718-0723
- Chorney, R., Jain, P., Grob, M., & Van Der Baan, M.** (2012). Geomechanical Modeling of Rock Fracturing and Associated Microseismicity, *The Leading Edge*, 31(11), 1348-1354
- Ge, M.** (2005). Efficient Mine Microseismic Monitoring, *International Journal of Coal Geology*, 64, 44-56
- Ge, M.** (2012). Source Location Error Analysis and Optimization Methods, *Journal of Rock Mechanics and Geotechnical Engineering*, 4(1), 1-10
- Ge, M., & Kaiser, P. K.** (1991). Practical Application of an Innovative Microseismic Source Location Procedure, *Geotechnical and Geological Engineering*, 10, 163-184
- Gibowicz, S. J.** (1975). Variation of Source Properties: The Inangahua, New Zealand, Aftershock of 1968, *Bulletin of Seismological Society of America*, 65(1), 261-276
- Gibowicz, S. J.** (1998). Partial Stress Drop and Frictional Overshoot Mechanism of Seismic Events Induced by Mining, *Pure and Applied Geophysics*, 153, 5-20
- Gibowicz, S. J.** (1990). Seismicity Induced by Mining, *Advances in Geophysics*, 32, 1-74
- Gibowicz, S. J., & Kijko, A.** (1994). *An Introduction to Mining Seismology*, 1<sup>st</sup> Edition, Academic Press
- Gibowicz, S. J. & Lasocki, S.** (2001). “Seismicity Induced By Mining” Ten Years Later, *Advances in Geophysics*, 44, 39-181
- Gurha, S. K.** (2000). Induced Earthquakes. Dordrecht, The Netherlands: Kluwer Academic Publishers
- Gupta, H. K. & Chadha, R. K.** (1995). Induced Seismicity, *Pure and Applied Geophysics (PAGEOPH)*, 145 (1), 1-216

- Hanks, T. C., and Kanamori H.** (1979). A moment magnitude scale, *Journal of Geophysical Research*, 84(5), 2348 - 2350
- Hartzell, S. H. & Archuleta, R. J.** (1979). Rupture propagation and focusing of energy in a foam rubber model of a stick slip, *Journal of Geophysics Research*, 84(B7), 3623-3636
- Hasegawa, H. S., Wetmiller, R. J. & Gendzwell, D. J.** (1989). *Induced Seismicity in Mines In Canada – An Overview*, *Pure & Applied Geophysics*, 129 (3-4), 423-453
- Havskov, J., & Ottemöller, L.** (2010). *Routine Data Processing in Earthquake Seismology*, Springer
- IMS Trace**, <http://www.imseismology.org/download-trace/> , Institute of Mine Seismology, Australia
- Kanamori, H., and Anderson, D. L.,** (1975). Theoretical basis of some empirical relations in seismology, *Bulletin Seismological Society of America*, 65, 1073-1095.
- Kijko, A., & Sciocatti, M.** (1995). Optimal Spatial Distribution of Seismic Stations in Mines, *Int. J. Rock Mech. Sci. & Geomech. Abstr.*, 32(6), 607-615
- Kulhanek, O.** (1997). *Anatomy of Seismograms*, Elsevier Science Publisher B. V. Second Edition
- Liu, J., Feng, X., Li, Y., Xu, S., & Sheng, Y.** (2013). Studies on Temporal and Spatial of Microseismic Activities in a Deep Metal Mine, *International Journal of Rock Mechanics & Mining Sciences*, 60, 171–179
- Madariaga, R.** (1976). Dynamics of an expanding circular fault, *Bulletin of Seismological Society of America*, 66(3), 639-666
- McGarr, A., Simpson, D., & Seeber, L.** (2002). 40 Case Histories of Induced and Triggered Seismicity, *International Geophysics, International Handbook of Earthquake and Engineering Seismology*, 81(A), 647-661
- Mendecki, A.J.** (1994). Quantitative seismology and rock mass stability. In: *Guide to Seismic Monitoring in Mines*, First edition. (A. J. Mendecki, Ed.). ISS International, Welkom, South Africa.
- Mendecki, A. J., ed.,** (1997). *Seismic Monitoring in Mines*, Chapman and Hall, London

- Mendecki, A. J. & Niewiadomski, J.** (1997). Spectral analysis and seismic source parameters, In Mendecki, A. J., *Seismic Monitoring in Mines*, First Edition, Chapman & Hall
- Molnar, P., and Wyss M.** (1972). Moments, Source Dimensions and Stress Drops of Shallow-Focus Earthquakes in The Tonia-Kermadec Arc, *Phys. Earth Planet. Interiors.*, 6, 263-278
- Murphy, M. M., Westman, E. C., Iannacchione, A. & Barzak, T. M.** (2011), Relationship Between Radiated Seismic Energy and Explosive Pressure for Controlled Methane and Coal Dust Explosion in an Underground Mine, *Tunnelling and Underground Space Technology*, Vol. 28, pp 278-286
- Nelder, J. A. & Mead, R.** (1965). A Simplex Method for Function Minimization, *The Computer Journal*, 7 (4), 308-313
- Nicholson, C., & Wesson, R.** (1992). Triggered Earthquakes and Deep Well Activities, *Pageoph*, 139(3/4), 561-578
- Occheina, C. Pirulli, M., & Scavia C.** (2014). A Microseismic-Based Procedure for the Detection of Rock Slope Instabilities, *International Journal of Rock Mechanics & Mining Sciences*, 69, 67-79
- Owen, M. L., and Meyer, L. H. I.** (2013). NI 43-101 Technical Report for the Zinkgruvan Mine, Central Sweden (Report No: MM775). United Kingdom: Wardell Armstrong International.
- Pakalnis, R. T., and Hughes, P. B.** (2011). Sublevel Stopping, SME Mining Engineering Handbook Volume Two, (Editor: Peter Darling), Third Edition, Society for Mining, Metallurgy, and Exploration, US, p.1355-1363.
- Raina, A.K., Chakraborty, A.K., Ramulu M. & Jethwa, J.L.** (2000). Rock mass damage from underground blasting, a literature review, and lab- and full scale tests to estimate crack depth by ultrasonic method, *FRAGBLAST – International Journal of Blasting and Fragmentation*, 4, 103–125
- Shearer, P., M.** (2009), *Introduction to Seismology*, Second Edition, Cambridge University Press.
- Šílený, J., and Milev, A.** (2008), Source Mechanism of Mining Induced Seismic Events – Resolutions of Double Couple and Non Double Couple Models, *Tectonophysics*, 456, 3-15
- Stein, S. & Wyssession, M.** (2003). *An Introduction Seismology, Earthquakes, and Earth Structure*, First Edition, Blackwell Publishing Ltd



- Talebi, S.** (1998). Introduction, Talebi, S. (Ed.) *Seismicity Caused by Mines, Fluid Injections, Reservoirs, and Oil Extraction*, (Vol. 1 pp. 1-2) Springer Base AG
- USGS,** (2015). [http://www2.usgs.gov/blogs/features/usgs\\_top\\_story/induced-earthquakes-raise-chances-of-damaging-shaking-in-2016/](http://www2.usgs.gov/blogs/features/usgs_top_story/induced-earthquakes-raise-chances-of-damaging-shaking-in-2016/)
- Vallejos, J. A. & McKinnon, S. D.** (2011), Correlations Between Mining and Seismicity for Re-entry Protocol Development, *International Journal of Rock Mechanics & Mining Sciences*, Vol 48, pp 616-625
- Vivallo, W.** (1985). The Geology and Genesis of The Proterozoic Massive Sulfide Deposit at Garpenberg, Central Sweden, *Economic Geology*, 80, 17-35
- Wang, H., and Ge M.** (2008). Acoustic Emission/Microseismic Source Location Analysis for a Limestone Mine Exhibiting High Horizontal Stresses, *Journal of Rock Mechanics & Mining Sciences*, 45, 720-728
- Wyss, M.** (1970). Stress Estimates of South American Shallow and Deep Earthquakes, *J. Geophys. Res.*, 75, 1529-1544
- Young, R. P., S. Talebi, D. A. Hutchins & T. I. Urbancic.** (1989). Source Mechanism Studies of Mining Induced Microseismic Events at Strathcona Mine, Sudbury, Canada, *PAGEOPH, Special Issue on Mining Induced Seismicity*, 129(3-4), 455-474.



## CURRICULUM VITAE



**Name Surname** : İrem ERGUNCU GÜÇLÜ

**Place and Date of Birth** : ANKARA 24/01/1988

**E-Mail** : iremerguncu@hotmail.com

**EDUCATION** :

- **B.Sc.** : 2011, ITU, Mining Faculty, Geophysics Engineering

### **PUBLICATIONS, PRESENTATIONS AND PATENTS ON THE THESIS:**

- **Erguncu Güçlü, İ., Dineva S., Hansen-Haug, J.** (2016). *Microseismic activity after blasting at Zinkgruvan Mine (Sweden)*. European Geosciences Union General Assembly 2016, Vienna, Austria, 17–22 April
- **Erguncu Güçlü, İ., Dineva, S., Grigoli, F., Fjellström, P., and Karaman A.** (2016). *Sensitivity of kinematic and dynamic parameters of induced seismic events to sensor coverage (Garpenberg Mine, Sweden)*, 35rd General Assembly of the European Seismological Commission (GA ESC), Trieste, Italy, 4-10 September